Continuous 24-hour Shack-Hartmann optical turbulence profiling on a small telescope.

RYAN MICHAEL GRIFFITHS

GRIFFITHS, RYAN MICHAEL (2024) Continuous 24-hour Shack-Hartmann optical turbulence profiling on a small telescope. Doctoral thesis, Durham University.

Continuous 24-hour Shack-Hartmann optical turbulence profiling on a small telescope

Ryan Griffiths

A thesis presented for the degree of
Doctor of Philosophy

Centre for Advanced Instrumentation
The University of Durham
United Kingdom
5th December 2024

For nan

1949 - 2021

Continuous 24-hour Shack-Hartmann optical turbulence profiling on a small telescope

Ryan Griffiths

Abstract

Atmospheric optical turbulence monitoring has been used for site selection and operation scheduling at observatories for decades, and is a critical element in the operational package for upcoming 20-40 m class telescopes. Furthermore it is a key validation method for adaptive optics systems. Continuous, 24-hour optical turbulence monitoring is a novel capability with a number of high-impact applications in astronomy, solar astronomy, optical turbulence forecasting and free space optical communications. The subject of this thesis is the Shack Hartmann image motion monitor (SHIMM), the first continuous 24-hour optical turbulence monitor. The instrument uses short-wave infrared observations of bright stars with a Shack-Hartmann wavefront sensor and small telescope to measure optical turbulence parameters and a low-resolution $C_n^2(h)\,\mathrm{d}h$ profile. Combined slope and intensity measurements from the Shack-Hartmann sensor are used to characterise the turbulence profile, and methods are validated through Monte Carlo simulations. The opto-mechanical design consists primarily of commercially-available components and is portable on a 28 cm telescope. The transmission spectrum is estimated and validated, finding a central wavelength of approximately 1280 nm. Using the simulation results, the maximum target star magnitude is found to be 0.07 in the J band and target availability to be sufficient for continuous measurements. Finally, on-sky results are presented for two sites: Paranal observatory and Barcelona. At the former, the SHIMM is found to agree well with existing turbulence monitoring instruments at the site. The latter is a permanent urban monitoring station, and early site monitoring are discussed indicating strong turbulence and that adaptive optics would be advantageous for a potential ground station.

Supervisors: James Osborn and Richard Wilson

Acknowledgements

I would like to begin by thanking my incredible supervisors James and Richard for their support and patience throughout the last four years, and for their thorough proofreading and feedback on this thesis. I am incredibly thankful to both of you for the opportunities and memories that I have made throughout my time at Durham. I feel extremely lucky to have worked with such amazing people on this project and for my thesis surviving two natural disasters in the pandemic and the volcanic eruption on La Palma.

Thank you also to the many people in CFAI that made the department such a welcoming and supportive place. To everyone who has always been happy to help when I was stuck on a problem, for all the fun conversations at the pub and to everyone who has contributed on campaigns, helping me through many sleep deprived days and nights.

I am extremely grateful to my parents for all their encouragement and help throughout the years and to my wider family for always cheering me on. Finally, my biggest thanks go to Rebecca. Thank you for keeping me sane and for your incredible unwavering support throughout my PhD.

Contents

Declaration

The work in this thesis is based on research carried out at the Centre for Advanced Instrumentation, Department of Physics, University of Durham, England. No part of this thesis has been submitted elsewhere for any other degree or qualification, and it is the sole work of the author unless referenced to the contrary in the text.

Some of the work presented in this thesis has been published in journals and conference proceedings - the relevant publications are listed below.

Publications

R. Griffiths, J. Osborn, O. Farley, T. Butterley, M. J. Townson, and R. Wilson. Demonstrating 24-hour continuous vertical monitoring of atmospheric optical turbulence. *Optics Express*, 31(4):6730, 2 2023b. ISSN 1094-4087. doi: 10.1364/OE.479544. URL `https://opg.optica.org/abstract.cfm?URI=oe-31-4-6730`

R. Griffiths, L. Bardou, T. Butterley, J. Osborn, R. Wilson, E. Bustos, A. Tokovinin, M. Le Louarn, and A. Otarola. A comparison of next-generation turbulence profiling instruments at Paranal. *Monthly Notices of the Royal Astronomical Society*, 529(1):320–330, 2 2024. ISSN 0035-8711. doi: 10.1093/mnras/stae434

R. Griffiths, J. Osborn, O. Farley, T. Butterley, M. Townson, and R. Wilson. The 24hSHIMM: a continuous day and night turbulence monitor for optical communications. In H. Hemmati and B. S. Robinson, editors, *Free-Space Laser Communications XXXV*, page 54. SPIE, 3 2023a. ISBN 9781510659315. doi: 10.1117/12.2648789

List of Figures

List of Tables

Nomenclature

AO adaptive optics

SHIMM Shack Hartmann image motion monitor

MASS Multi Aperture Scintillation Sensor

DIMM differential image motion monitor

FASS full aperture scintillation sensor

SCIDAR Scintillation Detection and Ranging

S-SCIDAR Stereo-Scintillation Detection and Ranging

SCO-SLIDAR single coupled SLODAR-SCIDAR

CO-SLIDAR coupled SLODAR-SCIDAR

NNLS non-negative least squares

BVLS bounded variable least squares

SLODAR slope detection and ranging

RINGSS ring image next-generation scintillation sensor

WFS wavefront sensor

OTA optical tube assembly

VLT Very Large Telescope

ELT Extremely Large Telescope

SHWFS Shack-Hartmann wavefront sensor

MLA microlens array

PSF point spread function

FWHM full width at half maximum

InGaAs indium gallium arsenide

SWIR short wave infrared

MLA microlens array

FADE FAst DEfocus

SNR signal-to-noise ratio

DAO Durham Adaptive Optics

OT optical turbulence

ESO European Southern Observatory

TURBO TURBulence mOnitoring and forecasting

MCAO multi-conjugate adaptive optics

HV Hufnagel-Valley

FOV field of view

OGS optical ground station

RTC real time control

FSOC	free space optical communications
FSO	free space optics

Chapter 1

Introduction

1.1 Motivation

For millennia those watching the skies have marvelled at the effects of atmospheric optical turbulence. The earliest written reference to the phenomenon is made by Aristotle in 350 BC in “On the Heavens” in which he posits that the apparent twinkling of the stars is related to some trembling effect of the image brought about by their distance from the earth. With optics and fluid dynamics yet to be invented, the true cause of this charming optical effect was unfortunately out of his reach. Indeed the phenomenon of atmospheric optical turbulence would not come to be truly understood until the mid-20$^{\mathrm{th}}$ century, despite the fact that astronomers have long been aware of its influence. The description of optical turbulence is based on early works by Kolmogorov (1941) describing energy cascades in turbulent flow, with important contributions from other authors such as Taylor (1938) and Obukhov (1971). The resulting phase perturbation of optical waves was subsequently thoroughly described by authors such as Tatarski et al. (1961), Fried (1965), Noll (1976), Roddier (1981). As astronomical technologies advanced and telescope sizes increased, it became clear that atmospheric optical turbulence represented a fundamental limit on the achievable accuracy of solar and astronomical observations. The phase distortion acquired by light passing through the atmosphere, when averaged over long exposures, results in a point spread function (PSF) that is significantly larger than a large telescope's diffraction limit. This phenomenon is referred to as “seeing”. An obvious early application of the statistical theory of optical turbulence was in site monitoring to provide a quantitative method for determining locations with good seeing. Some early techniques are discussed in the review by Coulman (1985) and include the use of balloon-based micro-thermal probes to profile turbulence strength above observatory sites (Barletti et al., 1974), scintillation measurements from double stars (Azouit and Vernin, 1980) and interferometry (Dainty et al., 1975). Before the emergence of adaptive optics (AO), in which the optical phase distortions are measured and corrected for by a phase-controlling element and wavefront sensor, site selection was one of the chief ways to mitigate the limiting effects of atmospheric optical turbulence.

Due to the increasing costs and sensitivity requirements of astronomical instruments, site monitoring has become an ever more critical tool for the design and operation of observatories (Milli et al., 2019). The emergence of the differential image motion monitor (DIMM), a simple two-aperture turbulence monitor based on differential wavefront tip/tilt measurements, in the late 1980s, was a critical development in the field (Sarazin and Roddier, 1990). The instrument found early use in the site monitoring campaign for the Very Large Telescope (VLT) (Sarazin, 1986) and has since been used successfully at many other observatories (Wood et al., 1995; Ziad et al., 2005; Sagar et al., 2000). The advantages of having a dedicated, portable, real-time optical site monitoring instrument have led to the dominance of the DIMM at major astronomical observatories around the world. This has given rise to a number of other instruments and techniques aiming to supplement or improve upon its success. Since the development of AO, additional aspects of optical turbulence such as angular and temporal coherence have become critical parameters for the design and modelling phase of such systems (Osborn et al., 2018), and so instruments capable of measuring the vertical profile of optical turbulence strength, such as the Multi Aperture Scintillation Sensor (MASS) (Kornilov et al., 2003), have become increasingly important. In addition, the next generation of Extremely Large Telescopes (ELTs) with 20-40m diameter primary mirrors will be far more sensitive to the outer scale of optical turbulence (Guesalaga et al., 2017), making its measurement a high priority.

Furthermore, such site monitoring activities are no longer limited to astronomical and solar observatories. Atmospheric optical turbulence is also a major limitation in free space optics (FSO) such as satellite-to-ground laser communications (Chan, 2006; Mata Calvo et al., 2019), including long-range quantum key distribution (Erven et al., 2008; Polnik et al., 2020) and space debris deorbiting via acceleration due to laser ablation or photon pressure (Bennet et al., 2012). For free space optical communications (FSOC) using a laser link between a satellite and an optical ground station (OGS), phase distortion of the laser light after propagation through optical turbulence results in jitter and speckling of the PSF in a receiver telescope (Chan, 2006). This severely limits the efficiency by which the light can be coupled into an optical fibre in the focal plane and therefore the achievable bit error rate of communications (Schieler et al., 2023). In the case of optical communications between an OGS and a satellite in low-Earth orbit, or between an OGS at high latitudes and a geostationary satellite, the link will need to be maintained down to low elevation angles where these effects are greatly magnified by airmass. Site monitoring will therefore play a critical role in determining the optimal locations for OGSs and in supporting their operation (Birch et al., 2023a). In stark contrast to the pristine mountain-top sites typical for astronomy, OGSs will need to be placed near to major population centres and in sub-optimal locations to deliver high bandwidth data rates to consumers. Communications applications also require OGSs networks to maintain optical links continuously for 24-hours a day. Such sites are also likely to experience strong turbulence conditions being at low-altitudes and in urban environments with numerous heat sources in the local environment. Moreover, AO offers a path to achieving higher data rates of communication links with many ongoing experiments demonstrating new technologies, for example see Mata Calvo et al. (2019); Biasi et al. (2023). As with astronomy, these systems demand a more detailed characterisation than offered by the DIMM alone.

The aim of this work is to present a successful implementation of a site monitoring instrument capable of meeting the current needs of both astronomy and FSOC. The instrument presented in this thesis is the Shack Hartmann image motion monitor (SHIMM). It exploits a Shack-Hartmann wavefront sensor (SHWFS) operating in the short wave infrared (SWIR) and utilises techniques for wavefront-sensing in high noise to provide continuous 24-hour vertical turbulence monitoring even in strong turbulence conditions. The system is built around a commercial 11" telescope and the low weight and size make it ideal for portable campaigns anywhere in the world. The instrument monitors a single, bright star and can extract the Fried parameter, r_0, isoplanatic angle, θ_0, coherence time, τ_0, the Rytov variance, σ_R^2, and a four-layer vertical $C_n^2(h)\,\mathrm{d}h$ profile. The SHIMM instrument began as a night-time only, single star turbulence monitor developed a few years ago at Durham university (Perera, 2017; Perera et al., 2023). The work presented here describes significant upgrades to the instrument concept in both the hardware and data analysis as the first continuous, day and night turbulence profiler. Due to its ability to provide detailed and continuous measurements of optical turbulence conditions in real time, the instrument has several exciting applications in supporting novel research into FSOC and astronomy. The first has already been discussed at length: in site characterisation and operations scheduling for observatories and OGS networks. Moreover, the continuous data sets generated by the instrument are ideal for 24-hour validation of optical turbulence forecasts (Quatresooz et al., 2023). There is also potential to be further integrated with forecasts using auto-regression techniques (Masciadri et al., 2023) to increase the predictive accuracy of such tools. This capability will be of paramount importance, for example in managing observation schedules for the costly and upcoming generation of ultra-high performance ELT instruments (Masciadri et al., 2020).

1.2 Synopsis

This thesis will firstly lay out the well-known and understood physical concepts relevant to the SHIMM instrument analysis in chapter 2, along with a discussion of the operating principles of similar site monitoring instruments to place it in the wider context of the field.

Chapter 3 will build on the theoretical framework developed for the coupled SLODAR-SCIDAR (CO-SLIDAR) to present a method by which optical turbulence profiles and the coherence time of the optical turbulence may be estimated from SHWFS slope and intensity measurements on a small telescope. This includes most critically new weighting functions for the slope measurements which are necessary for wavefront sensing with noisy images, as will be the case for the SHIMM instrument. Moreover there is lengthy discussion regarding corrections to the method for non-zero exposure times, noise bias, outer scale, dome turbulence, and spectral bandwidth.

Following this theoretical groundwork, in chapter 4 the image analysis methods are described and validation of the SHIMM instrument techniques are carried out using Monte Carlo wave optical simulations. The chapter begins by documenting the background subtraction algorithm. The accuracy of brightest pixel and correlation centroiding algorithms are then explored along with the techniques by which the spot intensities can be measured. The methods of centroid noise estimation, profile reconstruction and coherence time measurement are validated for typical daytime experimental conditions. The chapter ends by exploring the accuracy of reconstructed profiles given different numbers of layers, with and without regularisation.

Following the validation of the analysis, chapter 5 describes the instrument optics, design and hardware. Estimation of the transmission spectrum and the target availability imposed by the instrument design are also presented. Finally, the operating principles and software design are detailed systematically to give the reader a clear understanding of how real-time measurements are achieved.

Chapter 6 presents the results of two major measurement campaigns involving the SHIMM. The first being a milestone campaign at Paranal involving the SHIMM and other novel turbulence monitoring instruments. This section provides a detailed look at the results from that campaign and how the novel turbulence monitoring instruments compared to the well-characterised, permanently-installed turbulence monitors at Paranal. The second part is a key application of the SHIMM for site monitoring in an urban environment to provide information for OGS design. A particular focus is made on contrasting daytime and night-time measurements from the two SHIMM instruments in the experiment and showing the results of dome turbulence fitting to the data.

Finally, chapter 7 concludes this analysis into the SHIMM instrument and discusses some of the exciting future work and applications of the instrument.

Chapter 2

Theory

A flow moving with a uniform velocity becomes turbulent and induces mixing through eddy production when the critical Reynolds number of the system is exceeded. The Reynolds number is a dimensionless quantity equal to the ratio between inertial forces and viscous forces. This is expressed as $R = Vl/\nu$ where V is the characteristic velocity of the flow, l is the characteristic scale length of the system and ν is the kinematic viscosity. In the atmosphere, and in the boundary layer in particular, this critical threshold is exceeded and turbulent flow of air occurs.

2.1 Atmospheric optical turbulence

Atmospheric optical turbulence is caused by random variations in refractive index of the air resulting from the turbulent mixing of air with different temperatures and hence densities. The three dimensional refractive index field of the atmosphere can be described by $n(\mathbf{r})$. An assumption is made that light wavefronts entering the atmosphere from stars, which are effectively point sources at infinity, are plane waves with a uniform amplitude. Alternative sources such as satellites may be treated as point sources if they are of a sufficiently small angular size and less than the diffraction limited resolution of the telescope. The atmospheric optical turbulence is assumed to be concentrated in a number of thin layers parallel to the ground and as the plane wave passes through these layers it acquires phase deviations across the wavefront, $\phi(\mathbf{x})$, corresponding to different parts of the wavefront experiencing different refractive indices. The resulting complex amplitude is described by

$$\psi(\mathbf{x}) = A \exp[i\phi(\mathbf{x})]. \tag{2.1}$$

As the absolute value of the amplitude is not critical to the analysis, a normalised amplitude of $A = 1$ is typically assumed. In order to investigate the effect on the complex amplitude analytically, a further assumption is made that phase perturbations are small and as such

$$\psi(\mathbf{x}) \approx 1 + i\phi(\mathbf{x}). \tag{2.2}$$

This is called the Rytov approximation (Andrews and Phillips, 2005). The wavefronts then propagate to the ground. The analytic expression after the propagation is given by the Fresnel approximation, as the wavefront deviations are larger than the wavelength of light (Roddier, 1981),

$$\psi_0(\mathbf{x}) = \psi(\mathbf{x}) * \frac{1}{i\lambda z} \exp\left[i\pi \frac{\mathbf{x}^2}{\lambda z}\right], \tag{2.3}$$

where λ is the wavelength of light and z is the propagation distance in metres. Substitution of equation 2.2 into equation 2.3 yields,

$$\psi_0(\mathbf{x}) = 1 + \varepsilon(\mathbf{x}), \tag{2.4}$$

where $\varepsilon(\mathbf{x})$ describes the fluctuations in complex amplitude as a result of the atmospheric optical turbulence with the real part giving the log amplitude fluctuation χ and the imaginary part the phase fluctuation ϕ,

$$\chi(\mathbf{x}) = \phi(\mathbf{x}) * \frac{1}{\lambda z} \cos\left(\frac{\pi|\mathbf{x}|^2}{\lambda z}\right), \tag{2.5}$$

$$\varphi(\mathbf{x}) = \phi(\mathbf{x}) * \frac{1}{\lambda z} \sin\left(\frac{\pi|\mathbf{x}|^2}{\lambda z}\right). \tag{2.6}$$

It can be further shown that under the assumption of small phase perturbations, the resulting complex amplitude fluctuations of light propagating through many atmospheric layers is equal to the sum of the individual contributions, i.e. $\varepsilon(\mathbf{x}) = \sum \varepsilon_i(\mathbf{x})$ (Roddier, 1981).

Since atmospheric optical turbulence is a chaotic process, we are limited to studying the statistical properties of the turbulence when evaluating its effect on the wavefront phase distortions. A key metric for evaluating the spatial statistics of optical turbulence is the structure function. It describes the variance of difference in a random field at two points $\mathbf{x}$ and $\mathbf{x} + \boldsymbol{\rho}$ as a function of their separation. The structure function of refractive index variations is given by

$$D_N(\rho) = \langle |n(\mathbf{x}) - n(\mathbf{x} + \boldsymbol{\rho})|^2 \rangle. \tag{2.7}$$

Equation 2.7 relies on two major assumptions to express the structure function in this way. The first is that the random refractive index fluctuations are isotropic, such that the structure function is dependent on the magnitude of the separation, $\rho = |\boldsymbol{\rho}|$, rather than its direction. The second assumption is that the fluctuations are locally homogeneous such that the structure function is not dependent on the absolute position $\mathbf{x}$. The structure function of refractive index fluctuations can be further expressed using Kolmogorov-Obkuhov theory of turbulence by

$$D_N(\rho) = C_N^2 \rho^{2/3}, \tag{2.8}$$

where the quantity C_N^2 is called the refractive index structure constant, which itself is a key measure of the strength of the optical turbulence. Using the knowledge that the wavefront phase distortion is the integral of refractive index along its path of travel multiplied by the wavenumber, it is possible to directly relate this quantity C_N^2 to the amount of phase distortion and to calculate a structure function for the phase fluctuations.

2.2 Turbulence Power Spectra

Kolmogorov theory states that in turbulent flow, kinetic energy is injected into the system forming eddies of a characteristic size defined by the system geometry. These eddies transfer energy into smaller and smaller eddies until a minimum spatial scale is reached at which the kinetic energy dissipates into heat through friction. The largest scale size of turbulent eddies is referred to as the outer scale of the turbulence L_0 while the smallest scale is the inner scale l_0. The power spectrum of optical turbulence describes the energy distribution of the turbulence as a function of spatial frequency f and is a key quantity of interest. The power spectrum is valid only in the inertial range $L_0^{-1} \ll f \ll l_0^{-1}$. One can also calculate a structure function of the phase, which is linked to the power spectrum of the phase, $\Phi(f)$, through the following relation (Jenkins, 1998),

$$D_\phi(\mathbf{r}) = \langle |\phi(\mathbf{x}+\mathbf{r}) - \phi(\mathbf{x})|^2 \rangle, \tag{2.9}$$

$$D_\phi(\mathbf{r}) = 2\int_0^\infty \Phi(\mathbf{f})\left[1 - \cos(2\pi f r)\right] \mathrm{d}\mathbf{f}. \tag{2.10}$$

2.2.1 Kolmogorov Turbulence

The Kolmogorov turbulence power spectrum assumes that the inner scale is zero and the outer scale is infinite. The Kolmogorov power spectrum for a single, thin turbulent layer of width dh is given by the equation (Roddier, 1981),

$$\Phi_{\mathrm{K}}(\mathbf{f}) = 9.7 \times 10^{-3} k^2 f^{-11/3} C_n^2(h)\mathrm{d}h, \tag{2.11}$$

where $f = |\mathbf{f}|$ is the spatial frequency and k the wavenumber. The corresponding structure function is obtained through substitution of 2.11 into equation 2.10 yielding

$$D_\phi(\mathbf{r}) = 6.88(r/r_0)^{5/3}, \tag{2.12}$$

where r_0 is the Fried parameter defined in section 2.6.

2.2.2 Von Kármán Turbulence

The Von Kármán power spectrum arises from inclusion of the turbulence outer scale L_0 in the model (Tatarski, 1971),

$$\Phi_{\mathrm{VK}}(\mathbf{f}) = 9.7 \times 10^{-3} k^2 (L_0^{-2} + f^2)^{-11/6} C_n^2(h)\mathrm{d}h. \tag{2.13}$$

This avoids the infinity in the power spectrum at $f = 0$, and reduces to equation 2.11 for $L_0 \to \infty$. Each layer in the atmosphere will have a different outer scale such that a vertical profile of $L_0(h)$ exists and has been measured using both optical techniques (Maire et al., 2007) and radiosonde (Abahamid et al., 2004). The integrated effect of the outer scale profile at the ground is of greater relevance for AO. It is known as the wavefront coherence outer scale (Borgnino, 1990),

$$\mathcal{L}_0 = \left[\frac{\int_0^\infty L_0^{-1/3}(h) C_n^2(h)\mathrm{d}h}{\int_0^\infty C_n^2(h)\mathrm{d}h} \right]^{-3}, \tag{2.14}$$

and its physical interpretation is the distance at which the structure function of the phase begins to saturate. Measurements of the wavefront coherence outer scale have traditionally been in poor agreement, finding values between 1 m and 100 m (Ziad, 2016). This range suggests the unfortunate case that almost all optical turbulence monitoring instruments will be making measurements on baselines far smaller than the outer scale, while science instruments on large telescopes will be highly sensitive to fluctuations in the outer scale, especially on upcoming 20 - 40 m

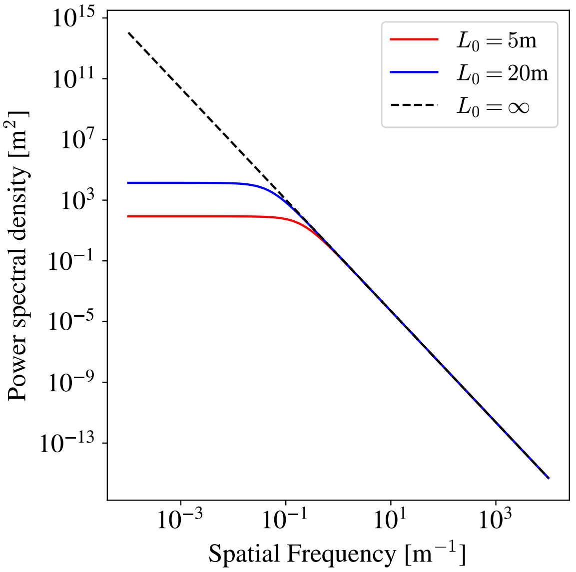

Figure 2.1: Von Kármán and Kolmogorov power spectra as a function of spatial frequency.

telescopes such as the ELT. A comparison of the power spectral density for Von Kármán and Kolmogorov turbulence is shown in figure 2.1.

2.3 Scintillation

Scintillation describes the twinkling effect of the stars. This directly results from equation 2.5 which describes the propagation of distorted wavefronts producing intensity fluctuations at the ground. The atmospheric turbulence acts as a series of weak lenses causing focus and defocus across the wavefront, resulting in a speckled pattern of intensity at the ground (Osborn et al., 2015). The size of the speckles is characterised by the Fresnel radius $r_F \propto \sqrt{\lambda z}$. It is clear from this equation and equation 2.5, that low altitude turbulence will be hard to sense as speckle sizes will be small and that at the ground $z = 0$, there will be no scintillation produced. Figure 2.2 shows the effect of optical propagation of a distorted plane wave for two different propagation distances, illustrating the increase in speckle size with propagation. Taylor's frozen flow theorem (Taylor, 1938) states that small

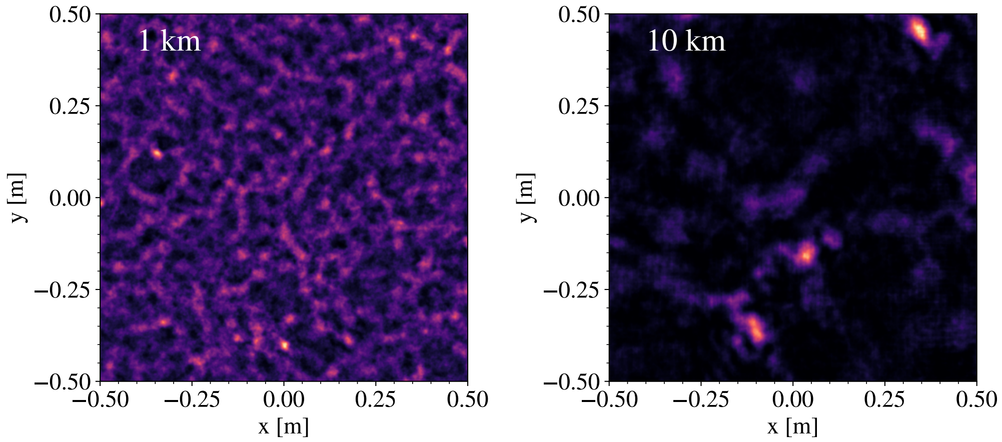

Figure 2.2: Simulated intensity of a plane wave after passing through a turbulent layer of r_0 = 10cm and propagating a distance of 1 km (left) and 10 km (right).

scale turbulent eddies will propagate along the wind direction without significant evolution, suggesting a direct link between the spatial and temporal structure of turbulent phase across an aperture. Under this assumption a speckled pattern in the wavefront intensity resulting from the optical turbulence will blow across the aperture, and the total amount of light within the aperture will fluctuate - leading to a temporal variance in the apparent magnitude of the stars or received light from a satellite laser downlink beam.

The relationship between log amplitude and intensity is $I = e^{2\chi}$. It is convenient to quantify the "strength" of scintillation through the scintillation index σ_I^2 where

$$\sigma_I^2 = 4\sigma_\chi^2 = \frac{\langle I^2\rangle - \langle I\rangle^2}{\langle I\rangle^2}. \tag{2.15}$$

This equation describes the normalised intensity variance as a result of optical turbulence, however it does not discriminate between different aperture sizes. In all experimental measurements of light, a collecting aperture of a finite size is required within which the light will be averaged. Even an image of a telescope

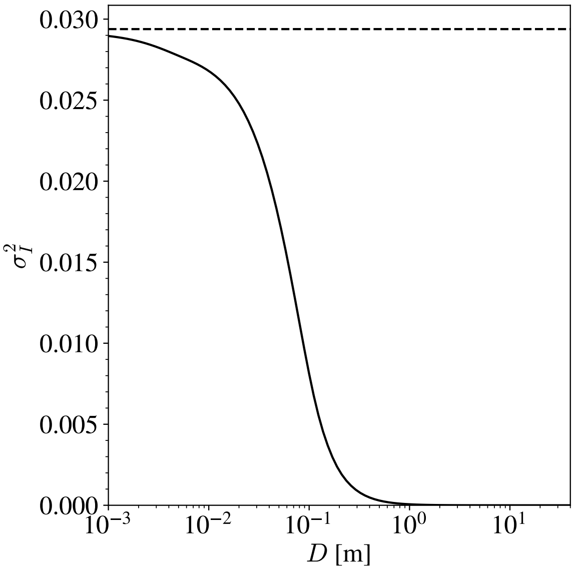

Figure 2.3: A figure showing how the theoretical scintillation index decreases with increasing aperture diameter D for a circular aperture and a simple 3-layer model of atmospheric turbulence. The asymptotic black dashed line is equivalent to σ_R^2, i.e. the scintillation index for an infinitely small aperture.

pupil is discretised by detector pixels within which averaging occurs. As a result, an aperture will act as a low-pass filter as it averages out high-spatial frequency information (i.e. small speckle sizes). A theoretical expression for the scintillation index measured by an arbitrary aperture is given by Tokovinin et al. (2003),

$$\sigma_I^2 = \int_0^{z_{\max}} \int_0^{\infty} \int_0^{\infty} f^{-8/3} \sin^2(\pi \lambda z f^2) A(f_x, f_y) C_n^2(z) \mathrm{d}f_x \mathrm{d}f_y \mathrm{d}z, \tag{2.16}$$

where the function $A(f_x, f_y)$ represents the aperture averaging function. This is the square modulus of the Fourier transform of the aperture function, $W(\mathbf{x})$. In figure 2.3 the effect of aperture size on the theoretical scintillation index for an example optical turbulence profile is plotted to demonstrate this effect.

2.4 Zernike polynomials

A principal method of mathematically describing the phase of an aberrated wavefront is its expansion in Zernike polynomials. First applied in the context of atmospheric optical turbulence in Noll (1976), the Zernike polynomials are a set of orthonormal functions on a unit circle, $Z_j(\mathbf{r})$, such that any distorted wavefront can be described by a sum of Zernike polynomials with coefficients a_j. Using polar coordinates, the wavefront phase $\phi(r,\theta)$ can be expressed as

$$\phi(r,\theta) = \sum_{j=1} a_j Z_j(r,\theta). \tag{2.17}$$

The functions $Z_j(\mathbf{r})$ are sorted by "Noll index" j, which is a combination the radial degree n and azimuthal frequency m. The first few Zernike polynomials correspond to common aberrations including piston ($j = 1$), tip and tilt ($j = 2, 3$) and defocus ($j = 4$) and so on.

$$Z_j(r,\theta) = \sqrt{n+1}\, R_n^m(r) \begin{cases} \sqrt{2}\cos(m\theta) & m \neq 0 \text{ and } j \text{ even}, \\ \sqrt{2}\sin(m\theta) & m \neq 0 \text{ and } j \text{ odd}, \\ 1 & m = 0. \end{cases} \tag{2.18}$$

$$R_n^m(r) = \sum_{s=0}^{(n-m)/2} \frac{(-1)^s (n-s)!}{s!\,\left(\frac{n+m}{2}-s\right)!\,\left(\frac{n-m}{2}-s\right)!} r^{n-2s}. \tag{2.19}$$

The orthonormality of the Zernike polynomials is expressed over the unit circle in the following way, which also leads to their normalisation,

$$\int W(\mathbf{r}) Z_j(\mathbf{r}) Z_{j'}(\mathbf{r}) \mathrm{d}\mathbf{r} = \delta_{jj'}, \tag{2.20}$$

$$W(r) = \begin{cases} 1/\pi & |\mathbf{r}| \leq 1, \\ 0 & |\mathbf{r}| > 1, \end{cases} \tag{2.21}$$

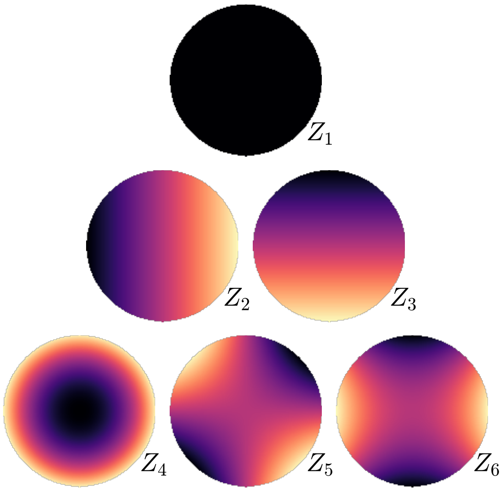

Figure 2.4: The first six Zernike polynomials ordered by Noll index.

where $\delta_{jj'}$ is the Kronecker delta. The Fourier transform of the Zernike polynomials Q_j is defined according to the following function,

$$W(\mathbf{r})Z_j(\mathbf{r}) = \int Q_j(\mathbf{f})e^{2\pi i\mathbf{f}\cdot\mathbf{r}}\mathrm{d}\mathbf{f}. \tag{2.22}$$

For a unit circle these functions are defined in Noll (1976). The Fourier representation of the Zernike polynomials is used by Noll to obtain a Zernike matrix representation of the Kolmogorov phase spectrum and predict the covariance of the coefficients $\langle a_j^* a_{j'}\rangle$ and the residual phase error after correcting for low order polynomials up to a given Noll index J. The residual phase error is expressed as a function of the telescope aperture diameter, D, and the Fried parameter, r_0, describing the turbulence strength.

Figure 2.4 shows the first six low-order Zernike polynomials. These are associated with the classical aberrations: piston, x-tilt, y-tilt, defocus, oblique astigmatism and vertical astigmatism respectively.

2.4.1 Shack-Hartmann wavefront sensors

Measurement of the amplitude modulation due to atmospheric optical turbulence is easily accomplished from measurement of the intensity of the light with a simple light-collecting detector such as a CCD or photodiode. In order to access the phase information of the wavefronts however, slightly more complex optical instrumentation is required. The group of techniques encompassing wavefront phase characterisation are known as “wavefront sensors”. Examples of such techniques include the pyramid wavefront sensor (Ragazzoni, 1996) and curvature wavefront sensor (Roddier et al., 1988). This work will focus on the Shack-Hartmann wavefront sensor (SHWFS) (Platt and Shack, 2001). A SHWFS consists of an array of small lenses or microlens array (MLA), and a detector in the MLA focal plane. An unaberrated plane wave incident normal to the microlens array will produce a regular array of focal spots on the detector, however a distorted wavefront will cause those focal spots to deflect from these reference positions. Figure 2.5 shows how distorted wavefronts in a SHWFS will produce deflections in the focal spot positions.

The angular x and y deflection (on the sky) is related to the average gradient of the wavefront across the lenslet (Roddier, 1999) such that the wavefront angle of arrival in x, a_x, is given by

$$a_x = \frac{\lambda}{2\pi A} \int \frac{\partial \phi(\mathbf{r})}{\partial x} \mathrm{d}\mathbf{r}. \tag{2.23}$$

This angle-of-arrival is commonly referred to as the “gradient” or “G” tilt measurement, and is distinct from the “Z” tilt which is the least-squares fit of the Zernike tip or tilt to the wavefront across the aperture. An illustration of this distinction is found in figure 2.6.

Typically the deflection will be measured in detector pixels, it is therefore important to characterise the angular pixel scale of the SHWFS in order to make use of the

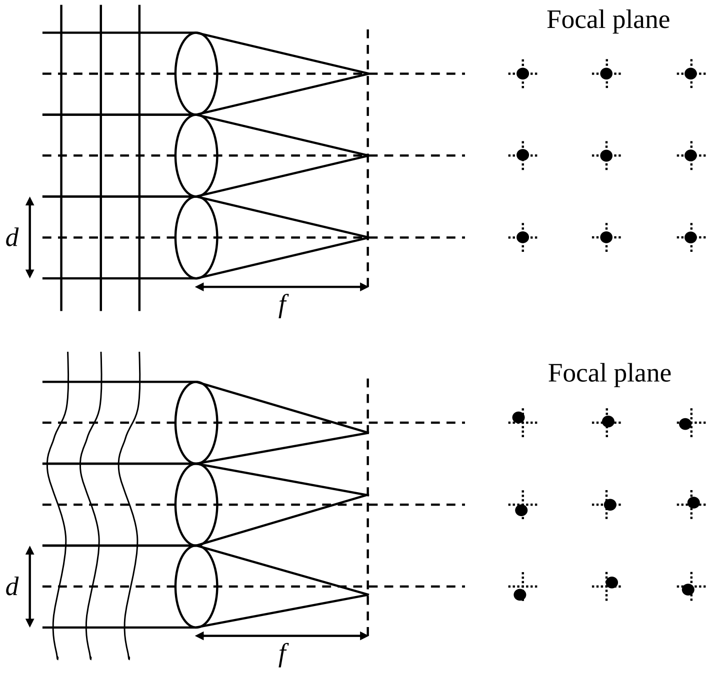

Figure 2.5: Operating principles of a Shack-Hartmann wavefront sensor showing the reference positions of the focal spots produced by a plane wave compared to the deflected spots when the wavefront is distorted.

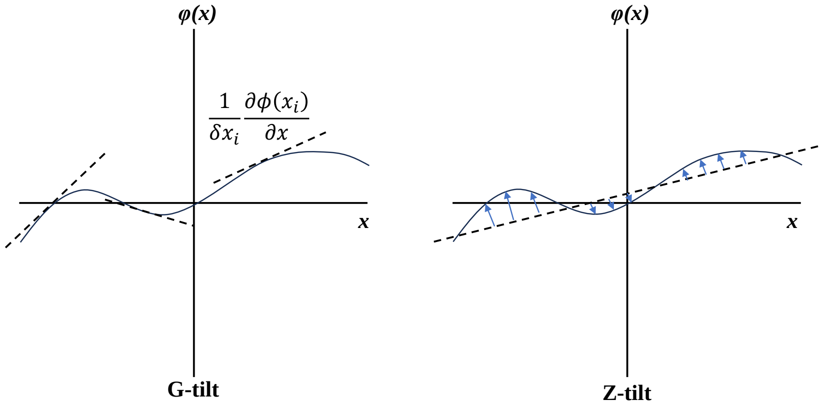

Figure 2.6: Plot of wavefront phase across an aperture in one dimension illustrating the difference between G-tilts (left) with the gradient averaged across the aperture and Z-tilts (right) which are the least square fitting of the Zernike tilt to the wavefront.

data. The SHWFS therefore provides a set of discrete measurements of the average wavefront gradient, which will be referred to as the “slope”, across each of the microlens arrays. Referring again to Noll (1976) it is possible to write the first derivative of the Zernike polynomials as a sum of Zernike polynomials

$$\frac{\partial Z_j}{\partial x} = \sum_{j'} \gamma^x_{jj'} Z_{j'}. \tag{2.24}$$

In this way, a wavefront represented by a sum of Zernike polynomials, Z_j, with coefficients, a_j, will have a gradient given by the sum of expressions 2.24 multiplied by the coefficients, a_j. Given that a vector of slope measurements $\mathbf{s}_x$ may be obtained from the SHWFS measurements, and a model of the gradient is obtained by a linear sum of the gradient averaged over each microlens array $\partial_x \mathbf{Z}$, a least-squares optimisation problem can be solved to find the set of Zernike coefficients that best fits the data. Taking a vector of slope measurements $\mathbf{S}$, a vector of Zernike coefficients to be calculated $\mathbf{a}$ and a matrix of derivatives of Zernike polynomials $\mathbf{G}$,

$$\mathbf{S} = \mathbf{G}\mathbf{a}, \tag{2.25}$$

$$\mathbf{a} = \mathbf{G}^{\dagger}\mathbf{S}, \tag{2.26}$$

where the pseudo-inverse has been used to solve the inverse problem. This is a description of a “modal” approach to wavefront sensing (Roddier, 1999). Typically the number of modes that can be fit is of the order of the number of subapertures, despite having twice as many total measurements of the slopes. This is because in a SHWFS, the power spectrum of the phase sampled by the x and y slope measurements is identical (Roddier, 1999), and attempting to fit more Zernike modes risks ill-conditioning of the problem (Lane and Tallon, 1992; Takato et al., 1994) as the system is effectively underdetermined. However the Zernike gradients that make up $\mathbf{G}$ are not strictly orthonormal and some of the columns of $\mathbf{G}$ will therefore not be orthogonal. This effect is known as cross-coupling (Andrade et al., 2019) and in practice it further limits the number of recoverable Zernike coefficients.

2.4.2 Centroiding methods

In a SHWFS, the G-tilt across a sub-aperture is measured exactly by the simple centre-of-gravity centroid of the spot in the absence of noise or scintillation (Roddier, 1999)

$$c_x = \frac{\sum_{ij} I_{ij} x_{ij}}{\sum_{ij} I_{ij}}, \tag{2.27}$$

where i, j represent the grid positions of detector pixels sampling the sub-aperture image, and I_{ij} refers to the intensity of pixel i, j. Unfortunately, the simple centroid is sensitive to detector noise, and so in practice is not suitable for real systems. A number of other approaches are viable, these include thresholding techniques such as the thresholded centre-of-gravity (Thomas et al., 2006) or the brightest pixel algorithm (Basden et al., 2012). The former involves choosing a percentage of the brightest pixel value, subtracting this value and setting all negative pixels to zero and then performing a simple centroid. The latter involves finding the $\mathrm{N^{th}}$ brightest pixel in the sub-aperture and subtracting this value from the image, then setting negative pixels to zero and performing a simple centroid. Both methods can be expressed as

$$c_x = \frac{\sum_{I>I_T} (I - I_T) x}{\sum_{I>I_T} (I - I_T)}. \tag{2.28}$$

It has been found that the brightest pixel algorithm produces superior results in low signal-to-noise measurements (Basden et al., 2012). Assuming that the spots can be approximated by a 2D Gaussian curve, and that the centroid noise is Gaussian with a mean of zero, the theoretical contributions to the centroid noise variance in angle-of-arrival radians^2 from shot noise and detector read noise are (Thomas et al., 2006),

$$\sigma_{\mathrm{read}}^2 = \frac{1}{12}\frac{N_{\mathrm{r}}^2}{N_{\mathrm{ph}}^2} N_s^2 \rho_\alpha^2, \tag{2.29}$$

$$\sigma_{\mathrm{shot}}^2 = \frac{1}{8\ln 2}\frac{1}{N_{\mathrm{ph}}}\left(\frac{\lambda}{d}\right)^2 \rho_\alpha^2, \tag{2.30}$$

where N_{ph} is the number of photoelectrons from the star during an exposure, N_{r} is the RMS readout noise per pixel, λ the wavelength and d the subaperture width, ρ_α the angular pixel size, N_s is the number of pixels used in the thresholded centroid.

An alternative approach is the correlation method. This involves cross-correlating sub-aperture images with a reference image F_{w} - either a mean sub-aperture image or theoretical spot function - using the equation (Thomas et al., 2006),

$$c_x(x, y) = I \otimes F_{\mathrm{w}} = \sum_{i,j} I_{ij} F_{\mathrm{w}}(x_i + x, y_i + y). \tag{2.31}$$

The correlation can be evaluated rapidly using fast Fourier transforms (FFTs). The pixel coordinates of the point of maximum correlation give the spot centroid. Sub-pixel accuracy may be achieved either through centroiding the correlation matrix (Thomas et al., 2006) or by fitting a parabola to a small sub-region around the pixel of maximum correlation (Löfdahl, 2010).

2.5 Optical turbulence profiling

In this section, a review of the current range of well-known optical turbulence profiling techniques will be made. The list is by no means exhaustive, however particular attention is paid to novel turbulence monitoring technologies that may see increased utilisation in future years, instruments that are widely employed for site characterisation today and those most relevant to this work.

2.5.1 Differential Image Motion Monitor

The DIMM (Sarazin and Roddier, 1990) is the most widely employed turbulence monitoring technique and instruments can be found at the largest observatories around the world including Roque de Los Muchachos Observatory and Mount Teide, Paranal Observatory. The operating principle of the DIMM is simple, and is shown visually in figure 2.7. It consists of a small telescope with diameter D with a mask in the pupil plane consisting of two identical small circular apertures diameter d spaced a distance B apart such that $b = d/B$. A wedge prism ensures that the focused beam from each aperture is spatially separated on a sensor by imparting a tilt to the wavefront from each aperture. The DIMM then measures the tip/tilt motion of the two focal spots, and calculates the variance of differential centroid motions in both the transverse axis and the longitudinal axis (perpendicular and parallel to a line through the centres of the two apertures). The differential centroid motion eliminates tip/tilt motion induced by shaking of the telescope with the wind and errors in the star tracking over the course of the measurement. Initially Sarazin and Roddier (1990) give the theoretical centroid variance σ_d^2 that should result from a turbulence atmosphere with seeing ε_0, however subsequent investigation by Tokovinin (2002b) lead to the equations

$$\sigma_d^2 = K\lambda^2 r_0^{-5/3} d^{-1/3}, \tag{2.32}$$

where K is a constant which is different for longitudinal and transverse centroid variance, defined in Tokovinin (2002b) as

$$K_l = 0.364\left(1 - 0.532b^{-1/3} - 0.024b^{-7/3}\right), \tag{2.33}$$

$$K_t = 0.364\left(1 - 0.798b^{-1/3} - 0.018b^{-7/3}\right). \tag{2.34}$$

The DIMM instrument is simple, well characterised and reliable due to it’s simple two-aperture design. However it is limited only to measurements the integrated see-

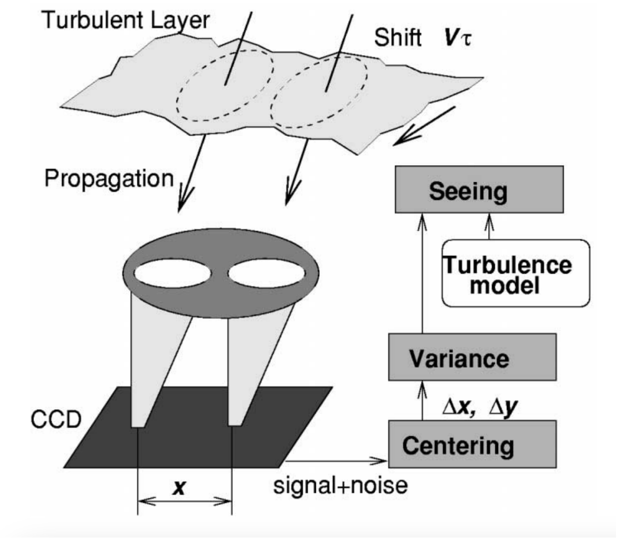

Figure 2.7: Operational principle of the DIMM showing light passing through a turbulent layer and arriving at the two-aperture mask of the DIMM. The differential motion of the two focal spots is then analysed to extract the seeing. Reproduced from Tokovinin (2002b).

ing and does not account for the small changes in the power spectrum of turbulence from higher-altitude layers as a result of optical propagation.

2.5.2 Multi Aperture Scintillation Sensor

The MASS (Kornilov et al., 2003) is another small-telescope based turbulence monitor. The MASS uses an optical assembly of four concentric mirrors to collect light from four concentric annular apertures (figure 2.8). It measures the normalised intensity fluctuations resulting from propagation though turbulence i.e. the scintillation index, in those four apertures using photomultiplier tubes. Using the theory described by Tokovinin et al. (2003), weighting functions are generated for the 10 (4 normal and 6 differential) scintillation indices at vertical heights of 0, 0.5, 1, 2, 4, 8, 16 km and an inversion algorithm is used to reconstruct the $C_n^2(h)\,\mathrm{d}h$ of each layer by solving the inverse problem,

$$\mathbf{S} = \mathbf{W}\mathbf{J}, \tag{2.35}$$

where **S** is a vector of scintillation index measurements, **W** is a matrix of weighting functions, each of which is equivalent to the (differential) scintillation index response for a thin layer of turbulence at a given height, and **J** is the vertical profile of optical turbulence strength $C_n^2(h)\,\mathrm{d}h$.

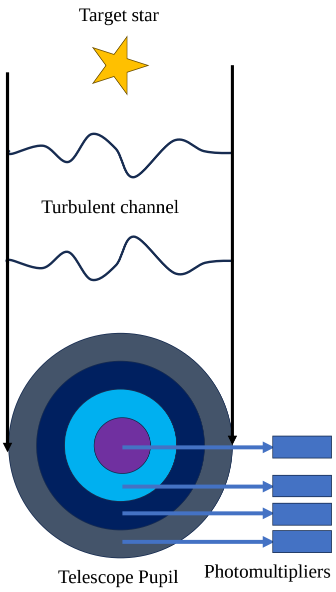

Figure 2.8: Operational principle of the MASS instrument showing measurement of the intensity fluctuations in the pupil of a telescope by four concentric mirrors and photomultiplier tubes.

The weighting functions for the normal and differential scintillation indices follow from equation 2.16, where the aperture averaging function $A(f)$ for the differential indices is replaced by the modulus squared of the difference between the Fourier transforms of the two aperture functions (Tokovinin, 2002a). As stated before, the scintillation produced by low-altitude turbulence is challenging to detect, and there is no scintillation for ground-level turbulence. The MASS can account for this using the generalised Scintillation Detection and Ranging (SCIDAR) technique of conjugating the instrument to a negative altitude (defocusing) - inducing propagation of the wavefronts. However this poses additional constraints on performance due to diffraction from the aperture (Tokovinin et al., 2003). In practice, the MASS is typically combined with the DIMM on a single telescope to form a MASS-DIMM, combining MASS profiles with the integrated seeing measurements from the DIMM to increase sensitivity to ground-layer optical turbulence.

The MASS is therefore able to compute additional turbulence parameters over the DIMM such as the Rytov variance and isoplanatic angle. The coherence time however requires knowledge of the wind speed of each layer. This may be obtained by the method described in Kornilov (2011a) of including a wind shear component in the weighting functions (Kornilov, 2011b). Then by taking continuous exposures without gaps, and using a fitting process the second moment of the wind, $\overline{V}_2$, may be estimated. The approximation of $\overline{V}_2 \approx 1.1\overline{V}_{5/3}$ found by Kellerer and Tokovinin (2007) then leads to an estimate of the coherence time. The MASS is however based around a design using photomultiplier tubes and customised optics making it difficult to produce new units.

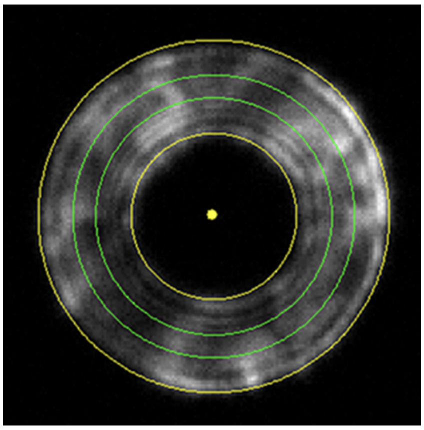

Figure 2.9: An example image from the full aperture scintillation sensor (FASS) instrument of the telescope pupil. The green rings describe the range of radii at which the annular power spectrum of intensity will be computed. The edges of the pupil are shown in yellow. Reproduced from Guesalaga et al. (2021).

2.5.3 Full aperture scintillation sensor

The FASS (Guesalaga et al., 2016, 2021) images the scintillation produced in the pupil plane of a telescope, again optionally defocusing the instrument to gain sensitivity to the scintillation from low-altitude turbulence as in the MASS. Instead of intensity covariances, the FASS calculates the annular power spectra of the scintillation in concentric rings within the telescope aperture. This data is then compared to simulated results in a similar equation to 2.35 in order to compute the turbulence $C_n^2(h)\,\mathrm{d}h$ profile for 14 individual layers arranged on a logarithmic scale of height. An example image from the instrument is given in figure 2.9. The FASS is able to measure a large number of layers considering the telescope aperture size, however until the generalised version of the instrument has been perfected it is insensitive to the ground layer of optical turbulence.

2.5.4 Ring Image Next-Generation Scintillation Sensor

Ring image next-generation scintillation sensor (RINGSS) is a turbulence profiler developed to replace the technically obsolete MASS instruments (Tokovinin, 2021). It uses a 5-inch Celestron telescope where an image of a bright single star is optically transformed into a ring (figure 2.10). This is achieved by combination of spherical aberration and defocus in the focal-reducer lens. The pixel scale is 1.57 arcsec and the ring radius is 11 pixels. Cubes of 2000 ring images of 48×48 pixel format and 1 ms exposure time are recorded by a CMOS camera. Image processing consists in centering the rings and computing 20 harmonics of intensity variation along the ring (in the angular coordinate). Variances of these harmonics, averaged over 10 image cubes, are related to the turbulence profile by means of weighting functions in the same way as in MASS. RINGSS delivers turbulence integrals in eight layers at 0, 0.25, 0.5, 1, 2, 4, 8, 16 km heights. The results are corrected to zenith. They are also corrected for the finite exposure time bias and partially corrected for deviations from the weak scintillation regime (saturation). The atmospheric time constant is determined by the method of Kornilov (2011a), similar to MASS. The instrument operates robotically. Its control provides for selection and change of targets, pointing and centering, and closed-loop focus control. Scintillation signals in RINGSS are sensitive to the ground-layer turbulence because the image is not focused, similar to the generalised SCIDAR technique. Alternative estimation of seeing is made using radial distortions of the rings, like in a DIMM. This "sector" seeing agrees reasonably well with the scintillation-based seeing.

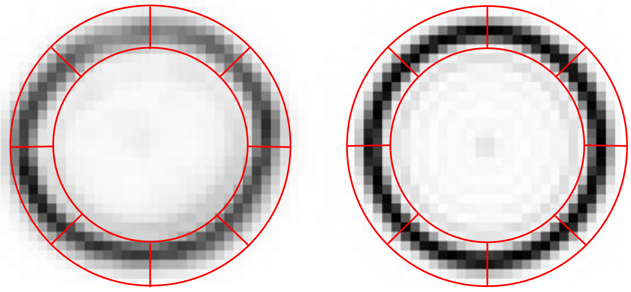

Figure 2.10: Example of simulated data from the RINGSS instrument showing an undistored ring image (right) divided into eight sectors and a distorted image (left). Both the sector distortions and the intensity fluctuations within the ring image are visible, each of which can give a separate measurement of the seeing. Adapted from Tokovinin (2021).

2.5.5 Scintillation Detection and Ranging

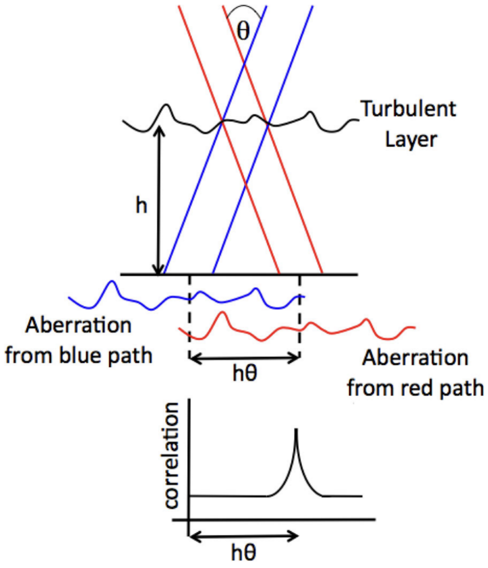

Figure 2.11: Stereo-SCIDAR measurement principle showing the triangulation method leading to a shift in the intensity correlation peak proportional to the height of the layer h and the binary separation angle θ. Reproduced from Shepherd et al. (2014).

SCIDAR (Fuchs et al., 1998) is the first of the “crossed beams” techniques. Instead of slopes, SCIDAR measures only the re-imaged intensity pattern in the telescope pupil plane from a binary star system. In the typical implementation, the images are overlapped on a single camera. However in the case of stereo-SCIDAR (Shepherd et al., 2014), a prism is used to project the two binary patterns onto two different cameras, yielding advantages in sensitivity. The cross covariance of the spatial intensity fluctuations in the two pupil images is analysed to extract a high-resolution optical turbulence $C_n^2(h)\,\mathrm{d}h$ profile comprised of 100 layers at 250 m intervals as shown in figure 2.11. Additionally, by analysing the temporal evolution of the cross-covariance responses, it is possible to extract the wind velocity and direction of individual turbulent layers which enables estimation of the optical turbulence coherence time. Stereo-Scintillation Detection and Ranging (S-SCIDAR) requires a far larger telescope aperture, typically on the order of 1-2 m both to achieve a high resolution and to reduce aperture diffraction effects resulting from propagation. In recent years, improvements have been made to the S-SCIDAR analysis techniques which can correct for wind speed and finite spatial sampling effects, increasing accuracy of the measurements (Butterley et al., 2020a).

2.5.6 Slope Detection and Ranging

slope detection and ranging (SLODAR) (Wilson, 2002) is another triangulation technique that uses Shack-Hartmann observations of binary stars systems to reconstruct the $C_n^2(h)\,\mathrm{d}h$ profile at high vertical resolutions. SLODAR calculates the cross-covariances and auto-covariances of wavefront angle-of-arrival slopes from the two SHWFS spot patterns, given by

$$C_x(\delta i, \delta j) = \left\langle \sum_{i,j} s^x_{i,j} s'^x_{i+\delta i, j+\delta j} / O(\delta i, \delta j) \right\rangle, \tag{2.36}$$

$$A_x(\delta i, \delta j) = \left\langle \sum_{i,j} s^x_{i,j} s^x_{i+\delta i, j+\delta j} / O(\delta i, \delta j) \right\rangle, \tag{2.37}$$

where i, j are points on the sub-aperture grid, $\delta i, \delta j$ are separations on the grid in subaperture units, $O(\delta i, \delta j)$ is the number of valid sub-apertures separated by

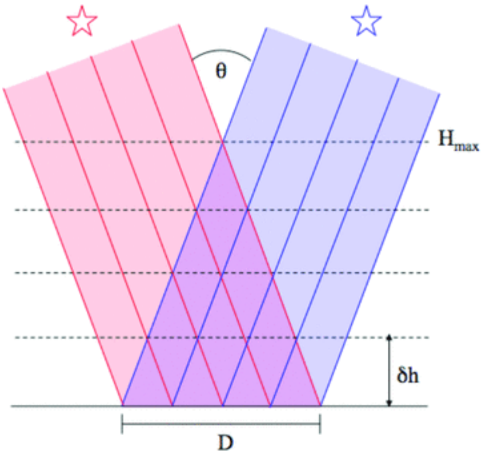

Figure 2.12: SLODAR diagram showing wavefronts from two binary stars with a separation θ overlapping at the telescope pupil of diameter D after passing through a number of layers. Reproduced from Osborn et al. (2010).

$(\delta i, \delta j)$ and $s^x_{i,j}$, $s'^x_{i,j}$ represent the x-slope measurements for stars 1 and 2 respectively in the sub-aperture (i, j). The auto-covariance is essentially the average of all terms in the covariance matrix with the same separation on the sub-aperture grid.

Use of slope information is advantageous as the slopes are sensitive to low-altitude turbulence. Impulse functions are computed through numerical integration of the turbulence power spectrum (making assumption of no propagation effects) and are fit to the data via a deconvolution (Butterley et al., 2006). A single layer at height H for a binary separation of θ_b will produce a peak in the cross-covariance shifted by $H\theta_b$, as shown by the crossed beams diagram in figure 2.12. This results in a vertical resolution of $\delta h = d/\theta_b$ for Shack-Hartmann sub-apertures of size d, and a maximum altitude given by the number of sub-apertures multiplied by the resolution. SLODAR may also fit non-Kolmogorov turbulence and allow calculation of outer scale (Goodwin et al., 2007). By careful choice of binary separations and SHWFS geometry the SLODAR may also give high vertical resolution in the first kilometre, as in the surface layer SLODAR at Paranal (Osborn et al., 2010; Butterley et al., 2020b). The limitations of SLODAR include firstly that sub-apertures much be relatively large to give a sufficiently small angular spot size to sense positional fluctuations due to atmospheric turbulence. Secondly, the SLODAR impulse functions do not account for optical propagation meaning that measurements for high altitude layers will be slightly biased.

2.5.7 (Single) Coupled SLODAR - SCIDAR

The final crossed-beams technique is CO-SLIDAR, the theoretical treatment of which is highly influential on later chapters in this work. The instrument is similar to a SLODAR in optical design as a Shack-Hartmann based optical turbulence profiler. There are however fundamental differences between the two in the analysis method and as the CO-SLIDAR utilises intensity information from the Shack-Hartmann in addition to slope measurements. The CO-SLIDAR starts with the following modifications to the weak scintillation functions for amplitude and phase in an arbitrary aperture equation 2.5, 2.6 (Robert et al., 2006),

$$\iota(\mathbf{x},\boldsymbol{\alpha}) = 2\phi(\mathbf{x}) * \frac{1}{\lambda z}\cos(\frac{\pi\mathbf{x}^2}{\lambda z}) * W(\mathbf{x}) * \delta(\mathbf{x}-\boldsymbol{z\alpha}), \tag{2.38}$$

$$s_\zeta(\mathbf{x},\boldsymbol{\alpha}) = -\frac{\lambda}{2\pi}\frac{\partial\phi(\mathbf{x})}{\partial\zeta} * \frac{1}{\lambda z}\sin(\frac{\pi\mathbf{x}^2}{\lambda z}) * W(\mathbf{x}) * \delta(\mathbf{x}-\boldsymbol{z\alpha}), \tag{2.39}$$

where $\boldsymbol{\alpha}$ indicates the angle of the observation of a point source $\boldsymbol{\alpha}$ and $\zeta = \{x, y\}$. s_ζ refers to the wavefront G-tilt angle-of-arrival slope in the x or y axis, $W(\mathbf{x})$ represents the aperture function and is given by,

$$W(\mathbf{x}) = \begin{cases} 1 & |x| \le \frac{d}{2}, |y| \le \frac{d}{2}, \\ 0 & \text{otherwise.} \end{cases} \tag{2.40}$$

Finally $\iota(\mathbf{x})$, for a single frame k, is equivalent to

$$\iota_k = \frac{I_k}{\langle I\rangle} - 1, \tag{2.41}$$

where the angular brackets denote an average over many frames, such that $\mathrm{Var}[\iota] = \langle\iota^2\rangle$ is the scintillation index σ_I^2. It therefore refers to the normalised intensity fluctuation in a subaperture k with shape $W(\mathbf{x})$ at position $\mathbf{x}$. For a point source on-axis, the delta function may be dropped and the system is now known as single coupled SLODAR-SCIDAR (SCO-SLIDAR) (Védrenne et al., 2007). This formulation is more relevant to this work and will be considered from here onwards.

Calculation of the spatial power spectrum of the two expressions in equation 2.38 is now straightforward and reduces to a product of the Fourier transforms of the individual components. For calculation of the power spectrum of the phase, a $C_n^2(h)\,\mathrm{d}h$ of unity is substituted yielding final expressions for the power spectra,

$$|\mathcal{F}\left[\iota(\mathbf{x})\right]|^2 = 4\Phi_K(\mathbf{f})\sin^2\left(\pi\lambda z f^2\right)A(\mathbf{f}), \tag{2.42}$$

$$|\mathcal{F}\left[s_\zeta(\mathbf{x})\right]|^2 = \left(\frac{\lambda}{2\pi}\right)^2 f_\zeta^2\Phi_K(\mathbf{f})\cos^2\left(\pi\lambda z f^2\right)A(\mathbf{f}), \tag{2.43}$$

where $\mathbf{f}$ is the two-dimensional spatial frequency with components (f_x, f_y) and $f = ||\mathbf{f}||_2$, $\Phi(\mathbf{f})$ the power spectrum of phase fluctuations for a $C_n^2(h)\,\mathrm{d}h$ of unity and $A(\mathbf{f})$ is the aperture filter function in this case for a single square Shack-Hartmann aperture of width d

$$A(\mathbf{f}) = \mathrm{sinc}^2(\pi d f_x)\,\mathrm{sinc}^2(\pi d f_y). \tag{2.44}$$

The Wiener–Khinchin theorem can then be used to give an analytical expression for the spatial auto-covariance of the normalised intensity fluctuations, ι and angle-of-arrival slopes s_ζ measured in the Shack-Hartmann apertures (Védrenne et al., 2010),

$$\mathcal{I}(\mathbf{w}, z) = \langle \iota_{ij}\iota_{i'j'}\rangle = 4\int_{-\infty}^{\infty}\Phi_K(\mathbf{f})\sin^2\left(\pi z\lambda f^2\right)A(\mathbf{f})\exp\left(2\pi i\mathbf{w}\cdot\mathbf{f}\right)\mathrm{d}\mathbf{f}, \tag{2.45}$$

$$\mathcal{S}_\zeta(\mathbf{w}, z) = \langle s_{\zeta,ij}s_{\zeta,i'j'}\rangle = \left(\frac{\lambda}{2\pi}\right)^2\int_{-\infty}^{\infty}f_\zeta^2\Phi_K(\mathbf{f})\cos^2\left(\pi z\lambda f^2\right)A(\mathbf{f})\exp\left(2\pi i\mathbf{w}\cdot\mathbf{f}\right)\mathrm{d}\mathbf{f}, \tag{2.46}$$

where $\mathbf{w}$ is a spatial offset. $(i, j), (i', j')$ denote two positions on the sub-aperture grid separated by $\mathbf{w} = (d(i - i'), d(j - j'))$. The above equation may be solved numerically using an inverse fast Fourier transform. Including oversampling in the frequency domain is essential to avoid aliasing at the edges of the IFFT and increases the accuracy of the calculation. These equations are referred to as the "weighting functions".

These equations follow from considering the response to a single turbulent layer. For multiple turbulent layers at fixed heights $\mathbf{z} = (z_1, z_2...z_n)$, a model of the intensity covariances can be constructed, returning to the weak turbulence approximation, where the total covariance measured at the ground is a linear sum of the auto-covariance responses for a unit $C_n^2(h)\,\mathrm{d}h$. These will now referred to as the weighting functions. Writing the offset between two sub-apertures as $\mathbf{w}_{\delta i \delta j}$ where $\delta i = (i - i'), \delta j = (j - j')$, the covariance between two sub-apertures for a multi-layer atmosphere can be written as a linear sum of the weighting functions,

$$\langle \iota_{ij} \iota_{i'j'} \rangle = \sum_{m=1}^{n} \mathcal{I}(\mathbf{w}_{\delta i \delta j}, z_m) C_n^2(z_m) \mathrm{d}z, \tag{2.47}$$

$$\langle s_{ij}^x s_{i'j'}^x \rangle = \sum_{m=1}^{n} \mathcal{S}_x(\mathbf{w}_{\delta i \delta j}, z_m) C_n^2(z_m) \mathrm{d}z, \tag{2.48}$$

$$\langle s_{ij}^y s_{i'j'}^y \rangle = \sum_{m=1}^{n} \mathcal{S}_y(\mathbf{w}_{\delta i \delta j}, z_m) C_n^2(z_m) \mathrm{d}z. \tag{2.49}$$

Combining the covariances of the intensities, x-slopes and y-slopes into a single vector and forming a matrix of weighting functions where the rows correspond to the sub-aperture pairs and the columns to the heights $\mathbf{z}$, this system can be written in the same form as equation 2.35.

2.6 Optical turbulence parameters

Given an optical turbulence profile $C_n^2(z)$ there exist a number of critical parameters that are useful in modelling the performance of optical systems and in particular adaptive optics systems. Assuming an effectively flat Earth and parallel layers of optical turbulence with thickness dh in the atmosphere, an observation made at an angle γ to the zenith will image through more turbulence and experience longer propagation distances. In this work the common simple geometrical correction $z = h\sec(\gamma)$ as in Hufnagel and Stanley (1964) is adopted, rather than more complex approaches such as Kasten and Young (1989). This is critical to derivations of the following parameters.

The first and most important optical turbulence parameter is the so-called Fried parameter, r_0. This parameter was derived by Fried (1965), and is a physical limit such that a telescope with a diameter $D \gg r_0$ will have a resolution limited by the atmosphere, whereas $D \ll r_0$ will be diffraction limited (Roddier, 1981). This parameter is also called the coherence length, and is effectively a measure of the turbulence strength of the whole atmosphere,

$$r_0 = \left[0.423k^2 \sec(\gamma) \int_0^\infty C_n^2(h)\mathrm{d}h\right]^{-3/5}. \tag{2.50}$$

Larger values indicate weaker turbulence and smaller values stronger turbulence. The Fried parameter therefore scales with wavelength, $r_0 \propto \lambda^{6/5}$, which implies that turbulence will appear weaker for imaging at longer wavelengths. The Fried parameter may also be directly related to the “astronomical seeing”. Seeing describes the amount of image distortion in the PSF resulting from atmospheric optical turbulence and is the angular size of the long-exposure PSF for a telescope imaging through optical turbulence. The astronomical seeing is defined as,

$$\varepsilon_0 = 0.98\frac{\lambda}{r_0}, \tag{2.51}$$

and is in practice always greater than the angular size of the diffraction limited PSF for large telescopes.

Another quantity of interest is the Rytov variance, that is the scintillation index measured by a point receiver and therefore a measure of the strength of scintillation

(Andrews and Phillips, 2005). The form of the Rytov variance for plane waves can easily be deduced from equation 2.16 if the aperture function is set to the Dirac delta function. The integration then yields

$$\sigma_R^2 = 19.12\lambda^{-7/6}\sec^{11/6}(\gamma)\int_0^\infty h^{5/6}C_n^2(h)\mathrm{d}h, \tag{2.52}$$

indicating a dependence on both the height distribution and strength of optical turbulence. This is expected as low-altitude turbulence should produce little scintillation. The Rytov variance is also an indicator for deviation from the weak scintillation regime implied by equation 2.2, where $\sigma_R^2 \leq 0.3$ corresponds to weak scintillation, $\sigma_R^2 \approx 1$ to medium scintillation and $\sigma_R^2 \gg 1$ to strong scintillation (Andrews and Phillips, 2005).

The isoplanatic angle, or coherence angle, is another parameter that is dependent on the height distribution of optical turbulence. It is defined as (Roddier, 1981)

$$\theta_0 = \left[2.91k^2\cos^{-8/3}(\gamma)\int_0^\infty C_n^2(h)\,h^{5/3}\mathrm{d}h\right]^{-3/5}. \tag{2.53}$$

The isoplanatic angle defines the angular separation between two stars observed through optical turbulence at which the wavefront error between the incoming light from each star will be equal to 1 rad^2. It describes the degree of anisoplanatism, that is the difference between the turbulence along the path between the two stars. This effect has particular importance in AO where an off-axis natural guide star is used to provide wavefront corrections for observation of a faint target star. As a result of anisoplanatism, the wavefront correction along one path will not fully correct turbulence along the second path. The isoplanatic angle is small, typically measured in arcseconds, and therefore significantly constrains the number of valid natural guide stars or the maximum angular separation of a laser guide star for AO.

The optical turbulence coherence time, τ_0, is the limit of time delay in an adaptive optics system at which the RMS wavefront error will equal 1 rad^2. Assuming frozen flow, the turbulent layers imaged by an adaptive optics system will be moving across the aperture with wind speeds $V(h)$. The adaptive optics will take a short exposure to image the turbulence and calculate a corresponding correction to the deformable mirror after which time the turbulence has moved. This therefore introduces error in the correction as the turbulence has evolved since the images were taken. This leads to the notion of a coherence time, defined as (Roddier, 1981; Kellerer and Tokovinin, 2007).

$$\tau_0 = 0.314 \frac{r_0}{\overline{V}_{5/3}}, \tag{2.54}$$

where $\overline{V}_{5/3}$ is the weighted mean of the wind speed raised to the power of 5/3,

$$\overline{V}_{5/3} = \left[\frac{\int_0^\infty V(h)^{5/3} C_n^2(h)\,\mathrm{d}h}{\int_0^\infty C_n^2(h)\,\mathrm{d}h} \right]^{3/5}. \tag{2.55}$$

Assuming a perfect deformable mirror and optics, an adaptive optics system will suffer from the fundamental limitations of time delay and ansioplanatism in the following way,

$$\sigma^2 = \sigma^2_{\mathrm{time}}(\tau) + \sigma^2_{\mathrm{aniso}}(\theta) = \left(\frac{\tau}{\tau_0}\right)^{5/3} + \left(\frac{\theta}{\theta_0}\right)^{5/3}. \tag{2.56}$$

This illustrates the usefulness of these two parameters in particular in determining the number of usable natural guide star targets and the viable bandwidth of the AO system for a given site.

2.7 Inverse problems

A number of inverse problems have already been discussed in this chapter, including the modal reconstruction of wavefronts with Zernike polynomials and in the operating principles of a number of turbulence monitoring instruments. This section will summarise methods of solving inverse problems and ill-conditioned inverse problems. For discrete, linear inverse problems, knowledge of the model and measurements is known, but the solution to the system is unknown. In a matrix formulation this is expressed as

$$\mathbf{A}\mathbf{x} = \mathbf{b}, \tag{2.57}$$

where $\mathbf{b}$ is a vector of m measurements, $\mathbf{A}$ is an $m \times n$ matrix where n is the number of fitting parameters. $\mathbf{A}$ is known as the design matrix and maps the vector of unknown coefficients $\mathbf{x}$ onto the measurements. In most physical systems, measurements cannot be made without being affected by some noise, therefore $\mathbf{b} = \mathbf{b}' + \mathbf{e}$ where the vector $\mathbf{e}$ represents the noise on the measurements and $\mathbf{b}'$ are the true measurements without noise present.

2.7.1 Least squares solution

To solve equation 2.57 for $\mathbf{x}$, the problem can be simplified by assuming zero-noise, i.e. the term $\mathbf{b} = \mathbf{b}'$. If $m > n$ then the system is overdetermined and there is no exact solution to equation 2.57. Instead we look for the best available solution which minimises the square of the euclidean norm of the residuals

$$\arg\min\{||\mathbf{A}\mathbf{x} - \mathbf{b}||_2^2, \} \tag{2.58}$$

which is the least squares solution to equation 2.57. In this case the pseudo-inverse of the design-matrix can be used to find the least-squares solution $\mathbf{A}^{\dagger}\mathbf{b} = \mathbf{x}$.

In cases where, for physical reasons, only positive solutions $\mathbf{x} \geq 0$ are valid (as in the profile of atmospheric turbulence strength), the pseudoinverse cannot be used. This class of problem is know as non-negative least squares (NNLS) and may be solved using iterative methods such as the NNLS active-set method described in Lawson and Hanson (1995) or the bounded variable least squares (BVLS) (Stark and Parker, 1995) algorithm which allows for general constraints in linear least squares problems.

2.7.2 Maximum likelihood estimation

Given some knowledge of the uncertainties in the measurement $\mathbf{b}$, equation 2.57 can also be solved with maximum-likelihood estimation, a detailed derivation of which can be found in Aster et al. (2013). The advantage of this method is that it takes into account the measurement errors $\mathbf{e}$. The likelihood function $L(\mathbf{x}|\mathbf{b})$ represents the probability of a model $\mathbf{x}$ leading to the observed data $\mathbf{b}$. This is equivalent to the joint probability density of all observations. If we assume that the errors in the data are normally distributed with a mean of 0 and standard deviation e_i, then the likelihood function can be written as the product of individual likelihoods of each point in $\mathbf{b}$,

$$L(\mathbf{x}|\mathbf{b}) \propto \prod_{i=1}^{m} \exp\left[-(b_i - (\mathbf{A}\mathbf{x})_i)^2/2e_i^2\right]. \tag{2.59}$$

By maximising the likelihood function we are able to obtain the most likely model $\mathbf{x}$ which has produced the observed data $\mathbf{b}$. By taking the logarithm of equation 2.59, the log-likelihood function is obtained,

$$\arg\max_{\mathbf{x}} \sum_{i=1}^{m} -\frac{(b_i - (\mathbf{A}\mathbf{x})_i)^2}{2e_i^2}, \tag{2.60}$$

where dropping the sign and constant leaves us with the weighted least squares solution to equation 2.57

$$\arg\min_{\mathbf{x}} \sum_{i=1}^{m} \frac{(b_i - (\mathbf{A}\mathbf{x})_i)^2}{e_i^2}. \tag{2.61}$$

This can be re-formulated by defining a diagonal matrix $\mathbf{C}_\varepsilon = \text{diag}\{1/e...1/e_m\}$ and two new matrices $\mathbf{W}_\varepsilon = \mathbf{C}_\varepsilon\mathbf{W}$, $\mathbf{b}_\varepsilon = \mathbf{C}_\varepsilon\mathbf{b}$ into a similar form to equation 2.58

$$\arg\min_{\mathbf{x}\geq 0}\{||\mathbf{A}_\varepsilon\mathbf{x} - \mathbf{b}_\varepsilon||_2^2\}, \tag{2.62}$$

to which standard solution techniques such as the BVLS and NNLS can be applied for solving for $\mathbf{x}$. A secondary advantage of the weighted least squares formulation is that is allows for a simple calculation of the covariance matrix of fitting errors

$$C_{\mathbf{x}} = \left(\mathbf{A}_{\varepsilon}^{T}\mathbf{A}_{\varepsilon}\right)^{-1}, \tag{2.63}$$

where the diagonal values of $C_{\mathbf{x}}$ is a vector $\sigma_x^2 = (\sigma_{x_0}^2 \dots \sigma_{x_n}^2)$ representing the error variance in the solution for $\mathbf{x}$ obtained from least squares. In practice, solving an inverse matrix like equation 2.63 is computationally slow and so the inverse is approximated by the pseudoinverse.

2.7.3 Ill-conditioned problems and Regularisation

The notion of a well-posed problem is attributed to Hadamard, who stated that such a problem should meet the following criteria,

- A unique solution to the problem exists.
- The solution should be stable and depend continuously on the data.

A problem which does not conform to this description may be considered ill-conditioned. An ill conditioned problem refers to an inverse problem where the singular values of the design matrix decay to zero (Hansen and O'Leary, 1993), inferring that the matrix is becoming singular and that the system is highly susceptible to perturbations in the data caused by noise. The principal method of finding the best solution in such cases is Tikhonov regularisation, also known as ridge regression (Tikhonov et al., 1995). Regularisation methods seek to stabilise the solution in the presence of noise, Tikhonov regularisation achieves this through the damped least squares formulation (Aster et al., 2013)

$$\arg\min\{||\mathbf{A}\mathbf{x} - \mathbf{b}||_2^2 + \alpha^2||\mathbf{L}\mathbf{x}||_2^2\}. \tag{2.64}$$

There are in theory a large number of possible least squares solutions due to the presence of data noise. Minimising the residuals alone is therefore likely to fit to the noise. The best solution will come from balancing the size of the solution norm with a suitably small residual norm. In equation 2.64, α is known as the regularisation parameter, and choice of its value is critical to maintaining the optimal balance between the solution and residual norms. The second new parameter is a matrix **L**, referred to as the roughening matrix. In standard Tikhonov regularisation **L** is the identity matrix, which results in equation 2.64 penalising large solution norms. Alternatively, **L** can be chosen to minimise the first or second derivatives of the solution, thereby enforcing a preference for "flat" or "smooth" solutions respectively. This is accomplished via the finite differences approximations (Aster et al., 2013)

$$\mathbf{L_1} = \begin{bmatrix} -1 & 1 & & & \\ & -1 & 1 & & \\ & & \ddots & \ddots & \\ & & & -1 & 1 \end{bmatrix}, \quad \mathbf{L_2} = \begin{bmatrix} -1 & 2 & 1 & & & \\ & -1 & 2 & 1 & & \\ & & \ddots & \ddots & \ddots & \\ & & & -1 & 2 & 1 \end{bmatrix}. \tag{2.65}$$

Two popular methods of choosing the regularisation parameter include the Morozov discrepancy principle (Fromovitz, 1986), and the L-curve method (Hansen, 1992). For the former, knowledge of the noise level in the measurements δ is necessary as the value of the regularising parameter is chosen such that the size of the residuals does not exceed this, $||\mathbf{Ax} - \mathbf{b}||_2^2 \leq \delta$. In the latter, we rely on the fact that as α increases, the system pivots from producing small residuals and a large norm to a small norm and larger residuals. This results in a characteristic L-shaped plot on a logarithmic axes of the residual norm plotted against the solution norm. The corner of the L-shaped curve indicates the optimal value of α where the two are finely balanced.

CHAPTER 3

Single-star Shack-Hartmann optical turbulence profiling techniques for the SHIMM

3.1 Introduction

Optical turbulence monitoring instruments have been widely adopted at astronomical observatories since the emergence of the DIMM in the 1980s. Site monitoring continues to play a critical role in observatory operations and for selection of new sites. The vast majority of active dedicated monitors are DIMM instruments due to their simplicity and reliability. However, following on from the success of the MASS, the demand for a more detailed characterisation beyond only the seeing has grown. Measurements of parameters such as the coherence time and isoplanatic angle are of great importance in defining the requirements for an adaptive optics system at any site. Furthermore, knowledge of the vertical distribution of optical turbulence will be crucial for predicting and verifying the performance of multi-conjugate adaptive optics (MCAO) systems planned for 20-40 m ELT-class telescopes (Costille and Fusco, 2011; Tokovinin, 2010). These systems will demand instruments that measure both "integrated" parameters relevant to AO and the vertical distribution of optical turbulence. Turbulence profiles are also important for the validation of meso-scale turbulence forecasting models (Masciadri et al., 2020), and for data assimilation activities such as auto-regression (Masciadri et al., 2023). Such models offer potential gains in scheduling efficiency which will be highly beneficial to both the operation of ELT-class instruments and for selecting sites for the optical ground station networks of the future (Osborn et al., 2023). As a result, considerable effort has been made to develop robust analysis techniques for the SHIMM instrument to provide accurate measurements of the integrated parameters (r_0, θ_0 etc.) and turbulence profiles while retaining a simple Shack-Hartmann optical design. These techniques are agnostic as to whether they are used during the day or night provided that the image processing algorithms are able to account for the increased level of instrument noise.

This chapter will focus on the theoretical basis underpinning the SHIMM optical turbulence profiling techniques. This work is largely based on the familiar inverse problem linking a series of weighting functions described by weak-scintillation theory and statistical measurements of optical turbulence slopes and scintillation. This is specifically focused on extending the approach developed for the SCO-SLIDAR instrument and adapting it to better suit measurements from a small telescope profiler such as the SHIMM. This work identifies a novel method of generating Z-tilt slope weighting functions using Fourier transforms, sets out corrections that can be made to the inverse problem to account for non-zero exposure time, a finite outer scale and for the disruptive effects of dome seeing. Most discussion will be in the context of the Shack-Hartmann geometry of the SHIMM instrument, namely 6 x 6 sub-apertures on an 28 cm telescope operating in the SWIR. However, these techniques could apply to any Shack-Hartmann system - even sensors integrated into adaptive optics in open-loop or even pseudo-open-loop given that the deformable mirror shape can be retrieved accurately in closed-loop. Therefore such techniques can provide “free” turbulence profiling at existing large telescopes.

3.2 Scintillation weighting functions

Scintillation weighting functions follow directly from the weighting functions used by the SCO-SLIDAR. These functions are plotted in Fig 3.1 for the four vertical heights used in the SHIMM analysis. This figure shows that the 0 km layer produces no scintillation as there is no optical propagation of distorted wavefronts. In order to gain sensitivity to low-altitude turbulence there are two possible approaches. The first is to include the covariance responses of wavefront sensor slopes as in CO-SLIDAR, and the second is to set the conjugation height of the instrument to below the ground.

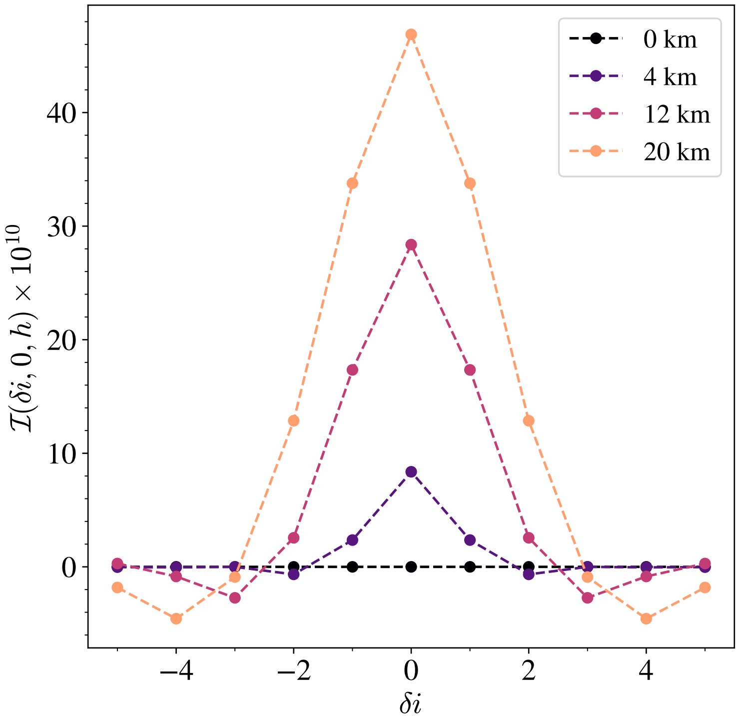

Figure 3.1: A cut-through of the scintillation weighting functions used by the SHIMM inversion.

The latter approach is that taken by instruments such as the generalised SCIDAR, MASS , RINGSS, generalised FASS and Shack-Hartmann MASS (Ogane et al., 2021). This approach has some drawbacks - mostly resulting from aperture diffraction effects, as well as a need to precisely measure the instrument conjugation height (Tokovinin et al., 2003). For these reasons the CO-SLIDAR approach has been favoured.

3.3 Slope weighting functions

For a number of reasons, the slope weighting functions used in SCO-SLIDAR are in their original state not well-suited for usage on small-telescope turbulence monitors with a limited signal-to-noise ratio (SNR). In this case, a SHWFS employing a simple centre of gravity centroid will experience significantly degraded performance, requiring instead a thresholded centre-of-gravity or other similar approach (Thomas et al., 2006). It was observed by Tokovinin (2002a) that a thresholded centroid will more closely measure the Z-tilt of the wavefront rather than the G-tilt, prompting a re-evaluation of the DIMM theoretical centroid variance which is reported in equation 2.33. These same observations are pointed out by Butterley et al. (2006) in the SLODAR theory. It is therefore preferable to develop and calculate weighting functions for the Z-tilt of the wavefronts. To do so, as in Robert et al. (2006) and Védrenne et al. (2010), an expression for the Z-tilt angle-of-arrival is sought. The power spectral density of the Z-tilt is then inverse Fourier transformed in order to find the slope auto-covariances.

Considering equation 2.6 and allowing the Zernike tilt function and aperture function to be at a position $\mathbf{x}$ in the telescope pupil, the function extracting the angle-of-arrival Z-tilt over a Shack-Hartmann sub-aperture is given by

$$s_\zeta(\mathbf{x}) = \phi(\mathbf{x}) * \frac{1}{\lambda z} \sin\left(\frac{\pi|\mathbf{x}|^2}{\lambda z}\right) * W(\mathbf{x}/d) Z_\zeta(\mathbf{x}/d). \tag{3.1}$$

Where $Z_\zeta(\mathbf{x})$ is the Zernike tilt function in the directions $\zeta = \{x, y\}$ and $W(\mathbf{x})$ is the aperture function. As the SHIMM uses square sub-apertures, the approach of Wilson and Jenkins (1996) is followed where an arbitrary basis set (in subaperture units, hence $\mathbf{x}/d$ above) for the Z-tilts is defined which will be normalised in a similar manner to the Zernike polynomials. The tilt functions are given by considering the Zernike x and y tilts across a square aperture of unit subaperture width such that they are described by 2.40. The tip and tilt functions are

$$Z_2(r,\theta) = 2r\cos(\theta), \tag{3.2}$$

$$Z_3(r,\theta) = 2r\sin(\theta). \tag{3.3}$$

Converting to Cartesian coordinates and including a normalising factor a yields

$$Z_2(\mathbf{x}) = 2ax, \tag{3.4}$$

$$Z_3(\mathbf{x}) = 2ay. \tag{3.5}$$

Requiring the the basis set be normalised according to equation 2.20 yields a normalising factor $a = \sqrt{3}$. From hereon, only the x slopes will be considered as the y slopes follow the same derivation. Evaluating the power spectral density of equation 3.1 requires calculating the Fourier transform of the Zernike functions which is given in Noll (1976),

$$F_x(\mathbf{f}') = \int_{-\infty}^{\infty} W(\mathbf{x}')\, Z_2(\mathbf{x}') \exp[-2\pi i \mathbf{f}' \cdot \mathbf{x}'] \mathrm{d}\mathbf{x}'. \tag{3.6}$$

Where $\mathbf{x}' = \mathbf{x}/d$ as the Zernike functions are defined in sub-aperture units. The spatial frequency units are therefore $\mathbf{f}' = d\mathbf{f}$. This integral can be evaluated analytically for a square Shack-Hartmann sub-aperture defined by equation 2.40 and it's solution is given by

$$F_x(\mathbf{f}) = \mathrm{sinc}(\pi d f_y) \left[\frac{i\sqrt{3}\,(\pi d f_x \cos(\pi d f_x) - \sin(\pi d f_x))}{(\pi d f_x)^2} \right]. \tag{3.7}$$

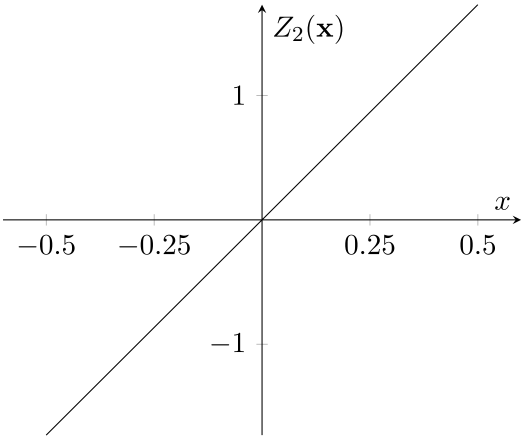

Figure 3.2: $Z_2(\mathbf{x})$ plotted against x for a constant y in an interval of one subaperture unit.

In a similar way $F_y(\mathbf{f})$ is given by swapping f_x and f_y in equation 3.7. The "filter function" to extract the Zernike tilt/tilt covariances in this basis, analogous to those for the unit circle in Sasiela (1994), is given by the square modulus of equation 3.7. This equation is however missing a scale factor; the Zernike tilts have units of radians of phase but a SHWFS measures radians of angle-of-arrival so it is necessary to include a conversion factor. The conversion factor can be obtained by considering the tilt function illustrated in figure 3.2. The angle of arrival is simply the angle made between a line normal to the plane of the tilt function with the Z_2 axis. Through simple geometry this is therefore equivalent to the angle made between the $Z_2(\mathbf{x})$ plane and the x axis.

The angle-of-arrival is typically on the order of arcseconds, therefore the small angle approximation $\tan(\theta) \approx \theta$ may be applied. The Zernike amplitude in radians of phase is converted to an optical path difference in metres through division by the wavenumber $k = 2\pi/\lambda$. At the edge of the subaperture this is $Z_2(1/2)/k = \sqrt{3}/k$. Taking the displacement in x at the sub-aperture edge as $d/2$ and making use of the small angle approximation, the factor converting radians of phase to angle-of-arrival is found to be $\frac{\sqrt{3}}{k} \cdot \frac{2}{d} = \frac{\sqrt{3}\lambda}{\pi d}$. Multiplying equation 3.7 by the scaling factor and taking the modulus squared leads to the filter function

$$\mathcal{Z}_x(\mathbf{f}) = \left(\frac{\sqrt{3}\lambda}{\pi d}\right)^2 \frac{3\,\mathrm{sinc}^2(\pi d f_y)\left[\pi d f_x \cos\left(\pi d f_x\right) - \sin\left(\pi d f_x\right)\right]^2}{(\pi d f_x)^4}. \tag{3.8}$$

The Wiener-Knichin theorem then allows for an expression of the auto-covariance of the angle-of-arrival Z-tilts

$$\mathcal{S}_x(\mathbf{w}, z) = \langle s^x_{ij} s^x_{i'j'} \rangle = \int_{-\infty}^{\infty} \Phi_K(\mathbf{f}) \cos^2\left(\pi z \lambda f^2\right) \mathcal{Z}_x(\mathbf{f}) \exp\left[2\pi i \mathbf{w} \cdot \mathbf{f}\right] \mathrm{d}\mathbf{f}. \tag{3.9}$$

Global tip-tilt subtraction is critical to decouple the measurements of centroids from wind shake and tracking errors. This will therefore significantly modify the agreement of slope covariances with the above theory as the Zernike tip and tilt across the aperture are also subtracted. Similar to SLODAR, the theoretical auto-covariances can be modified. Again considering the slope measurements in two subapertures ij and $i'j'$, we consider using the auto-covariance weighting functions to find the theoretical covariance matrix. Each point in that covariance matrix may be expressed as $C^x_{ab} = \langle s^x_{ij} s^x_{i'j'} \rangle$ where $a, b = \{1, 2 \ldots n\}$ represents a simplified numbering scheme for the sub-apertures and n is the number of active sub-apertures. The tip-tilt subtracted covariances are denoted $\hat{C^x_{ab}}$ and calculated as in Butterley et al. (2006)

$$\hat{C^x_{ab}} = C^x_{ab} - \frac{1}{n}\sum_{a=1}^{n} C^x_{ab} - \frac{1}{n}\sum_{b=1}^{n} C^x_{ab} + \frac{1}{n^2}\sum_{a=1}^{n}\sum_{b=1}^{n} C^x_{ab}. \tag{3.10}$$

The Z-tilt slope weighting functions after tip/tilt subtraction are plotted for the four layer heights used in the SHIMM in figure 3.3. From this figure it is clear that the slope weighting functions are not orthogonal and become more similar in shape for high-altitude turbulence between 12 km and 20 km. Therefore a single-star turbulence profiler utilising only slope information will struggle to reconstruct high altitude layers accurately. This highlights the need to include intensities in the reconstruction.

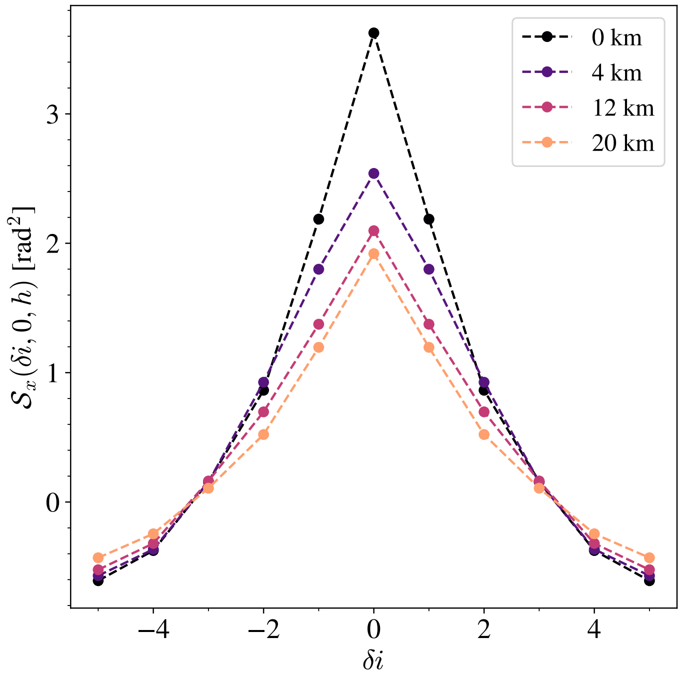

Figure 3.3: A cut-through of the tip/tilt subtracted Z-tilt slope weighting functions used by the SHIMM inversion.

The weighting functions calculated through this new method are compared against SLODAR weighting function generated from code supplied by T. Butterley in Fig 3.4. The SLODAR code calculates slope weighting functions for the x and y directions for a single-star observation (Butterley et al., 2006). The SHIMM weighting functions are calculated for a layer at the ground as the SLODAR does not take into account propagation effects on the power spectrum of the phase. Both the G and Z-tilt cases after tip/tilt subtraction using equation 3.10 are shown.

The Fourier approach has distinct advantages over the SLODAR method of generating auto-covariance response functions detailed in Butterley et al. (2006) which relies on the turbulence structure function. Firstly the computational efficiency of the Fourier transform method is much greater - to generate the SLODAR weighting functions from scratch using the python Numba package took 1.52s whereas numpy FFTs calculate the Z-tilt weighting function in 0.011s. In order to account

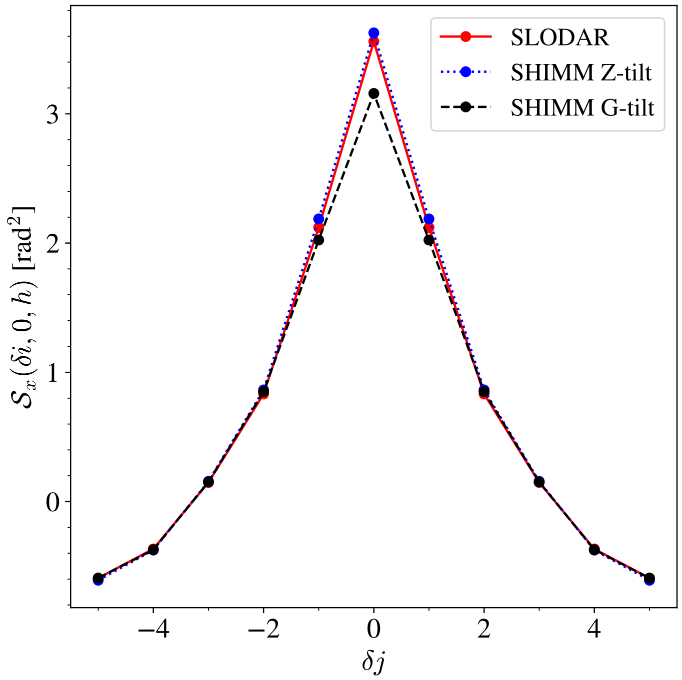

Figure 3.4: A comparison of slope weighting functions for the SHIMM generated by the Fourier G/Z-tilt methods and by the SLODAR method.

for optical propagation effects, Griffiths et al. (2023b) describes how the standard SLODAR approach necessitates firstly a numerical integration of the power spectrum of equation 2.6 according to the relation in Jenkins (1998),

$$D_\phi(r) = 4\pi \int f \Phi_K(f) \left[1 - J_0\left(2\pi f r\right)\right] \mathrm{d}f. \tag{3.11}$$

In the case of Kolmogorov turbulence, this is an improper integral and cannot be evaluated at zero-frequency. The integral is however finite and in the limit of $f \to 0$, $D_\phi(r) \to 0$. We refer to the techniques detailed in Press et al. (2007) for the evaluation of improper integrals with a singularity at zero, specifically the use of the midpoint rule over the trapezoidal rule. One complication is that this function is highly peaked at very small displacements with a long oscillating tail, making accurate numerical integration difficult and computationally expensive. Fig 3.4 shows that the SHIMM Fourier-filter technique agrees well with the results of nu-

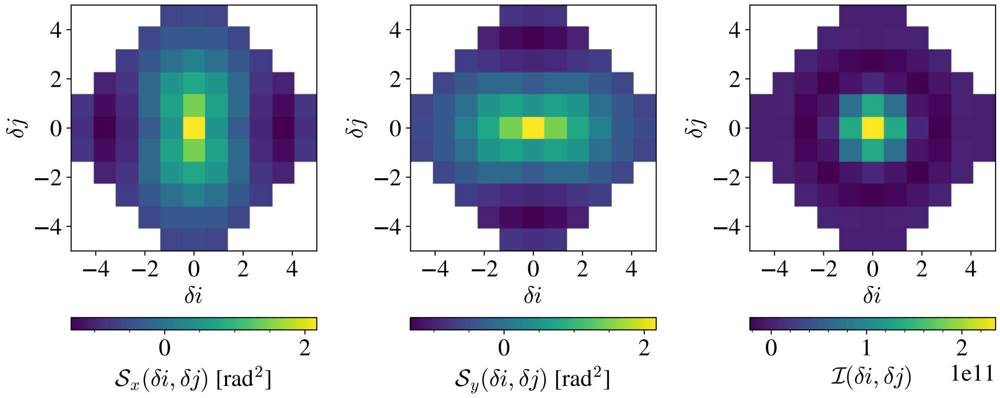

Figure 3.5: SHIMM weighting functions for a turbulent layer at $h = 10$ km plotted against sub-aperture separation on the grid. From left to right are the weighting functions for x, y slopes and scintillation.

merical integration of the SLODAR and the inaccuracy that can arise when using G-tilt filters instead of the Z-tilts derived in this section.

Finally figure 3.5 shows the weighting functions after tip/tilt subtraction plotted against separation on the sub-aperture grid for a single turbulent layer at 10km. It is clear that the y-slope weighting function is the transpose of the x-slope weighting function. The expected centroid variances and scintillation index are found at the $(0, 0)$ coordinate.

3.4 Measurements and bias

The weighting functions defined in the previous two sections are for noiseless measurements. There are several possible sources of noise in the covariances of intensity fluctuations and slope fluctuations from a Shack-Hartmann sensor. In this work it is assumed that the noise within each subaperture is independent.

Starting by considering the scintillation measurements, it is not possible to directly measure ι as given by equation 2.41. Rather, any aperture will measures the normalised fluctuations in the total photometric signal. The fluctuations in the total photometric signal are influenced by contributions form the dark noise, readout noise, shot noise and sky background noise, as well as the scintillation noise (Osborn et al., 2015). Fortunately, only scintillation noise is spatially correlated - the other noise sources are considered independent in each sub-aperture. In order to calculate ι, firstly only the signal from the star must be analysed. Other sources of photons with non-zero mean such as the sky background and dark current are not modulated by the scintillation and so must be subtracted. After background and dark subtraction, the average intensity measured by the SHIMM should be equal to the shot signal from the star, S. The bias due to photometric noise in the scintillation covariance measurements are given by,

$$\langle e_a e_b \rangle_\iota = \begin{cases} \frac{S+n_{\mathrm{pix}}\left(B+D+\sigma_{\mathrm{Rd}}^2\right)}{S^2} & a=b, \\ 0 & a \neq b. \end{cases} \tag{3.12}$$

B, D, σ_{Rd} are the background count, dark current and RMS readout noise per pixel per exposure in photo-electrons and n_{pix} is the number of pixels used to measure the intensity of a Shack-Hartmann focal spot. For the diagonal terms in the covariance matrix where $a=b$, the covariance is equal to the scintillation index with a positive bias that is a function of the detector noise and signal S. For the off-diagonal terms where $a \neq b$, the covariance is equal to the equation 2.47 (which is equivalent to the scintillation index if evaluated at zero separation) and unbiased. By measurement of the individual noise contributions the bias can therefore be subtracted.

Wavefront sensor slope measurements are also affected by noise in the centroiding algorithm. The various sources of centroid noise and analytical expressions are given in Thomas et al. (2006). The brightest pixel centroider is highly performant in strong noise, however there is no analytical model for centroid noise of the algorithm (Basden et al., 2012). The measured slopes may be modelled as the sum of the true wavefront slope and a noise contribution ϵ. Under the assumption that centroid noise is independent in each sub-aperture and normally distributed with zero mean and variance $\langle\epsilon^2\rangle$, the noise in the slope covariance matrix may be calculated. In the absence of tip/tilt subtraction, the centroid noise would be concentrated in the diagonal terms of the covariance matrix. However as discussed in Butterley et al. (2006) the global tip and tilt subtraction couples a small amount of the centroid noise into off-diagonal terms on the covariance matrix. This was derived in Perera (2017) and found to be

$$\langle\epsilon_a\epsilon_b\rangle = \begin{cases} \left(1 - \frac{1}{n}\right)\langle\epsilon^2\rangle & a = b, \\ -\frac{1}{n}\langle\epsilon^2\rangle & a \neq b. \end{cases} \tag{3.13}$$

The diagonal terms in the covariance matrix where $a = b$ are far more strongly biased by centroid noise than the off-diagonal points. Omission of diagonal terms from the inversion therefore suppresses much of the detrimental effects of centroid noise.

3.5 Choice of layers

The chosen layer heights are influenced by a number of factors. One factor is the relationship between speckle size and sub-aperture diameter. The scintillation speckle size is dependent on the propagation distance between the layer and the ground. If the Fresnel zone speckle size is smaller than the sub-aperture diameter then the speckle will be fully averaged in the total intensity measurement from the aperture. Therefore the contribution to the scintillation power spectral density will be lost for spatial frequencies higher than this, and it can be expected that the reconstruction will be insensitive to the scintillation information from that layer. For the sub-aperture diameter of the SHIMM, 4.67 cm, this corresponds to turbulent layer height of approximately 1700 m.

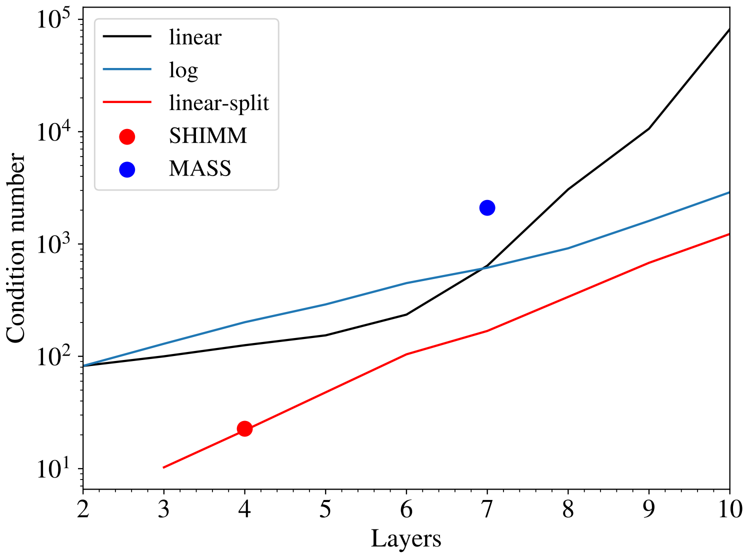

Figure 3.6: Design matrix condition number plotted against the number of layers to fit for a number of different layer selection schemes. The SHIMM layer result is marked on by the red circle.

However, the primary consideration when determining the number and height of the layers is the ill-conditioned of the resulting inverse problem. Ill-conditioning stems from the fact that the weighting functions are not orthogonal with altitude. That is to say that columns in the matrix of weighting functions are similar, or that weighting functions at different heights are similar. This means that the matrix A becomes more singular if an attempt is made to reconstruct too many layers. As the columns of A become too similar, random noise can greatly affect the solution and accuracy is lost. A convenient method of measuring how ill-conditioned a matrix can be is the condition number (Hansen and O'Leary, 1993). It is the ratio of the largest singular value in the singular value decomposition of A to the smallest value. If the problem is ill conditioned, the smallest singular values approach zero and the condition number is large. Figure 3.6 evaluates for the case of the SHIMM optics a number of layer placement schemes using the condition number of the design matrix. Layers are chosen in the interval 0 km to 20 km. The schemes include placing layers on a linear scale of height, a base-2 logarithmic scale of height, a split linear scale with twice as many layers between 0 km and 10 km as between

10 km and 20 km. The condition number of matrices using the SHIMM 4-layer model and the MASS 7-layers are also shown. It is clear from this plot that the linear-split method outperforms all others, and that the MASS layers are not a suitable placement scheme for this system.

3.6 Response functions

The weighting functions are the auto-covariances of slopes and intensities measured in pairs of sub-apertures with given separations for a single, thin layer with a unit $C_n^2(h)\,\mathrm{d}h$ Unlike triangulation techniques such as SLODAR and SCIDAR which spatially separate the responses from layers at different heights, all of the atmospheric layers are overlaid to produce a single measured function. The model is limited to defining a number of thin layers at given heights - inevitably fewer layers than the real atmosphere and certainly not at the correct heights. It is therefore important to characterise the response of the instrument to thin layer at an arbitrary height. A "response function" can by found by calculating the theoretical covariance response for a thin layer at a number of different heights throughout the atmosphere, and putting each of them into the noiseless inverse problem of equation 3.14. The $C_n^2(h)\,\mathrm{d}h$ measured at each fixed layer height in the inversion can then be plotted. The total sum of $C_n^2(h)\,\mathrm{d}h$ in all bins is expected to be equal to the $C_n^2(h)\,\mathrm{d}h$ of the thin layer. Examples of instrument response functions include the MASS and RINGSS which can be found in Kornilov et al. (2003) and Tokovinin (2021). The SHIMM response functions may be found in figure 3.7. In this plot the y-axis represents the $C_n^2(h)\,\mathrm{d}h$ measured in the bins divided by the $C_n^2(h)\,\mathrm{d}h$ of the input layer, therefore the sum of the normalised response at all heights should be equal to one. Figure 3.7 does verify this, and shows that layers below 20 km should be accurately characterised. Above 20 km the $C_n^2(h)\,\mathrm{d}h$ will be over-estimated, providing an important motivation for placing the highest layer at a level above which there will be little turbulence. Previous studies from the

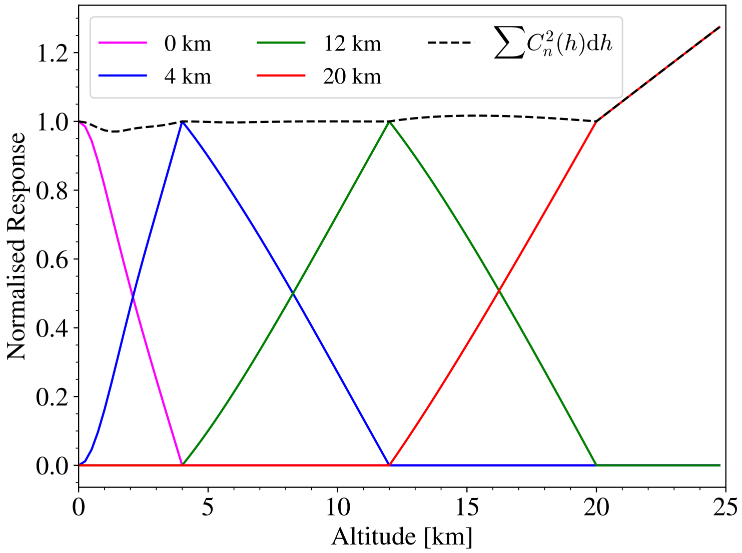

Figure 3.7: SHIMM response functions for the four layers plotted up to 25 km. The black dashed line represents the sum of all layers.

100-layer SCIDAR at Paranal show that there is very little turbulence above this height (Osborn et al., 2018) and so the effect of this systematic overestimation is likely to be small and most obvious in parameters that are sensitive to high-altitude turbulence such as the isoplanatic angle.

3.7 Turbulence profile inversion

For Shack-Hartmann optical turbulence profiling with n fitted layers and m scintillation and slope covariance measurements, the inversion problem is

$$\mathbf{c} = \mathbf{W}\mathbf{j} + \mathbf{e} + \varepsilon. \tag{3.14}$$

The matrix $\mathbf{W}$ is of shape $(m \times n)$ where $m \gg n$, therefore the system of linear equations is considered over-determined. The vector $\mathbf{c}$ is constructed by flattening the three covariance matrices which are of the form $C_{ab}^x = \langle s_a^x s_b^x \rangle$ for the measurements of scintillation , x-axis slopes and y-axis slopes. Example covariance matrices for the three measurements are shown in figure 3.8. Given the noise in intensity measurements $\langle e_\iota^2\rangle$, and a centroid noise $\langle \epsilon^2\rangle$, the vector of measured covariances $\mathbf{c}$ and the vector of biases in the covariances due to measurement error $\mathbf{e}$ can be written as

$$\mathbf{c} = \begin{bmatrix} \langle \iota_1\iota_1\rangle \\ \langle \iota_1\iota_2\rangle \\ \vdots \\ \langle \iota_n\iota_n\rangle \\ \langle s_1^x s_1^x\rangle \\ \langle s_1^x s_2^x\rangle \\ \vdots \\ \langle s_n^x s_n^x\rangle \\ \langle s_1^y s_1^y\rangle \\ \langle s_1^y s_2^y\rangle \\ \vdots \\ \langle s_n^y s_n^y\rangle \end{bmatrix}, \quad \mathbf{e} = \begin{bmatrix} \langle e_\iota^2\rangle \\ 0 \\ \vdots \\ \langle e_\iota^2\rangle \\ \frac{n-1}{n}\langle\epsilon^2\rangle \\ -\frac{1}{n}\langle\epsilon^2\rangle \\ \vdots \\ \frac{n-1}{n}\langle\epsilon^2\rangle \\ -\frac{1}{n}\langle\epsilon^2\rangle \\ -\frac{1}{n}\langle\epsilon^2\rangle \\ \vdots \\ \frac{n-1}{n}\langle\epsilon^2\rangle \end{bmatrix}. \tag{3.15}$$

The weighting function matrix is therefore given by

$$\mathbf{W} = \begin{bmatrix} \mathcal{I}(\mathbf{w}_{11}, z_0) & \mathcal{I}(\mathbf{w}_{11}, z_1) & \dots & \mathcal{I}(\mathbf{w}_{11}, z_n) \\ \mathcal{I}(\mathbf{w}_{nn}, z_0) & \mathcal{I}(\mathbf{w}_{nn}, z_1) & \dots & \mathcal{I}(\mathbf{w}_{nn}, z_n) \\ \vdots & \vdots & \ddots & \vdots \\ \mathcal{S}_x(\mathbf{w}_{11}, z_0) & \mathcal{S}_x(\mathbf{w}_{11}, z_1) & \dots & \mathcal{S}_x(\mathbf{w}_{11}, z_n) \\ \vdots & \vdots & \ddots & \vdots \\ \mathcal{S}_x(\mathbf{w}_{n,n}, z_0) & \mathcal{S}_x(\mathbf{w}_{n,n}, z_1) & \dots & \mathcal{S}_x(\mathbf{w}_{n,n}, z_n) \\ \mathcal{S}_y(\mathbf{w}_{11}, z_0) & \mathcal{S}_y(\mathbf{w}_{11}, z_1) & \dots & \mathcal{S}_y(\mathbf{w}_{11}, z_n) \\ \vdots & \vdots & \ddots & \vdots \\ \mathcal{S}_y(\mathbf{w}_{nn}, z_0) & \mathcal{S}_y(\mathbf{w}_{nn}, z_1) & \dots & \mathcal{S}_y(\mathbf{w}_{nn}, z_n) \end{bmatrix}, \tag{3.16}$$

and the solution $\mathbf{j}$ will be a vector of $C_n^2(h)\,\mathrm{d}h$,

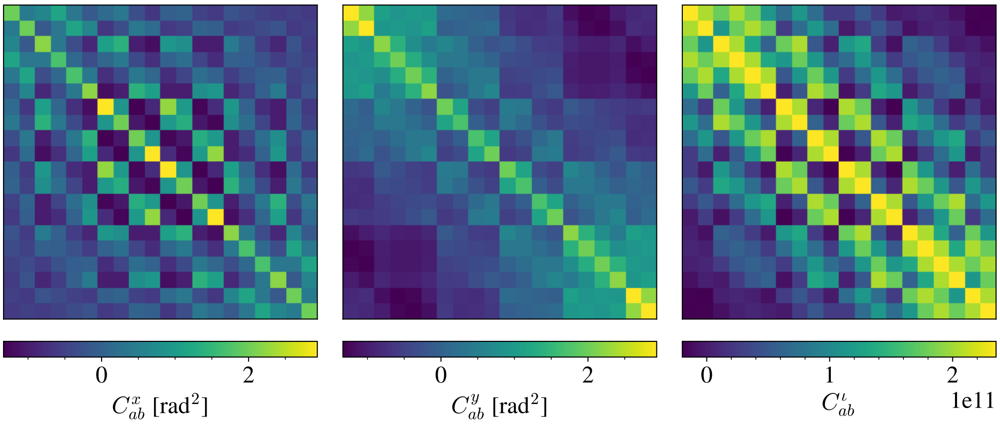

Figure 3.8: Example covariance matrices for the SHIMM. From left to right are the x, y slope covariance matrices, $\mathbf{C}^x_{ab} = \langle s^x_a s^x_b \rangle$, $\mathbf{C}^y_{ab} = \langle s^y_a s^y_b \rangle$, and scintillation covariances $\mathbf{C}^\iota_{ab} = \langle \iota_a \iota_b \rangle$ for all possible pairs of the 20 active subapertures. Each matrix therefore has 400 terms and is diagonally symmetric.

$$\mathbf{j} = \begin{bmatrix} C_n^2(z_0)\,\mathrm{d}z \\ C_n^2(z_1)\,\mathrm{d}z \\ \vdots \\ C_n^2(z_n)\,\mathrm{d}z \end{bmatrix}. \tag{3.17}$$

The vector ϵ is additional convergence noise associated with calculation of the covariances with a limited number of frames, and other random errors that may occur in calculation of the covariances. In this case we assume that the noise is normally distributed with a mean of zero and that noise in each covariance measurement is independent. We can therefore express the covariance matrix of ϵ as a diagonal matrix C_ϵ.

This formulation will retrieve the turbulence profile along the line of sight path of the instrument. Two approaches are obvious in reporting results: either distances to the layers z_n are fixed, or they are allowed to vary in such a way as to conserve the vertical heights of the layer. For the SHIMM the latter method is chosen to produce results that are easier to compare with other instruments. To conserve the vertical heights of the layers, a model is needed to associate the zenith angle of observations, γ, with the vertical heights of each layer h_n and the line-of-sight distances z_n. The line-of-sight turbulent layers are chosen using a set of fixed vertical heights $\mathbf{h} = \{h_0,\, h_1 \ldots h_n\}$ that are transformed under the standard geometric $\sec(\gamma)$ approximation for airmass assuming plane parallel atmospheric layers,

$$\mathbf{j}(z) = \mathbf{j}(h) \sec{(\gamma)}. \tag{3.18}$$

A disadvantage with fixed vertical layers is that at low elevation angles, z can become very large and optical propagation may cause the scintillation to enter into the saturation regime (Young, 1970). This can introduce systematic bias into the results as shown in Beesley et al. (2024) where a direct comparison is made between simultaneous SHIMM measurements at Zenith and a range of elevation angles. In this work, two methods will be tested for solving equation 3.14. The first is by the weighted least squares formulation, or maximum likelihood estimation, described in section 2.7.2. The second is by using Tikhonov regularisation as detailed in section 2.7.3 to reduce the impact of noise in the inverse problem and stabilise the solution. This will be investigated in chapter 4.

3.8 Influence of finite bandpass

The above equations are all only valid under the assumption of monochromatic light. It is known that polychromatic light can affect the power spectrum of amplitude fluctuations and can therefore be considered in the weighting functions (Tokovinin, 2003). However it is argued from investigation into polychromatic effects on the SCIDAR in simulation that the effects on scintillation covariances in such cases are small and are agree well with performing the analysis at the effective wavelength of the instrument (Shepherd et al., 2014). One might assume that the slopes are insensitive to wavelength as changing the wavelength only affects the optical path length experienced by the light. However, taking into account the wavelength dependence of the Fresnel filter in equation 2.6 one must conclude that

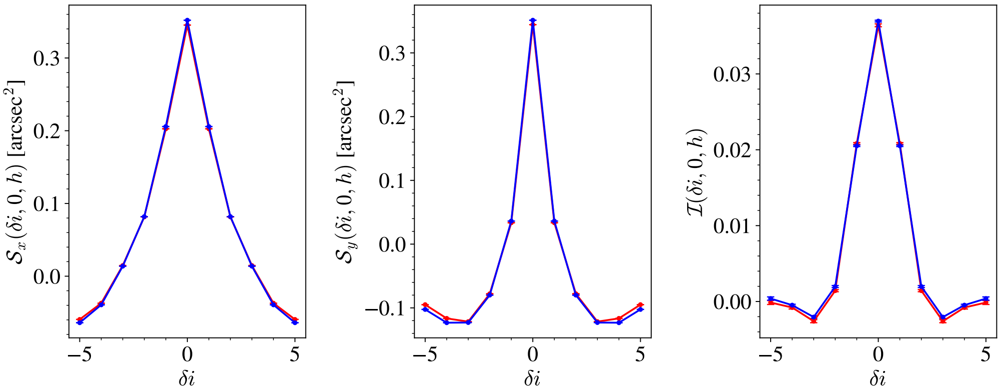

Figure 3.9: Simulated auto-covariance responses to the HV profile for a single wavelength simulation at 1280n (blue) and a panchromatic (red) simulation consisting of five wavelengths weighted by a rectangular function in the interval 900nm to 1660nm. These functions result from a vertical cut through the centre of the auto-covariance maps as in figure 3.5.

the modulation as a result of optical propagation will depend on optical bandpass in a non-trivial way.

Figure 3.9 presents a comparison of noiseless measurements from simulations using the Hufnagel-Valley (HV) profile with a rectangular transmission function across the wavelength range of 900 nm - 1660 nm. The effective wavelength of this transmission function is 1280 nm and matches the monochromatic simulation wavelength exactly. The polychromatic simulation is achieved by summing the Shack-Hartmann images from ten monochromatic simulations with equal intensity weighting sampled evenly across the rectangular transmission function. The figure shows that there is little appreciable difference between the two results. This justifies the use of monochromatic simulations and analysis at the effective wavelength of the system as an approximation.

3.9 Influence of finite exposure

The SHIMM weighting functions are only valid for perfectly “frozen” turbulence, that is an assumption of zero exposure time. In reality, the wavefront sensor exposes for a finite time and averages the optical turbulence (OT) fluctuations within the exposure. Under the Taylor's frozen flow assumption, for a layer moving with a wind speed v in a direction θ_w and an exposure time τ_E the wind speed filter may be derived as in Kornilov and Safonov (2011). Both weighting functions are modified by a convolution with a rectangular function representing the spatial averaging effect as wind blows across the aperture in the two spatial directions. Taking a quantity $g_0(\mathbf{x})$ that can represent $s_\zeta(\mathbf{x})$ or $\iota(\mathbf{x})$, and $g(\mathbf{x})$ to be the quantity modified by the wind speed integral

$$g(\mathbf{x}) = \int_{-\frac{v\tau_E}{2}}^{\frac{v\tau_E}{2}} g_0(\mathbf{x}-\mathbf{x}')\mathrm{d}\mathbf{x}', \tag{3.19}$$

$$g(\mathbf{x}) = \int_{-\infty}^{\infty} g_0(\mathbf{x}-\mathbf{x}')h(\mathbf{x}')\mathrm{d}\mathbf{x}' = g_0(\mathbf{x}) * h(\mathbf{x}), \tag{3.20}$$

where the $h(\mathbf{x})$ represents a rectangle over which the turbulent phase traces a path during an exposure. It is represented by a 2D-rect function with dimensions set by the wind speed, direction and exposure time,

$$h(x,y) = \frac{2}{v^2\tau_E^2\sin(2\theta_w)}\,\mathrm{rect}\left(\frac{x}{v\cos(\theta_w)\tau_E}\right)\mathrm{rect}\left(\frac{y}{v\sin(\theta_w)\tau_E}\right). \tag{3.21}$$

The Fourier filter is then obtained in the standard way by calculation of the modulus squared of the Fourier transform of $h(x,y)$, $\mathcal{H}(\mathbf{f},\mathbf{v},\tau_E) = |\mathcal{F}[h(\mathbf{x},\mathbf{v},\tau_E)](\mathbf{f})|^2$ which yields the finite exposure weighting functions,

$$\mathcal{H}(\mathbf{f},\mathbf{v},\tau_E) = \mathrm{sinc}^2(\pi v\cos(\theta_w)\tau_E f_x)\,\mathrm{sinc}^2(\pi v\sin(\theta_w)\tau_E f_y). \tag{3.22}$$

This wind speed filter function can be included in the inverse Fourier transform that generates the weighting functions 3.9 and 2.45 to include the effects of wind speed and non-zero exposure time. The influence of the exposure time and wind speed of the layer are explored in Fig 3.10 and Fig 3.11.

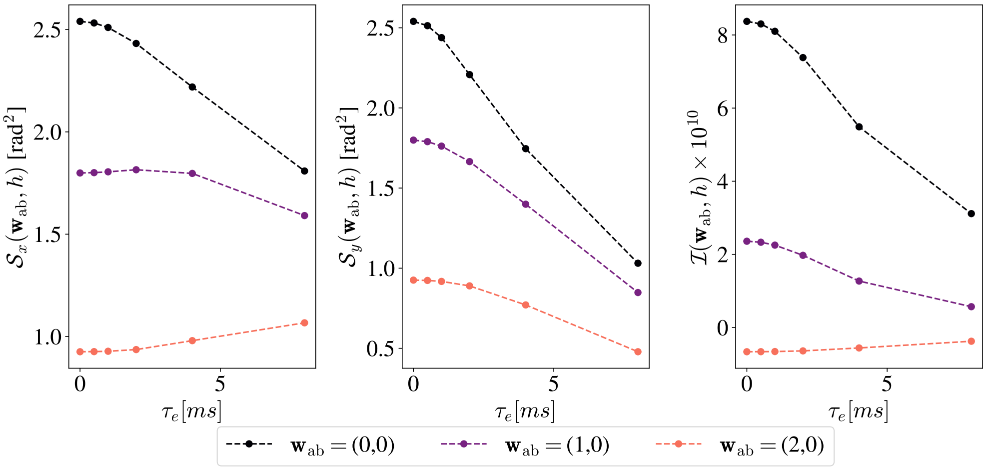

Figure 3.10: Effect of changing exposure time on three spatial separations, $\mathbf{w}_{\rm ab}$, in the weighting functions of slopes and scintillation for a single layer at 4000 m and a fixed wind speed of 10 m s^{-1} along the y-axis.

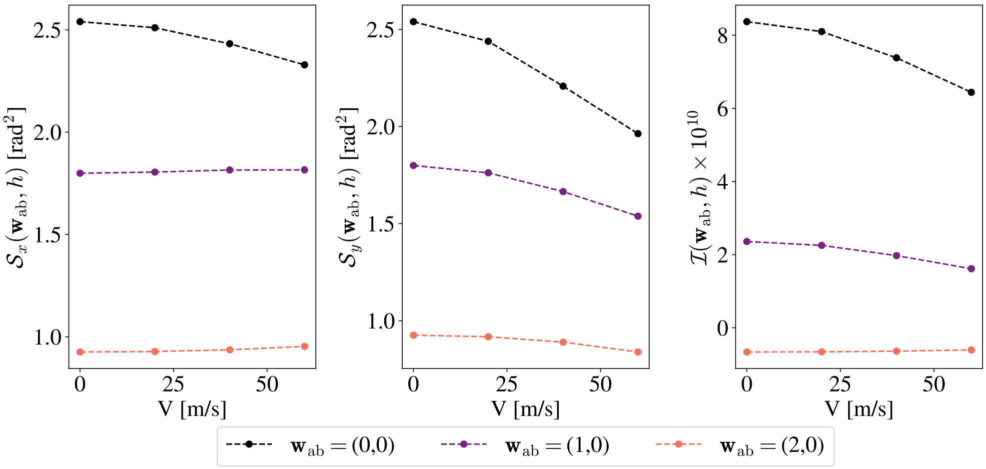

Figure 3.11: Effect of wind speed in the y-direction on three spatial separations, $\mathbf{w}_{\rm ab}$, in the weighting functions of slopes and scintillation for a single layer at 4000 m and a fixed exposure time of 1 ms.

Following the example of Kornilov and Safonov (2011), it is possible to perform a Taylor expansion of equation 3.22 around zero for small values of the $\pi v\cos(\theta_w)\tau_E$ and $\pi v\sin(\theta_w)\tau_E$. Replacing these coefficients with a single constant for $i=\{x,y\}$: l_x, l_y, the 2D-Taylor expansion may be expressed as

$$\mathcal{H}(l_x,l_y,f_x,f_y)=1-\frac{2}{3}(l_x^2f_x^2+l_y^2f_y^2)+\mathcal{O}(l_x^3,l_y^3,f_x^3,f_y^3). \tag{3.23}$$

Substitution into the power spectrum equations for the slopes and intensities, and re-defining the constants $l_x=\tau_E\pi v\cos(\theta_w)$ to bring exposure time out explicitly yields for the slope weighting functions,

$$\begin{aligned}\mathcal{S}'_x(\mathbf{w},z,\tau_E)&=\mathcal{S}_x(\mathbf{w},z,0)-\\&\frac{2}{3}\tau_E^2\left[l_x^2\int_{-\infty}^{\infty}f_x^2\Phi(\mathbf{f})\sin^2(\pi z\lambda f^2)\mathcal{Z}_x(\mathbf{f})\exp(2\pi i\mathbf{x}\cdot\mathbf{f})\right.\\&\qquad\left.-\,l_y^2\int_{-\infty}^{\infty}f_y^2\Phi(\mathbf{f})\sin^2(\pi z\lambda f^2)\mathcal{Z}_x(\mathbf{f})\exp(2\pi i\mathbf{x}\cdot\mathbf{f})\right],\end{aligned} \tag{3.24}$$

$$\mathcal{S}'_x(\mathbf{w},z,\tau_E)=\mathcal{S}_x(\mathbf{w},z,0)-\frac{2}{3}\tau_E^2\Theta(\mathbf{x}). \tag{3.25}$$

Finally by taking simultaneous covariances at two exposure times τ_E and $2\tau_E$ one can solve for the zero-exposure time weighting functions through a simple equation and arrive at the result given for the scintillation index correction in Kornilov and Safonov (2011),

$$\mathcal{S}'_x(\mathbf{w},z,\tau_E)=\mathcal{S}_x(\mathbf{w},z,0)-\frac{2}{3}\tau_E^2\Theta(\mathbf{x}), \tag{3.26}$$

$$\mathcal{S}'_x(\mathbf{w},z,2\tau_E)=\mathcal{S}_x(\mathbf{w},z,0)-\frac{8}{3}\tau_E^2\Theta(\mathbf{x}), \tag{3.27}$$

$$\mathcal{S}_x(\mathbf{w},z,0)=\frac{4}{3}\mathcal{S}'_x(\mathbf{w},z,\tau_E)-\frac{1}{3}\mathcal{S}'_x(\mathbf{w},z,2\tau_E). \tag{3.28}$$

The exact same method can be applied to the scintillation weighting functions.

3.10 Dome and tube seeing

In all of the analysis so far it has been assumed that the optical turbulence measured by the wavefront sensor (WFS) has a Kolmogorov or Von Kármán power spectrum. These assumptions hold well for optical turbulence in the free atmosphere. However the local environment around the telescope can also have a major effect on the measurements. A telescope dome structure can interact thermally with air, or retain hot air from heat sources within - for example cameras and computers - which would otherwise be cleared away by wind. This can lead to relatively slow-moving turbulence within the dome, known as “dome seeing” (Woolf, 1979). Several optical techniques have been developed to measure the strength of dome seeing (Osborn and Alaluf, 2023; Bustos and Tokovinin, 2018; Lai et al., 2019). Such instruments unlock the ability to make changes to dome design and observe quantitative improvement in the seeing inside the domes of large telescopes. This kind of turbulence is however a nuisance for traditional turbulence monitoring instruments which rely on assumptions about the phase power spectrum. Dome seeing is inherently non-Kolmogorov (Bustos and Tokovinin, 2018) and so will reduce the profiling accuracy of the inversion which assumes a Kolmogorov or Von Kármán spectrum. A further issue for instrumentation utilising a closed-tube optical tube assembly (OTA) is so called "tube seeing". Tube seeing is similar, slow-moving and non-Kolmogorov turbulence caused by air mixing inside the OTA itself, most likely caused by heating of the walls of the OTA. It is possible to minimise tube seeing and dome seeing by physically altering equipment and the local environment, however this is not always practical. Ideally therefore, the dome seeing component might be isolated and removed in post-processing. The key is exploiting the fact that dome seeing moves slowly compared to atmospheric optical turbulence, and can therefore be extracted by considering temporal correlation of slopes at longer timescales (Shepherd et al., 2014).

3.10.1 Temporal auto-covariance

Under Taylor's frozen flow hypothesis, the turbulence phase pattern does not evolve and moves with a velocity vector $\mathbf{V}$ across the telescope aperture. After a time τ the layer has moved a distance $\mathbf{V}\tau$. This setup is similar to derivation of the Fourier filter wind speed and finite exposure time equation 3.22. To find the temporal auto-covariance, the SLODAR auto-covariance can be modified to include a time lag τ

$$A_x(\delta i, \delta j, \tau) = \left\langle \sum_{i,j} s^x_{i,j}(t) s^x_{i+\delta i, j+\delta j}(t+\tau) / O(\delta i, \delta j) \right\rangle . \tag{3.29}$$

In reality, the time lags that can be computed from WFS data are discrete with a granularity $\delta\tau$, the inverse of the camera frame rate. Since the phase is a homogeneous, random field, the spatio-temporal auto-covariance function for a given time lag is a simple spatial translation of the auto-covariance at $\tau = 0$ by $\mathbf{V}\tau$ (Tatarski, 1971). The temporal auto-covariance response for a single layer is therefore expected to manifest as a peak that moves across $V\delta\tau/d$ sub-apertures per time lag. These moving covariance peaks will also be present for the intensity auto-covariances. This has been exploited to measure the wind speeds and directions of individual turbulent layer by a number of turbulence monitoring instruments including SCIDAR and SLODAR and on open loop data from adaptive optics systems (Guesalaga et al., 2014). For time lags $\tau > D/V$ where D is the telescope pupil diameter, the auto-covariance function measured for $\tau = 0$ has completely passed out of the map. For sufficiently large τ, the effective spatial baseline increases and the correlation between the two slope measurements decreases to zero as in figure 3.13. As the decorrelation time is proportional to the wind speed of the layer, optical turbulence arising from atmospheric layers decorrelates relatively quickly - the auto-covariance peak will take $D/2V$ seconds to exit the auto-covariance map, which for a ground level wind speed of $1\,\mathrm{m\,s^{-1}}$ is $0.1397\,\mathrm{s}$ for an 11-inch aperture. Dome seeing has been observed to remain correlated on much longer time scales than atmospheric turbulence (Shepherd et al., 2014), owing to far slower wind speeds inside a dome. It is therefore possible to isolate the auto-covariance response arising from dome turbulence by calculating the spatio-temporal auto-covariance of the slopes for large time lags.

3.10.2 Subtraction method

The spatio-temporal auto-covariance is calculated for all subaperture baselines using equation 3.29. A maximum time lag is chosen at which atmospheric layers will be decorrelated. For the SHIMM, a maximum temporal lag of $\tau_{\text{max}} = 2\,\text{s}$ ensures that the auto-covariance peaks from any slow-moving layers with a wind speeds of less than $V = 0.069\,85\,\text{m}\,\text{s}^{-1}$ would remain inside the auto-covariance map for all offsets. A plot of on-sky measurements of the spatio-temporal auto-covariance at three different time lags is shown in figure 3.12. The x and y auto-covariances have been added together to produce symmetric response functions that are easier to visualise. The figure shows atmospheric turbulence decorrelating between the auto-covariance ($\tau = 0\,\text{m}\,\text{s}^{-1}$) and $\tau = 15\,\text{ms}$ while a sharply-peaked dome seeing component remains stationary in the central pixel for the longest time lag $\tau = 83.3\,\text{ms}$. Simply allowing the atmospheric layers to decorrelate and subtracting the remaining auto-covariance at a large time lag is insufficient to correct for this as the dome turbulence peak also evolves slowly with time. Previous studies have advocated for a linear fit to the decay curve for the dome seeing component (Guesalaga et al., 2014). However in this study it was found that this approximation does not hold for all sub-apertures. The approach in this work is a variation on the linear extrapolation. The method involves the following steps:

1. Calculate the spatio-temporal covariances and auto-covariances for all valid subaperture pairs for a maximum time lag τ_{max}.
2. Identify the time lag where the peaks of auto-covariance responses for all atmospheric turbulent layers have just left the auto-covariance map, double

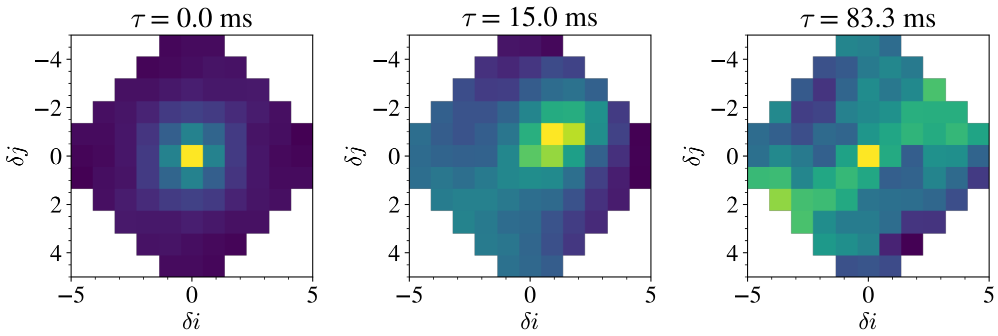

Figure 3.12: Sum of on-sky x and y spatio-temporal auto-covariances plotted for three different time lags showing the evolution of atmospheric layers and the almost-stationary dome seeing component.

this time to find the start point.

3. Disregard all points before the start point, perform a order-2 polynomial fit to the covariance decay curve for each sub-aperture pair.
4. Use the polynomial fits to extrapolate the dome seeing covariance matrix to $\tau = 0\,\mathrm{s}$.
5. Calculate the dome-seeing auto-covariance map using equation 2.37. This effectively averages the dome seeing extrapolation if there are multiple baseline pairs with the same separation, producing a symmetric and smoothed contribution.
6. Re-calculate a covariance matrix from the dome seeing auto-covariance and subtract this from the measured slope covariance matrices for a time lag of $\tau = 0\,\mathrm{s}$.

The first key point of discussion is how to find the starting point described in step 2. An assumption is made that the strongest auto-covariance response originates from the ground layer turbulence, which is the slowest moving layer and dominates over other layers such that they are not detectable. The sum of the auto-covariances in

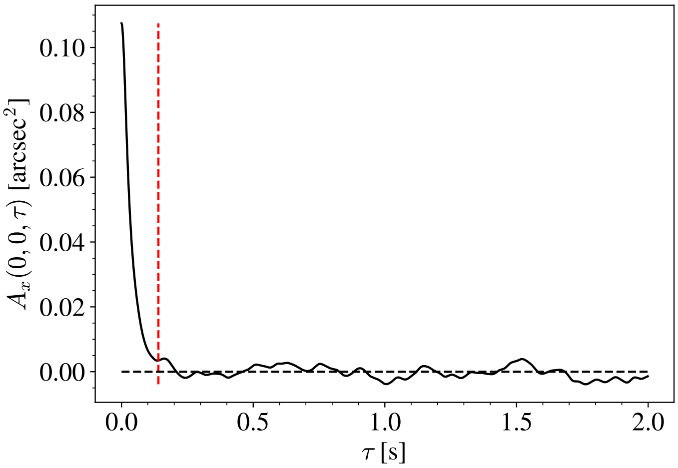

Figure 3.13: Spatio-temporal auto-covariance for the point $(0, 0)$, i.e. the centroid variances, for a noiseless simulation of a single turbulent layer moving with a wind speed of $2\,\mathrm{m\,s^{-1}}$ for the 28 cm SHIMM. The red dashed line represents the time lag $\tau = D/V$ which is detected by the start-time algorithm.

the points at the edge of the covariance map is monitored for each time lag which increases as the peak translates outward from the centre. The point at which the auto-covariance first decreases is assumed to be the time lag at which the peak has moved out of the map, i.e. $\tau = D/2V$. It was hypothesised that after the entire auto-covariance peak has translated out of the map, that the atmospheric turbulent layer could be effectively considered fully decorrelated. Figure 3.13 provides evidence supporting this. It shows the initial rapid drop in the covariance measured in the central pixel of the auto-covariance map as the atmospheric layer decorrelates, followed by noise. The red dashed vertical line corresponds to the start time of the algorithm $\tau_s = D/V$, and appears to be within the noise level. The time taken for the response from a layer to decorrelate to within the noise level is proportional to the width of the response, which depends on the propagation distance to the ground. The results of an order-2 polynomial fitting to the auto-correlation after the atmospheric decorrelation threshold can be found in figure 3.14. This figure evidences favouring a higher order fit than linear to the decay curve to allow an estimate of the dome seeing component of the auto-covariance for each baseline separation $(\delta i, \delta j)$.

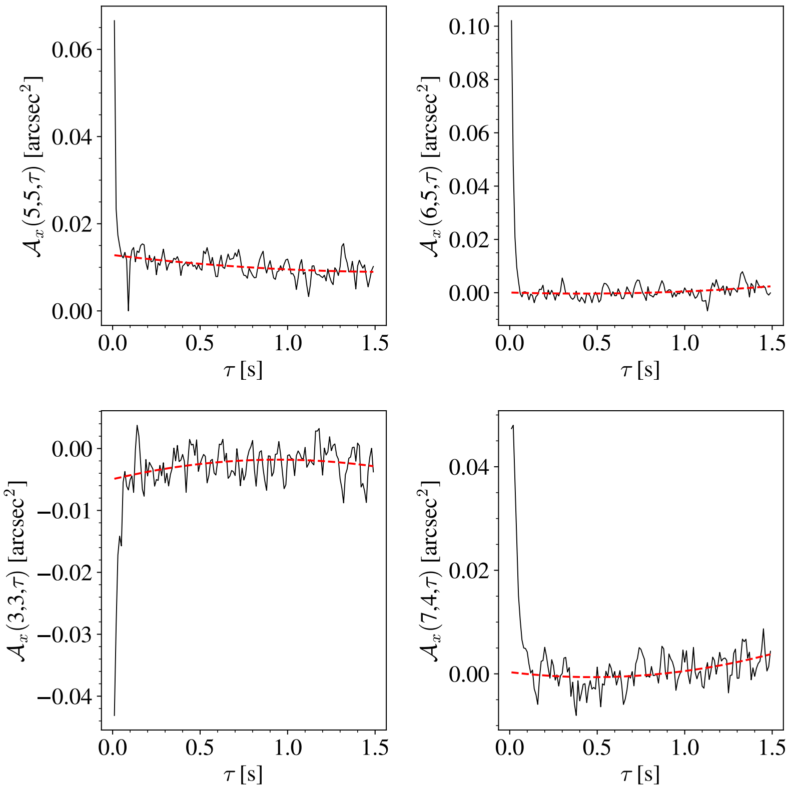

Figure 3.14: Evolution of points in the spatio-temporal auto-covariance map with time lag for real measurements from the TURBO experiment in Barcelona. The red dashed line is the second-order polynomial fitting of the dome turbulence decay curve.

3.11 Coherence time

An atmospheric turbulence parameter that cannot be measured solely from the vertical profile of $C_n^2(h)\,\mathrm{d}h$ is the coherence time. As in equation 2.54, the vertical wind speed profile $V(h)$ is also required. This work implements the FAst DEfocus (FADE) (Tokovinin et al., 2008) method of measuring the coherence time from fast variations in the defocus component of the optical turbulence. Fortunately for a Shack-Hartmann system, obtaining the Zernike defocus is straightforward through the methods described in section 2.4. In this work, the AOtools package (Townson et al., 2019) is used to find the gamma matrices and build the inverse matrix $G^{\dagger}$. This gives direct measurement of the defocus coefficient $a_4(t)$ as a function of time.

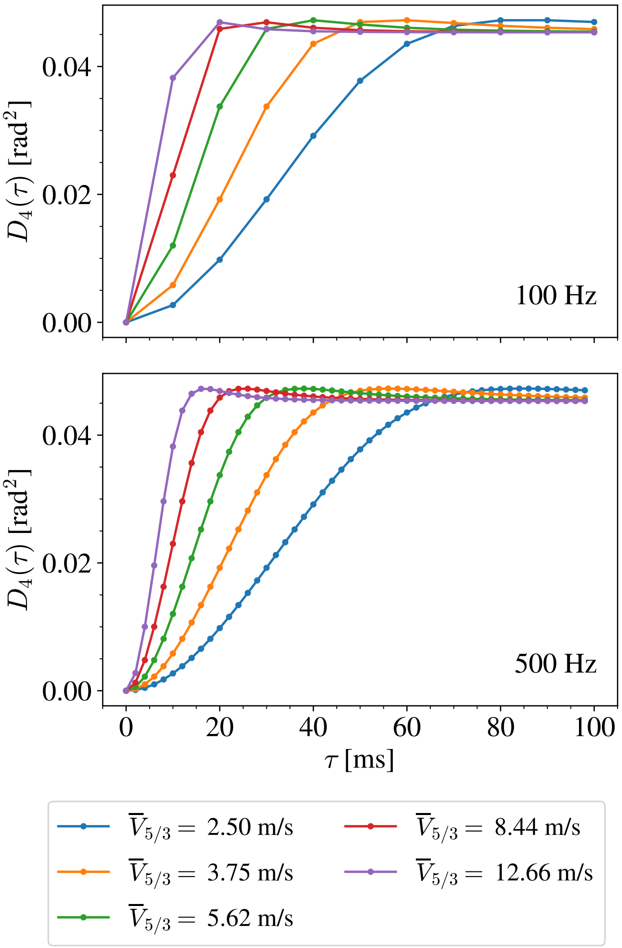

Figure 3.15: Theoretical $D_4(\tau)$ response for sampling rates of 100 Hz (top) and 500 Hz (bottom) for wind speed profiles with increasing effective wind speeds. $C_n^2(h)\,\mathrm{d}h$ remains constant.

Calculation of the structure function of $a_4(t)$ yields a curve that rises rapidly and saturates after a few tens of milliseconds. It is imperative therefore to use high sampling rates of a few hundred Hz in order to sample of the rising part of the curve. This is because the steepness is related to the effective wind velocity $\overline{V}_{5/3}$, while the height of the saturation level is influenced by the integral of $C_n^2(h)\,\mathrm{d}h$. Figure 3.15 shows the theoretical response curves at two different sampling frequencies for a range of $\overline{V}_{5/3}$ and constant profile of $C_n^2(h)\,\mathrm{d}h$. At 100 Hz the rising part of $D_4(\tau)$ is poorly sampled for higher effective wind speeds, illustrating the requirement of fast frame rates. The constant $C_n^2(h)\,\mathrm{d}h$ leads to a similar saturation level of the

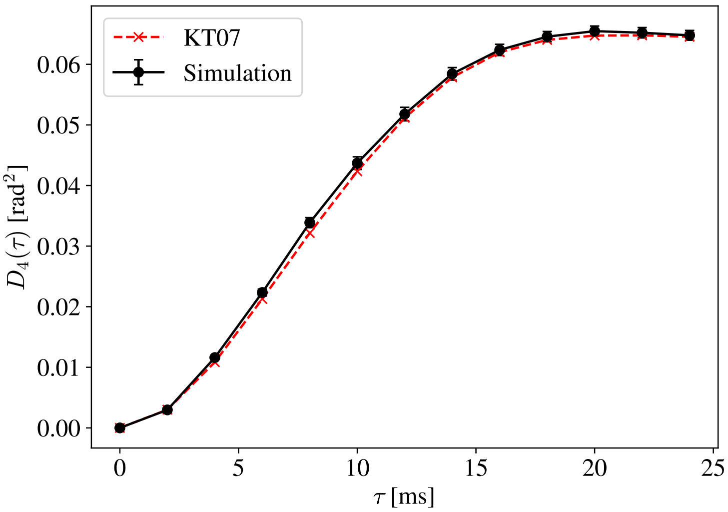

Figure 3.16: The structure function of defocus calculated from simulation of two layers with wind speeds of $10\,\mathrm{m\,s^{-1}}$ and $20\,\mathrm{m\,s^{-1}}$ (black line) at the ground and 10 km respectively, compared with the theoretical function from Kellerer and Tokovinin (2007) (red dashed line).

structure functions across all effective wind velocities.

The theoretical $D_4(\tau)$ is given by Kellerer and Tokovinin (2007) as

$$D_4(\tau) = 0.861 k^2 D^{5/3} \int_0^\infty C_n^2(h) K_4(2\tau V(h)/D) \mathrm{d}h. \tag{3.30}$$

Given that the $C_n^2(h)\ \mathrm{d}h$ profile is obtained from the inversion method, equation 3.30 can be reduced to a function of the wind speed profile $V(h)$. The Kellerer and Tokovinin (2007) simplification of K_4 for the case of circular Zernike polynomials is further applied and this combination allows for a simple non-linear least squares solver to find the best fitting $V(h)$. Furthermore, the uncertainty in the defocus measurements σ_4^2 can be found using the analytical least squares error in equation 2.63. Uncertainty in the defocus leads to a bias in the structure function of size $2\sigma_4^2$ which must be subtracted.

To validate the forward model, a Monte-Carlo simulation with shot noise only was made consisting of two screens with wind speeds of $10\,\mathrm{m\,s^{-1}}$ and $20\,\mathrm{m\,s^{-1}}$ at altitudes of 0 km and 10 km respectively. In figure 3.16 the structure function of defocus has been calculated and compared with the theoretical value given by Kellerer and Tokovinin (2007), showing very strong agreement after subtraction of the offset due to noise. The τ_0 for this simulation was 2.4 ms and sampling rate was 500 Hz.

3.12 Outer scale fitting

In this chapter so far, the power spectrum of the optical turbulence has been assumed to be Kolmogorov, as shown in equation 2.11. The observed range of wavefront coherence outer scales of 1 m to 100 m (Ziad, 2016) suggests that sub-aperture baselines on a small telescope are likely to be much smaller than $\mathcal{L}_0$. The influence of outer scale is therefore expected to be small. The sensitivity of Shack-Hartmann measurements of slopes and intensities to outer scale effects is investigated in figure 3.17. The fractional difference between the scintillation index and centroid variance for Kolmogorov and Von Kármán turbulence has been plotted as a function of the outer scale for three different telescope diameters using the HV profile. To maintain the same sub-aperture size, the number of sub-apertures across the pupil was increased. This figure shows that on the small telescope, the outer scale effects on the slopes are negligible. They are most prevalent in the centroid variance on larger telescopes.

The wavefront coherence outer scale may therefore be estimated through an algorithmic minimisation, by assuming that the best fit to the data should arise from a correctly chosen outer scale. There are however many potential pitfalls in such a method as for example the minimisation algorithm may converge on a local minimum rather than a global one, and computation using a global minimisation algorithm is prohibitively time-consuming. The process may also fit to the convergence noise, especially if the true outer scale is large and its effects are therefore relatively weak. As this work focuses on small-telescope results, it is assumed that the outer scale effects are likely to be too small to be measured accurately.

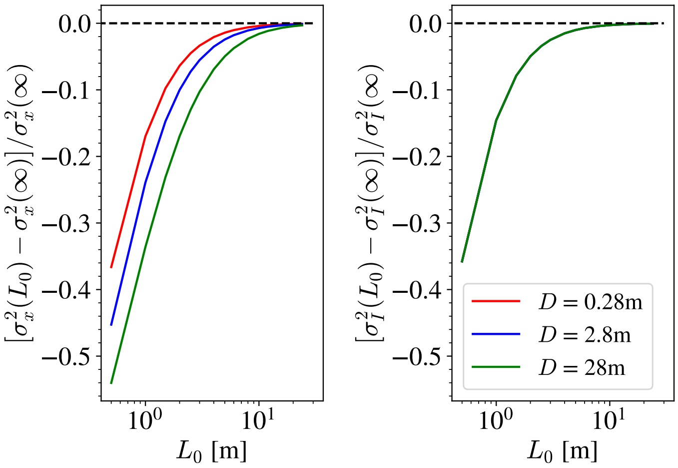

Figure 3.17: Normalised difference between the centroid variance (left) and scintillation index (right) responses for Von Kármán and Kolmogorov turbulence as a function of outer scale. The input profile is a seven equivalent layers binning of the HV profile. The curves on the right hand plot are overlapping.

3.13 Conclusion

This chapter sets out the theory underpinning the analysis of SHWFS data from the SHIMM. A number of modifications have been made to the CO-SLIDAR theory, primarily in the derivation of a new Z-tilt weighting function for SHWFS slope measurements. This was found to be more suitable for use on a small telescope with noisy slope measurements. Several other improvements and mitigations were made to the profiling algorithm. The effect of polychromatic light was evaluated and it was determined that a wide optical bandpass produced no significant changes in the weighting functions. The finite exposure time however may have a significant effect on the weighting functions of slopes and intensities, particularly from strong winds in the upper atmosphere. A method of accounting for this was applied by following a similar analysis to the MASS instrument. Finally, a dome seeing subtraction method using a 2D polynomial fit to the temporal auto-covariance of slope measurements was laid out. The effects of outer scale on accuracy of the Kolmogorov model were further investigated showing that profile reconstruction on small telescopes is likely to be insensitive to outer scales above 5 m.

Chapter 4

Simulations and image analysis

4.1 Introduction

In developing optical turbulence monitoring instrumentation, there is no access to “truth” measurements on-sky. Additionally as discussed in section 6, there are a wide range of environmental factors and assumptions built into different techniques that can affect correlation of data when comparing two instruments. Due to this, such instruments are heavily reliant on simulation to verify analysis techniques. There are a number of parameters affecting the instrument performance that can only be evaluated by simulation, namely the minimum permissible SNR in a sub-aperture, the influence of sub-aperture size and number, telescope diameter, number of pixels to use in centroiding and so on. This chapter discusses the SHIMM simulations that were carried out to verify elements of the analysis in chapter 3 and to characterise the instrument response when the above factors are varied, evaluating the performance of different designs.

4.2 SHIMM simulation design

SHIMM simulations were based on Monte Carlo techniques implemented in the AOTools python package (Townson et al., 2019). Two main approaches were used in designing simulations for the SHIMM. The first was the so-called “independent phase screens" method whereby many phase screens were generated randomly and independently and compiled to an array of wavefronts. The second approach utilised the method of infinite phase screens (Assémat et al., 2006) to simulate a more realistic turbulent layer which moved a distance set by the wind speed between capturing wavefront images. The advantages to the former were a more rapid statistical convergence of parameters and faster simulation, whereas the latter could be used to study and validate temporal techniques. For example in the case of the moving phase screen, several sequential images of the wavefronts could be summed together to simulate an effective exposure time, this however greatly increased the necessary pixel scale and required number of phase screen evaluations. Such details were prohibitively time consuming and so were omitted from larger simulations.

Many layers could be included in the simulations, firstly by defining a discrete number of layers with given turbulence strengths and heights. Profiles were generally taken either from the HV model, or from the Paranal Stereo-SCIDAR database (Osborn et al., 2018) with the latter being favoured as more realistic. These profiles were then reduced from a 100 layer profile to a far smaller number suitable for Monte Carlo simulations using the method of equivalent layers (Fusco et al., 1999). This reduced computing time while maintaining similar atmospheric turbulence statistics. Given a number of randomly generated phase screens at several heights, the angular spectrum method was used to propagate a plane wave through each layer and to the telescope pupil in the simulation. At the pupil, the phase screen could then be sliced into sub-apertures and the telescope pupil mask applied. Shack-Hartmann spots were computed through 2D Fourier transform of the sub-aperture images and padding was set appropriately to maintain the angular image scale of the system. An example of the phase and intensity of a propagated wavefront in the simulated telescope pupil, along with the corresponding spot pattern on the simulated Shack-Hartmann is shown in figure 4.1.

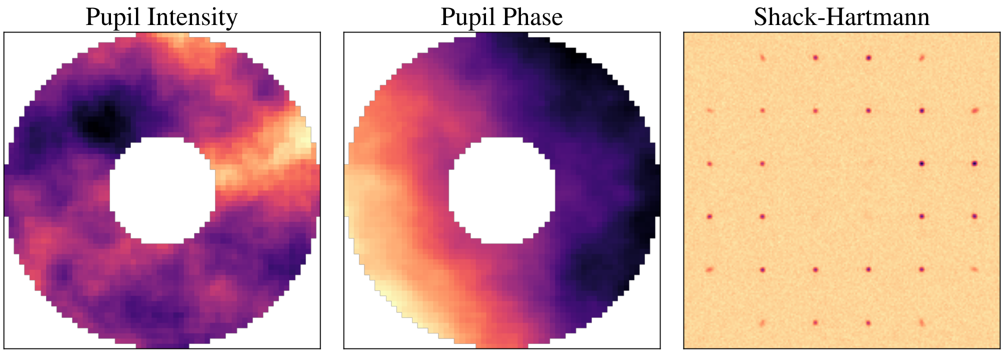

Figure 4.1: Outputs of the SHIMM simulation software from left to right: intensity of the wavefront at the telescope pupil after propagation, phase angle of the wavefront at the telescope pupil and the corresponding Shack-Hartmann image for the SHIMM geometry of 6×6 sub-apertures. The phase screen resolution is 10 pixels per sub-aperture for a pupil diameter of 28 cm.

4.3 Image processing

Image processing techniques are critical to extract accurate measurements of slopes and intensities from Shack-Hartmann images, especially in a low-SNR environment. The raw measurements from the SHIMM camera are still expected to contain significant background, dark and readout noise due to limitations in indium gallium arsenide (InGaAs) technology and some measurements taking place during the daytime. Therefore noise statistics were estimated, Poisson shot noise was added to the spots, Poisson background count to the background and a Gaussian readout noise to the resulting image. The simulations assume a dark subtraction, and include the effect of dark noise in the readout noise by adding the two in quadrature. The estimates of the dark and RMS readout noise from the camera are made from the relevant sections of Gach et al. (2020) for an exposure time of 1.66ms with final values of $640e^{-}$ and $37e^{-}$ found respectively. This gave a total RMS noise of $45e^{-}$. The estimate of the background noise was taken from the 90th percentile of background measurements made on-sky during the TURBulence mOnitoring and forecasting (TURBO) campaign. This high percentile was used to both to give a pessimistic estimate of the daytime sky background as a limit for simulations. This gave a final value of approximately $752e^-$ per pixel per exposure. A 9×9 grid of pixels around the spot was used to measure intensities, giving a value of $n_{\text{pix}} = 81$.

4.3.1 Background subtraction

Background subtraction was achieved through a number of steps in the processing algorithm. Ideally, a background image could be easily captured by moving a telescope off-target such that the star is no longer in the field-of-view. For the SHIMM this was not feasible during sunrise and sunset periods where the background changes rapidly. Therefore a method of in-place background subtraction was implemented which involved masking the spot with the average background value. The following method refers to the process of subtracting the background from a sequence of images of a single Shack-Hartmann sub-aperture.

- Take a difference image of the first and last frames in the dataset and calculate the centroid. This will given an estimate of the initial position of the spot in the image sequence unbiased by static artefacts formed by background images. Slice out a sub-window around this point.
- Take a mean of the sub-aperture image sequence, calculate the centroid to find the spot centre.
- Find the median pixel intensity within this “mean image”. The majority of pixels are sampled from within the field of view (FOV) such that this gives an estimate of the sky background intensity.
- Set the pixels within a circular section centred around the spot centre to the median value. The radius of the circular section is determined by the size of the FOV and level of wind shake expected (in simulation this radius could be very small).

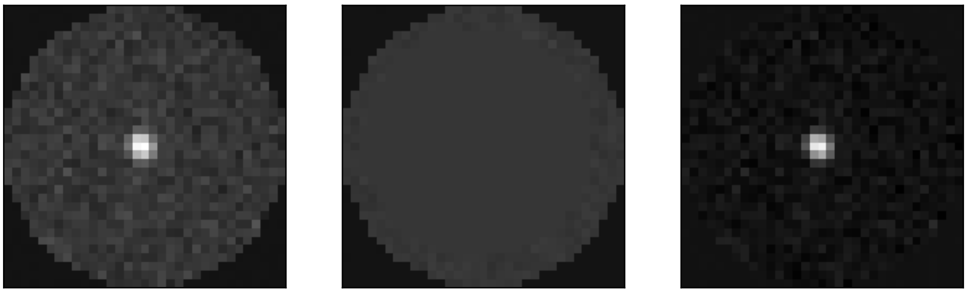

Figure 4.2: Background subtraction process used by the SHIMM showing from left to right: the first frame in the sequence of raw sub-aperture images, the average background image constructed by masking the spot and filling in values with the median background level and finally the background-subtracted first frame of the sequence. Shack-Hartmann images are simulated for daytime conditions and include the effect of a circular field-stop in the back focal plane of the telescope.

- Subtract this mean image from all frames in the sequence to remove the background without significantly affecting spot photometry.

Figure 4.2 illustrates three key stages of this process: the first raw frame in the image sequence before background subtraction, the mean with the spot masked out and the first frame in the sequence after subtracting this background image.

4.3.2 Centroiding

Simulations were used to determine the best-performing centroiding method for the combination of spot size, noise level and expected range of centroid variances. These were individual simulations of a single layer at the ground (and so do not include the influence of scintillation) for a large range of r_0 values covering expected strong "daytime" turbulence of $r_0 < 5\,\mathrm{cm}$ ($\lambda = 500\,\mathrm{nm}$), and very good seeing conditions of $r_0 > 30\,\mathrm{cm}$ to represent measurements at astronomical observatories. Detector noise with the values quoted in section 4.3 was added to the simulations, and a shot noise of $11300e^-$ per spot per exposure was used which was roughly equivalent of a J band star of magnitude 0.07.

These simulations were then run through the data analysis software to extract the measured tip and tilt subtracted slope covariances and the theoretical slope covariances calculated using the input $C_n^2(h)\,\mathrm{d}h$ of the simulation. They were analysed both using the correlation centroiding algorithm with parabolic fitting to the correlation maximum supplied by L. Bardou and a brightest pixel centroiding algorithm from AOtools. For the former, the degree of padding in the Fourier transforms used to calculate the correlations was varied, and for the latter the number of brightest pixels was changed. The resulting reduced χ^2_ν fit of the measured x-slope covariance matrix to the theoretical matrix (excluding the centroid variance terms which are biased by noise) and the difference between the measured and theoretical centroid variances derived from equation 3.9 were calculated for each variation of the algorithms.

Figure 4.3 shows the results of this experiment comparing the performance of the brightest pixel and correlation centroiding algorithms on a simulated SHIMM SHWFS. The figure shows that all brightest pixel algorithms exhibit a significant deviation from the theoretical model above $r_0 = 5\,\mathrm{cm}$. The best performing brightest pixel choice is for 9 pixels which remains below $\chi^2_\nu = 3$ until $r_0 = 10\,\mathrm{cm}$. The inaccuracy for large values of r_0 is likely a combination of the small angular motion in good seeing conditions, and large angular size of the PSF making the measurements highly sensitive to noise. Choosing a number of pixels that would sample only the core of the PSF, for example six, results in unstable measurements from picking pixels outside of the PSF core due to noise. It is also expected that using a large number of pixels would result in very weak thresholding of the spot, potentially sampling the G-tilt rather than the Z-tilt, and a large contribution from readout noise which is a dominant noise source on the SHIMM. The correlation centroid exhibits a significant improvement over the brightest pixel method. The zero-padded correlation centroid performs similarly to the brightest pixel methods

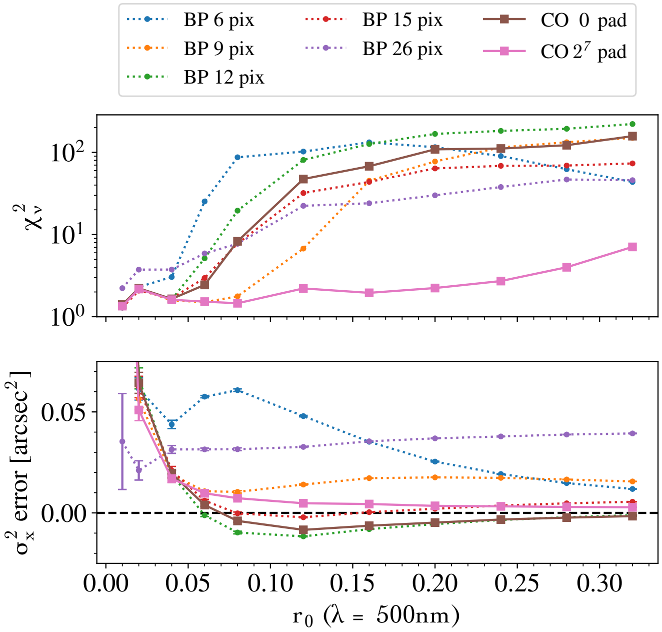

Figure 4.3: Top: A plot of the χ^2_ν goodness of fit of simulated centroid covariances, with added daytime detector noise, for the SHIMM WFS geometry to theoretical covariances over a range of r_0 values. Bottom: fractional error in the centroid variance from simulation compared with the theory plotted against the r_0 of the simulation. Each dotted line represents a different number of brightest pixels (BP), the solid lines represent the result using a correlation centroid (CO) with a different number of pixels for padding. Simulations do not include optical propagation of distorted wavefronts.

at larger values of r_0, however when the results are padded using an array of size 2^n instead of the sub-aperture size of 33 pixels there is a significant improvement for $n = 7$, where $\chi^2_\nu \leq 2$ up to $r_0 = 20\,\mathrm{cm}$.

4.3.3 Centroid noise estimation

Accurate measurement of the centroid noise is extremely useful for debiasing both the slope covariance matrices that are used in the $C_n^2(h)\,\mathrm{d}h$ profile inversion and the defocus structure function in the calculation of coherence time. Estimating centroid noise from WFS data is a well-studied problem with a number of different approaches other than relying on theoretical expressions such as equation 3.13.

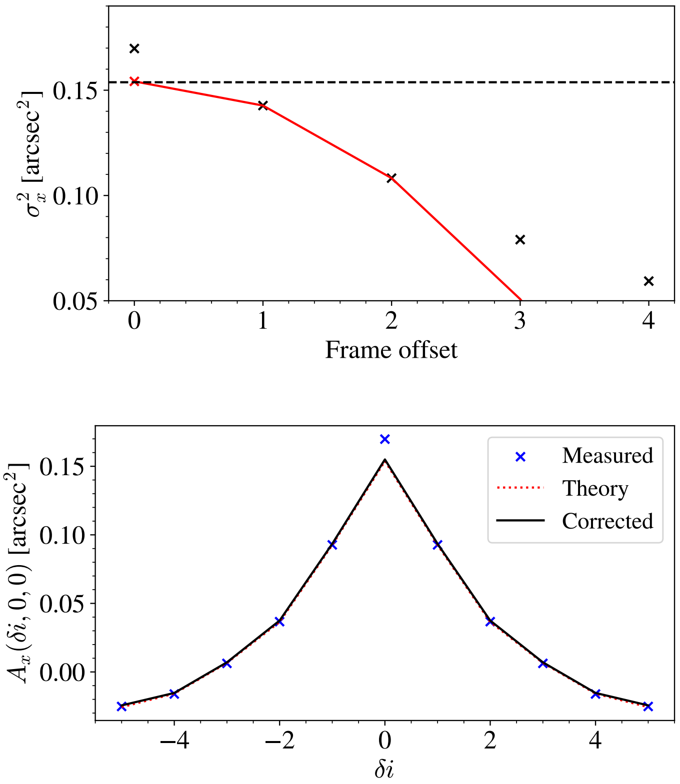

Figure 4.4: Top: Illustration of the centroid noise measurement via extrapolation of the decay curve of the temporal autocorrelation of centroid motion. The black crosses represent the measurements averaged over all sub-apertures from simulation, the black dashed line the theoretical Z-tilt centroid variance, the red line a parabola fitted to the first and second frame offsets with the extrapolated unbiased centroid variance at zero-offset. Bottom: A slice through the auto-covariance map of the x slopes for the data used in extrapolation plot, showing the theoretical response, the measured response from the simulation and the corrected simulation measurement using the centroid noise estimated through the extrapolation method subtracted according to equation 3.13. The theoretical and corrected curves are virtually overlapping.

In SLODAR the centroid noise is measured by first fitting the impulse functions excluding the centroid variance terms which contain most of the noise. The centroid noise is then estimated by extrapolating the impulse function fitting to the centroid variance term and the difference between this value and the measured centroid variance yields an estimate of the noise level. This method is less suitable for the SHIMM as the shape of its slope impulse functions can depend strongly on the height of the fitted layer and so the centroid noise would have to be instead included in the inversion matrix - which is already ill-conditioned. Another method of calculating the centroid noise in each sub-aperture is detailed in Gendron and Lena (1995). To summarise, the method relies on the observation that temporal auto-correlation of the centroid motion is approximately parabolic for very small temporal offsets, and that the centroid noise is uncorrelated in different image frames. This results in a delta function at $\tau = 0\,\mathrm{s}$ in the auto-correlation of spot motion corresponding the centroid noise contribution, and a decreasing parabola for the subsequent few values of τ. By fitting a parabola to these points and excluding $\tau = 0\,\mathrm{s}$, the curve can be extrapolated to zero to estimate the true unbiased centroid variance. The difference between this value and the measured centroid noise corresponds to the noise level in each sub-aperture. This process is illustrated in figure 4.4 which shows both the process of parabola fitting to the autocorrelation function and the resulting correction to the auto-covariance measurements of the SHIMM. This improves agreement of the measurements with theoretical result and allows for using centroid variances in the profile inversion.

4.3.4 Intensity measurement

Spot intensities were calculated by summing the intensity of pixels in a small square window around the centroid position. There were several considerations for the optimal size of the square window. Following the centroid studies, similar single-layer simulations were performed under daytime detector noise conditions for a range of scintillation strengths as determined by the Rytov variance. The Rytov variances were linearly spaced between 0 and 0.5 at $\lambda = 500\,\mathrm{nm}$. Ensuring that the Rytov variance was below the critical threshold of 0.3 at the instrument wavelength, as the model is only valid for weak scintillation. The two metrics chosen to evaluate the optimal window size were the χ^2_ν fit of the scintillation covariance matrix, and the difference between the measured sub-aperture scintillation index and theoretical results derived from equation 2.45 after the subtraction of photometric noise.

The results of this study can be found in figure 4.5. For the smallest Rytov variances, the fit to the covariances worsens due to the relative size of the instrument

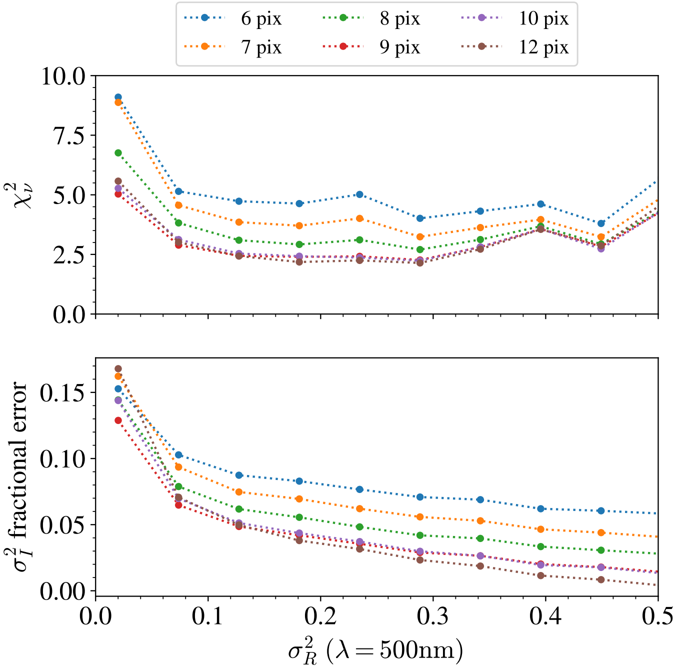

Figure 4.5: Top: χ^2_ν goodness of fit of simulated scintillation covariances to theoretical covariances plotted for a range of Rytov variances in the "weak scintillation" range at the instrument wavelength of 1280nm. Bottom: fractional error in the scintillation index from simulation compared with the theory plotted against the Rytov variance of the simulation. Each coloured line represents a different width of square window around the centroid in which the intensity fluctuations are measured.

response to the convergence noise of the simulations. In the case of the bottom plot of scintillation index, the relative error increases for small Rytov variances where the SNR is low. For larger Rytov variances, although the SNR should be higher due to increased scintillation, and therefore a better χ^2_ν fit might be expected, the uncertainty in the fit begins to increase again. This is likely due to some early saturation of the scintillation covariance matrix as the strong scintillation regime is approached. Disregarding the saturation effects, the plot suggests that for the noise level expected during daytime measurements, a window width of 9 pixels is optimal for fitting to experimental data as it performs better in low-scintillation conditions than all other sizes, and the graphs show little benefit for using larger window sizes across the full range of Rytov variances.

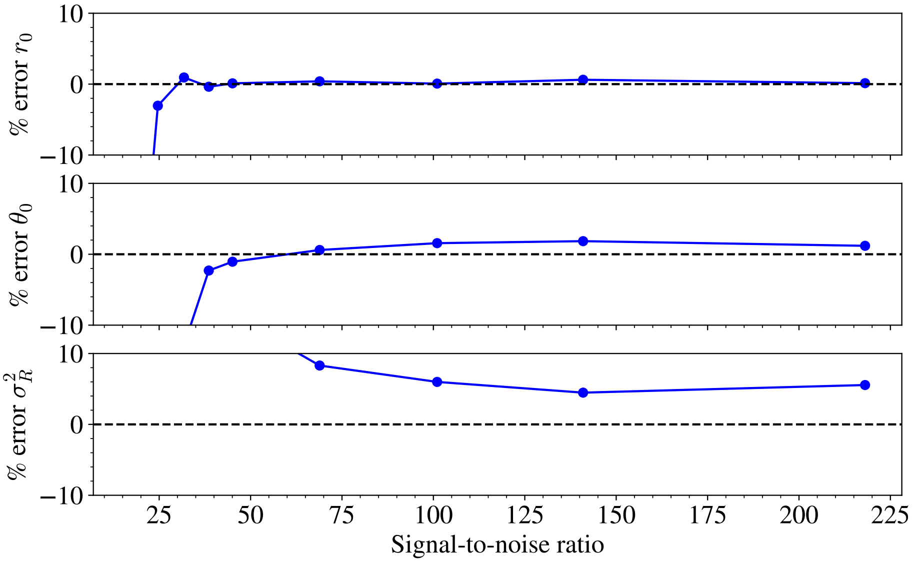

Figure 4.6: Percentage fractional error in the measurement of the Fried parameter (top), isoplanatic angle (middle) and the Rytov variance (bottom) as a function of simulation SNR for a 10-layer HV profile and daytime detector noise.

4.4 Sensitivity limits

By including the expected daytime detector noise in simulations and varying the shot signal, it was possible to investigate the minimum SNR necessary to produce accurate measurements. The input turbulence profile in this study was the HV profile, binned to 10 layers using the equivalent layers method. The SNR of measurements was determined using the number of pixels under the spot centre, that is $N_{\text{pix}} = \pi(\lambda/d\rho)^2$ where ρ is the angular pixel scale in radians. For the SHIMM geometry this was 5.6 pixels. The standard equation could then be used to determine the SNR of simulations. Figure 4.6 shows the results of this investigation. The input simulations were run with SNRs ranging from 10 to 225 and the resulting fractional errors in three of the major turbulence parameters r_0, θ_0 and σ_R^2 were recorded. It was found that for accurate estimation of r_0, a signal-to-noise ratio of approximately 25 was required. However for the isoplanatic angle and Rytov variances, a much greater SNR of 70 was necessary. These parameters are far more closely influenced by higher altitude turbulence. They appeared to require higher SNR to be fit accurately. For the HV profile, there was also a significant bias of around 5% on measurements of the Rytov variance even at large SNR. This was purely a feature of the profile in this case as the validation plots in the following section suggest that this problem was not systematically present for SCIDAR profiles.

4.5 Integrated parameters validation

Figure 4.7 shows the turbulence parameters estimated in end-to-end Monte Carlo simulations with daytime noise and a source intensity of $11500e^-$ per spot per exposure, equivalent to a star with a J band magnitude of 0.07 as determined in the instrument design section in the following chapter (section 5.2.5). The input turbulence profiles were randomly sampled from the Stereo-SCIDAR database at Paranal, Chile (Osborn et al., 2018) and binned down to 10-layers using the method of equivalent layers. Additionally, the ground-layer turbulence strength was “boosted” in a number of profiles to increase the range of r_0 values tested and mimic the increased surface layer strength that might be encountered during the daytime. The simulations were run for the SHIMM optical design detailed in table 5.1. They did not include a wind-speed component and did not to take into account exposure time or polychromatism of the source, and therefore could not be used to validate the coherence time. All plots indicate very strong agreement with the simulation inputs. Correlation coefficients are very close or exactly equal to 1, and linear regression gradients close to 1 with small offsets. Visually there is very little spread in the data in r_0 and θ_0. Rytov variance however appears to have significantly more spread. This could be a result of strong scintillation from low-altitude turbulence which would be difficult for the instrument to measure with its large sub-apertures. Indeed the altitude of the layer that would produce scintillation speckles equivalent to the sub-aperture size for this SHIMM design would be approximately 1.7 km. It

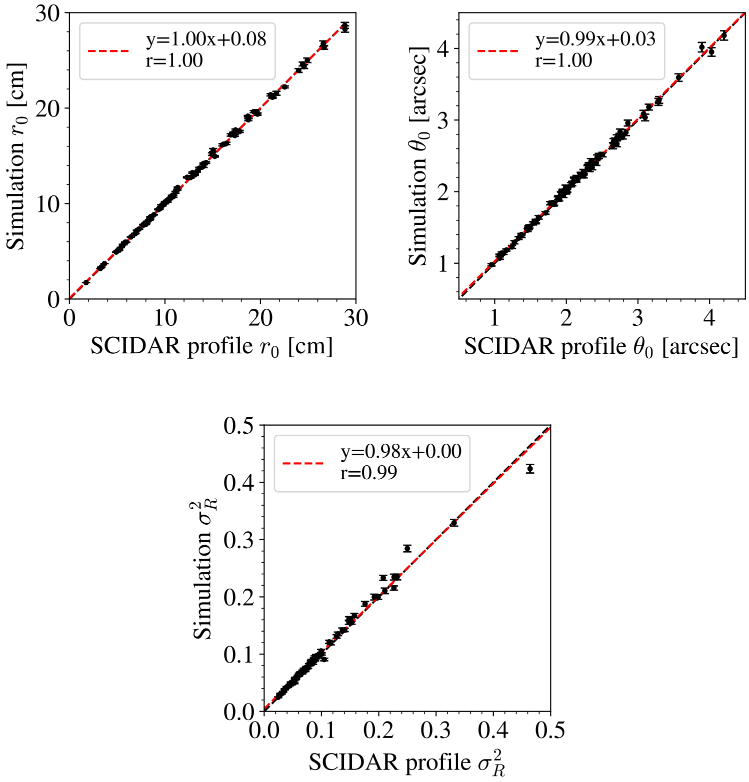

Figure 4.7: Parameter measurement methods were tested via end-to-end Monte Carlo simulation of the instrument using measured vertical turbulence profiles from the Stereo-SCIDAR instrument as input. The panels show the coherence length, coherence angle on the top row and Rytov variance on the bottom row. The red dashed line shows the linear best-fit for the data calculated through linear regression, and a black dashed line indicates the perfect instrument response. r indicates the value of the Pearson correlation coefficient for the data. Simulations were carried out for monochromatic light with a wavelength of 1280 nm, however parameters reported in this figure have been corrected to their values at 500 nm.

is expected that the sensitivity from the intensity part of the reconstruction process would be low for turbulence at this altitude.

The validation of the coherence time measurement method was carried out separately. It relied instead on infinite phase screens to simulate high frame rate (500 Hz) imaging of optical turbulence. These simulations were much slower to converge than the independent phase screens used to investigate the profiling accuracy. Therefore a much larger number of frames were required, limiting the simulation complexity to three layers and fewer overall profiles. Figure 4.8 displays the measured

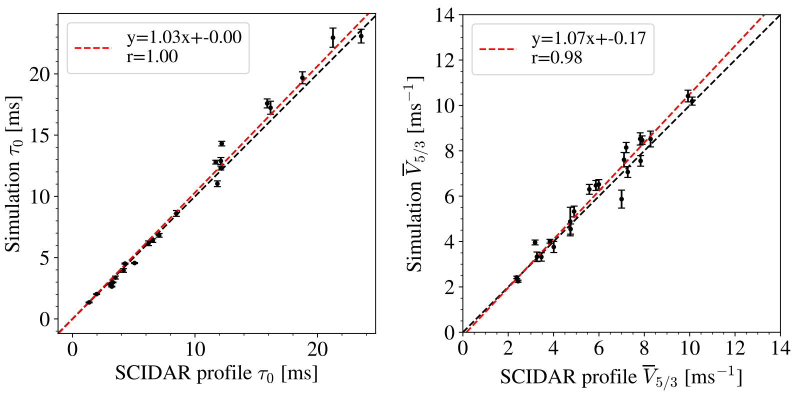

Figure 4.8: Results of measurements of the coherence time (left) and effective wind velocity (right) from end-to-end Monte Carlo simulation of the instrument. Input vertical $C_n^2(h)\,\mathrm{d}h$ and wind speed profiles were taken from the Stereo-SCIDAR database and binned to three layers using the equivalent layers method. The red dashed line shows the linear best-fit for the data calculated through linear regression, and a black dashed line indicates the perfect instrument response. r indicates the value of the Pearson correlation coefficient for the data. Simulations were carried out for monochromatic light with a wavelength of 1280 nm, however parameters reported in this figure have been corrected to their values at 500 nm. The simulations use infinite Kolmogorov phase screens to allow for temporal analysis of SHWFS measurements.

coherence time and effective wind velocity, defined in equation 2.55, from these simulations against the input values. The agreement is not quite as good as for terms derived from only the $C_n^2(h)\,\mathrm{d}h$ profile. There is some small scatter about the trend line for coherence time and slightly more for $\overline{V}_{5/3}$. The greater scatter is likely a limitation of the secondary non-linear least squares inversion problem for fitting a wind speed profile being sensitive to noise as a result of ill-conditioning. The high correlation coefficient and best fit line close to the optimal result suggest however that the method is valid. Finally, it is noted that without subtraction of the noise bias from the defocus structure function, there was a significant bias towards a larger effective wind velocity and a trend line gradient of 1.21 instead of 1.07. The noise subtraction is therefore a critical step to obtaining accurate measurements of the coherence time during the daytime.

4.6 Turbulence profiles and regularisation

The accuracy and resolution of the SHIMM profile inversion technique is strongly limited by noise and non-orthogonal weighting functions. The columns of the design matrix are therefore not fully independent, the matrix can be considered somewhat singular and the problem is ill-conditioned. As evident from figure 3.6, including additional layers leads to a steep increase in the matrix condition number and accentuates this issue. The constraint of non-negative solutions further complicates matters as terms in the solution vector where the $C_n^2(h)\,\mathrm{d}h$ would have been negative typically return zero. Considering the large database of SCIDAR measurements at Paranal, this seems unphysical for the wide SHIMM response functions. A number of studies have utilised regularisation to attempt to improve measurements from optical turbulence profilers (Védrenne et al., 2007; Chabé et al., 2020; Voyez et al., 2014). However these approaches typically focus on the second order Tikhonov regularisation, which enforces profile smoothness. A real turbulence profile is however anything but smooth, and so instead this work uses the classical Tikhonov regularisation problem where $\mathbf{L} = \mathbf{I}$. These studies use the L-curve criterion to choose the optimal value of the regularisation parameter, however in simulations for the SHIMM the L-curve did not have a distinct corner and so this method could not be used successfully.

In this work, the choice of the regularisation parameter is determined through the criterion of the Gaussian “whiteness” of the least-squares residuals. Almeida and Figueiredo (2013) argue that the choice of regularisation parameter that produces the most Gaussian residuals will be optimal as it infers that residuals are primarily resulting from random noise rather than fitting errors due to ill-conditioning. The whiteness of residuals is evaluated using the auto-correlation of the normalised vector of residuals. For an optimal fit to the data, the noise in each residual term should be independent and therefore the noise manifests as a delta function at the origin of the autocorrelation function. The maximum whiteness can be evaluated by

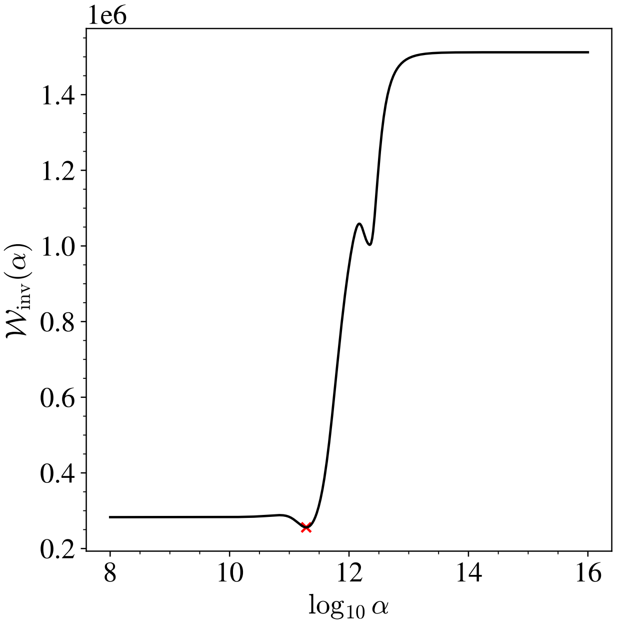

Figure 4.9: A plot of the inverse whiteness metric $\mathcal{W}_{\mathrm{inv}}$ against the logarithm of the regularisation parameter for a simulated optical turbulence profile. The red cross marks the point of maximum whiteness successfully located through the dual annealing algorithm.

summing the square of the normalised residuals outside of the origin and reasoning that when this is minimised, the maximal amount of energy can be found in the origin. Figure 4.9 shows the sum of the square autocorrelation of the residuals outside of the origin, referred to as inverse whiteness, of a regularised least squares solution for a simulated profile plotted against the logarithm of the regularisation parameter. The flat sections at the extremes of the x-axis, corresponding to on the left the under-regularised solution and on the right the over-smoothed solution, present difficulties for simple minimisation algorithms. It was found that a global minimisation algorithm was necessary to find this point. This work implements the dual annealing algorithm (Xiang et al., 1997) for this purpose.

4.6.1 Four layers

Simulations were first analysed with four layers at the heights chosen by the condition number analysis in section 3.5: 0, 4, 12 and 20 km. The simulation dataset was the same as that used in section 4.5. The simulations consisted of 10 layers placed at heights calculated through the equivalent layers method. To enable a comparison of the input profiles with the SHIMM measurements, the input profiles were binned down to four layers using the instrument response functions (figure 3.7). This was accomplished by multiplying the input 10-layer $C_n^2(h)\,\mathrm{d}h$ profile from the simulation by the normalised response functions for each SHIMM layer. The resulting array of input $C_n^2(h)\,\mathrm{d}h$ values was then summed to give a binned $C_n^2(h)\,\mathrm{d}h$ value at each of the layer heights in the SHIMM reconstruction. Figure 4.10 compares the results of using a weighted least squares approach to solve the inversion problem with a regularised least squares approach using zeroth-order Tikhonov regularisation and the Gaussian whiteness criterion to choose the regularisation parameter α. As the number of fitted layers increases, the non-negative least squares inversion tends to produce measurements of $C_n^2(h)\,\mathrm{d}h = 0\,\mathrm{m}^{1/3}$ in the bins. Although it has been observed that atmospheric turbulence is concentrated in thin layers throughout the atmosphere (Osborn et al., 2018), for the small layer numbers fitted by the SHIMM none of the bins should return zero. This is because the response functions are typically kilometres wide and so should average out the turbulence from a number of layers. In the following two plots, simulations where the standard weighted least squares approach gives $C_n^2(h)\,\mathrm{d}h = 0\,\mathrm{m}^{1/3}$ and the regularised version gives a non-zero $C_n^2(h)\,\mathrm{d}h$, are represented by red triangles. In the four layer case - which is unlikely to be severely ill-conditioned - it appears that there is little benefit to using regularisation over weighted least squares. The agreement in the first two layers is slightly worse with regularisation included and the bias in the 4 km layer notably increases at the expense of the ground layer. This can be seen in table 4.1 where the 4 km layer bias increases from 0.173 to 0.555 while the 0 km layer bias decreases from -0.010 to -0.052. The agreement in the upper two layers however slightly improves with a reduced bias while maintaining a similar RMSE and correlation. Additionally, the number of zero-$C_n^2(h)\,\mathrm{d}h$ layers only very slightly decreases with regularisation. The overall result here suggests that the regularisation parameter chosen through Gaussian whiteness is very slightly over-smoothing the resulting profile in transferring $C_n^2(h)\,\mathrm{d}h$ from the ground layer to the 4 km layer and offers little benefit when the profiling is restricted to only four layers.

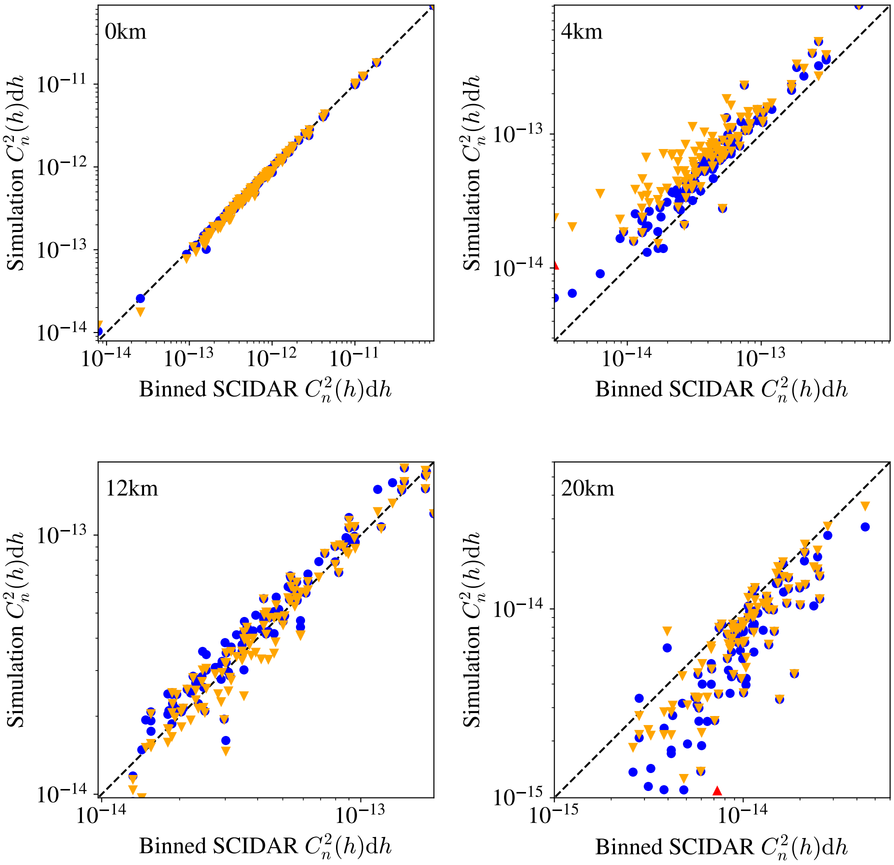

Figure 4.10: Scatter plots of $C_n^2(h)\,\mathrm{d}h$ measured in each SHIMM layer compared with the binned input profiles to the simulations, for a four-layer reconstruction. The blue dots represent the weighted least squares method with no regularisation, orange triangles represent the zeroth-order Tikhonov regularised solution using the Gaussian whiteness method, and the red up-facing triangles indicate layers which were zero in the weighted least squares case but non-zero when using regularisation.

4.6.2 Six layers

When using six-layers instead, the ill-conditioning of the problem is expected to increase significantly. This is reflected in the number of layers with a $C_n^2(h)\,\mathrm{d}h$ of zero, and the worsened agreement between the input and simulation measure-

	Weighted LS				Regularised LS			
Layer h (km)	r	RMSE	B	NZ (%)	r	RMSE	B	NZ (%)
0	1.00	0.03	-0.02	99	1.00	0.04	-0.04	99
4	0.97	0.09	0.15	98	0.95	0.17	0.26	99
12	0.97	0.07	0.03	99	0.97	0.07	-0.00	99
20	0.83	0.20	-0.22	83	0.80	0.20	-0.17	84
0	1.00	0.23	-0.01	99	1.00	0.055	-0.05	99
3	0.81	0.31	0.17	92	0.53	0.438	0.56	97
6	0.71	0.40	0.11	82	0.75	0.377	-0.05	72
9	0.70	0.39	0.01	72	0.79	0.311	-0.04	87
12	0.52	0.42	-0.06	63	0.62	0.422	-0.11	78
16	0.63	0.33	0.01	95	0.73	0.265	0.03	97

Table 4.1: A summary of all statistical comparison parameters calculated from the base-10 logarithm of the $C_n^2(h)\,\mathrm{d}h$ measurements. The table includes data from both the four-layer and six-layer examples corresponding to the results in figures 4.10 and 4.11.

ments. As in the four-layer case there is systematic overestimation in the first atmospheric layer when using regularisation. The layer at $C_n^2(h)\,\mathrm{d}h = 3\,\mathrm{km}$ shows an obvious bias when compared with the unregularised solution. There is however significant improvement in agreement for the higher-altitude layers as reported by table 4.1. The number of layers which are zero without regularisation and non-zero with regularisation, highlighted by the red up-facing triangles on the plot, increases significantly. This is especially prominent in the 9 km and 12 km layers. Regularisation in this case appears to be sacrifice some accuracy in the first two layers to improve the characterisation of the profile in the upper atmosphere. Improvements in these results can likely be made by restricting the target magnitude to use brighter stars and fitting a variable number of layers based on the current SNR level.

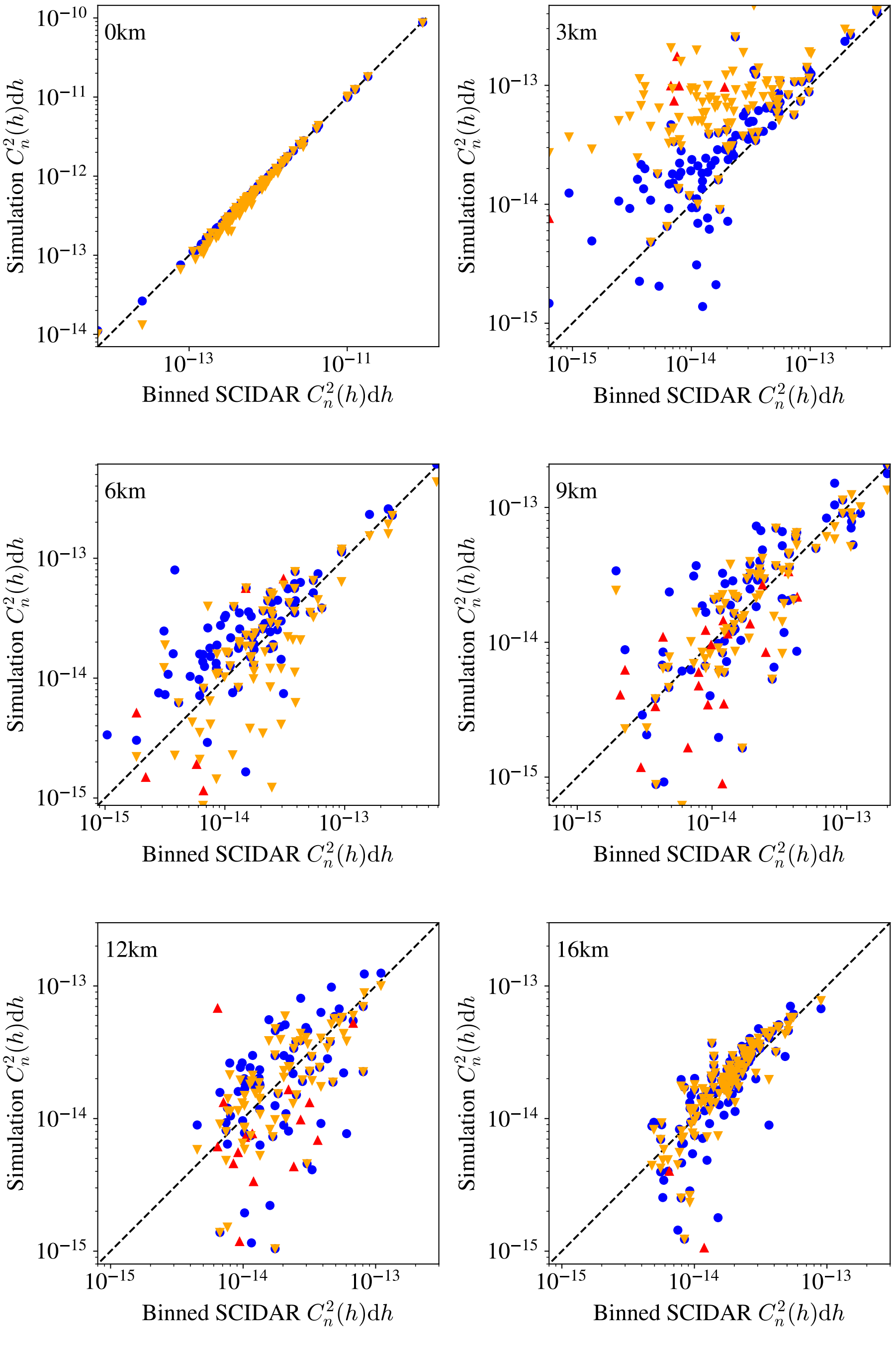

Figure 4.11: Scatter plots of $C_n^2(h)\,\mathrm{d}h$ measured in each SHIMM layer compared with the binned input profiles to the simulations, for a six-layer reconstruction. The blue dots represent the weighted least squares method with no regularisation, orange triangles represent the zeroth-order Tikhonov regularised solution using the Gaussian whiteness method and, the red up-facing triangles indicate layers which were zero in the weighted least squares case but non-zero when using regularisation.

4.7 Conclusion

Chapter 4 explored the image analysis algorithms used by the SHIMM and evaluated their accuracy in simulations through comparison with theory. This was primarily to validate the forward model in the inversion problem. This involved choosing the window size of the intensity measurements and optimal configuration of the centroiding algorithm. This study determined that a correlation centroid with padding and using a parabolic fit for sub-pixel accuracy offered improvement over a brightest pixel centroider. It was also found that a parabolic extrapolation of the temporal auto-correlation of the centroid motion to the origin was a suitable method for estimating the centroid noise. For the measurements of scintillation, a square window of 9 pixels in width was also determined optimal for the chosen SHIMM geometry and daytime noise. Following this, it was found by varying the shot signal in daytime-level noise that a SNR of 70 was desirable to produce accurate measurements of all optical turbulence parameters. It will be shown in the following chapter that this is equivalent to a J band magnitude of 0.07 for the SHIMM. The accuracy of the estimation of the Rytov variance was the limiting factor in this study, however a different choice of profile might yield a lower required SNR. Finally, the accuracy of both integrated parameter measurements and the optical turbulence profiles are evaluated using 100 simulations which use real optical turbulence profiles from the Paranal SCIDAR database. The integrated parameter measurements are all found to agree extremely well with the simulation inputs, including the coherence time which was evaluated using a smaller set of simulations that also included the wind speed. The optical turbulence profiles show good agreement for the four-layer case but a worsened agreement for a six-layer case. It was found that using regularisation may offer some improvement in characterisation of higher altitude layers, but came at the expense of producing a bias in measurements of the first two layers.

Chapter 5

The SHIMM design

5.1 Introduction

So far, discussion of the SHIMM instrument has focused on the analysis of SHWFS images. This chapter will describe the opto-mechanical design, control software and data analysis pipeline of the instrument. It will show that the SHIMM represents a portable, relatively low-cost and effective method of measuring day and night optical turbulence conditions. The SHIMM optical design is based on an early night-only prototype (Perera, 2017; Perera et al., 2023) developed at Durham University using mostly commercially available components. However, the current iteration represents a significant hardware upgrade with a number of modifications to enable 24-hour monitoring of optical turbulence. The instrument is based around a 28 cm telescope and SWIR SHWFS. By measuring at SWIR wavelengths, the SHIMM experiences the triple benefits of weaker optical turbulence, significantly reduced sky background noise during the daytime and far more suitable bright star targets. It will be shown that this is key to enabling accurate measurements of optical turbulence in daytime conditions. The opto-mechanical design is adapted to supporting the InGaAs camera technology, and the acquisition and analysis of high frame rate data is handled by AO real-time control techniques. The practical elements of performing an experiment such as calibrations and target availability will also be discussed alongside the logic behind automated data acquisition routines.

5.2 Optical design

A full schema of the SHIMM design is displayed in figure 5.1. In summary it consists firstly of an f/10 telescope, which was chosen as an f-number that is a multiple of five ensures a more convenient pairing with commercially available lens focal lengths and microlens array diameters. Additionally, a small FOV is desirable for reducing background light. A field stop is placed in the back focal plane of the telescope to limit the FOV of each sub-aperture and ensure that background image for each lenslet does not overlap with the adjacent ones. For the SHIMM the field stop is a motorised iris that can fully close and act as a shutter. This provided the additional benefits of being remotely operable, allowing the taking of dark frames at regular intervals to combat the changing temperature of the sensor, and for precise control of the FOV of the instrument. Following the field stop, a lens of effective focal length f_{col} collimates the beam from the telescope observing a star. Given that the SHIMM is a wide-bandpass instrument an achromatic doublet was chosen for this lens to minimise chromatic aberrations. The microlens array of focal length f_{mla} is then placed at a distance d_{conj} from the collimating lens. This distance is optimised in optical design software to ensure that the microlens array is conjugated to the telescope pupil plane. Finally the microlens array focuses the light onto an InGaAs sensor.

The optical components used in the SHIMM design are listed with focal lengths and other relevant information in table 5.1. The optical components are, where possible, chosen with a NIR II coating to maximise throughput of SWIR light. This choice of components results in a beam diameter of 3 mm from the collimating lens. The lenslets have a pitch of 500 µm leading to six Shack-Hartmann sub-apertures across the telescope pupil. The active subapertures in the Shack-Hartmann sensor are set as those with more than 94% of the aperture unvignetted by the telescope pupil. This configuration leaves 20 active sub-apertures as shown in figure 5.2.

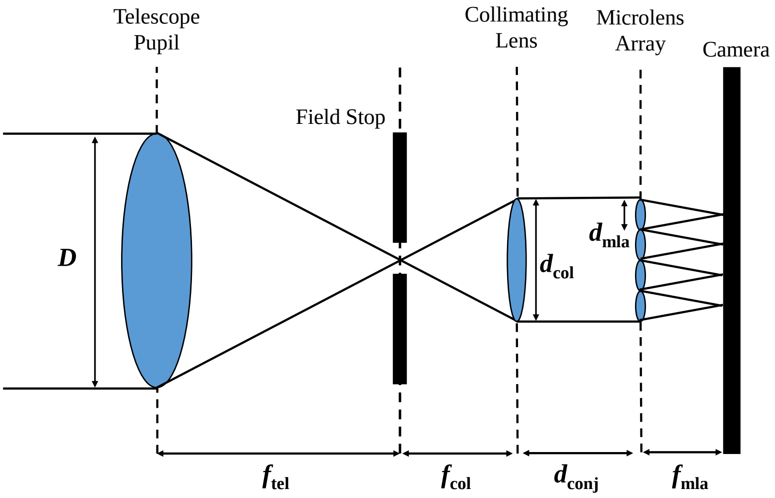

Figure 5.1: SHIMM optical design.

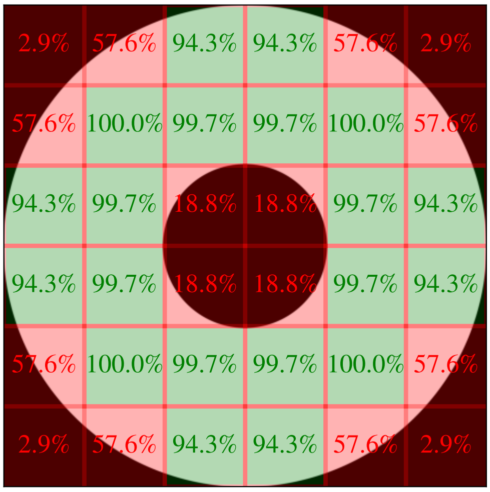

2.9%	57.6%	94.3%	94.3%	57.6%	2.9%
57.6%	100.0%	99.7%	99.7%	100.0%	57.6%
94.3%	99.7%	18.8%	18.8%	99.7%	94.3%
94.3%	99.7%	18.8%	18.8%	99.7%	94.3%
57.6%	100.0%	99.7%	99.7%	100.0%	57.6%
2.9%	57.6%	94.3%	94.3%	57.6%	2.9%

Figure 5.2: Diagram of the telescope pupil sampling by the Shack-Hartmann sub-apertures. Apertures shaded green indicate activate sub-apertures used in the analysis, inactive sub-apertures are shaded red. The percentage of the sub-aperture area that is not vignetted by the pupil is displayed in the centre.

Component	Model	Information
Telescope	Celestron C11 SCT	$D = 0.2794$ m, $f/10$
Field stop	STANDA 8MID10-40	Aperture size = 0-22 mm Resolution/step = 385 μm
Collimating lens	Edmund Optics #45-794	$f_{\rm col} = 30$ mm, $d_{\rm col} = 12$ mm Coating: NIR-II
Microlens array	Edmund Optics #21-159	$f_{\rm mla} = 15.3$ mm, $d_{\rm mla} = 500$ μm Coating: NIR-II
Camera	First Light Imaging C-RED3	Pixel size $\rho = 15$ μm Sensor: InGaAs 640 × 512 pix Max. FPS: 600 (Full frame)

Table 5.1: Optical components of the SHIMM.

5.2.1 Image scale

The image scale of the system can be found modelling the three-lens system using geometric optics, thin lenses and small angle perturbations. The plate scale of the telescope $p = 1/f$ relates angular deflections to physical x, y displacement of the focus in the back focal plane of the telescope. The magnification of the collimating-lens and microlens system then yields the plate scale in the focal plane of the MLA. Multiplication by the pixel-scale converts to angular pixel size,

$$\rho_\alpha = \rho \frac{f_{\rm col}}{f_{\rm tel} f_{\rm mla}} \quad \text{(rads pix}^{-1}\text{)}. \tag{5.1}$$

This ensures that for the SHIMM optics listed in table 5.1, the image scale is approximately 2.17 $''$pix^{-1} and the spot full width at half maximum (FWHM) is 5.65 $''$ such that the spots are comfortably Nyquist sampled by detector pixels.

5.2.2 Conjugation altitude

It is critical for the analysis that microlens array is conjugated near to the telescope pupil, or that the conjugation altitude of the Shack-Hartmann is known to a reasonable degree of accuracy as in the principle of generalised SCIDAR (Fuchs et al., 1998). Otherwise the propagation distances of distorted wavefronts sensed by the instrument can not be related to vertical height above the ground introducing systematic errors. In determining the sensitivity of the instrument to changes in d_{conj}, the two-lens formula yields the following formula for the conjugation height of the instrument,

$$d_t = \frac{f_t(f_c + f_t - \frac{d_{\mathrm{conj}} f_c}{d_{\mathrm{conj}} - f_c})}{f_c - \frac{d_{\mathrm{conj}} f_c}{d_{\mathrm{conj}} - f_c}}. \tag{5.2}$$

In the limit of $d_t = 0\,\mathrm{m}$, i.e. conjugation to the pupil of the telescope, an analytical expression for d_{conj} may be obtained,

$$d_{\mathrm{conj}} = \frac{f_c^2 + f_t f_c}{f_t}. \tag{5.3}$$

For the SHIMM optical design this thin-lens approximation yields $d_{\mathrm{conj}} = 30.32\,\mathrm{mm}$, compared to 30.40 mm determined through the ray tracing software Zemax. By considering $d_t(d_{\mathrm{conj}})$ and $d_t(d_{\mathrm{conj}} + \delta x)$ one can show that the corresponding δt, corresponding to a shift in conjugation altitude caused by a displacement of the microlens array from the collimating lens is given by

$$\delta t = -m^2 \delta x, \tag{5.4}$$

where m is the magnification of the $4f$ f_c, f_t relay ($m = f_t/f_c$). On the SHIMM a 1 mm error in d_{conj} therefore corresponds to an 8 m change in conjugation altitude - it is relatively insensitive.

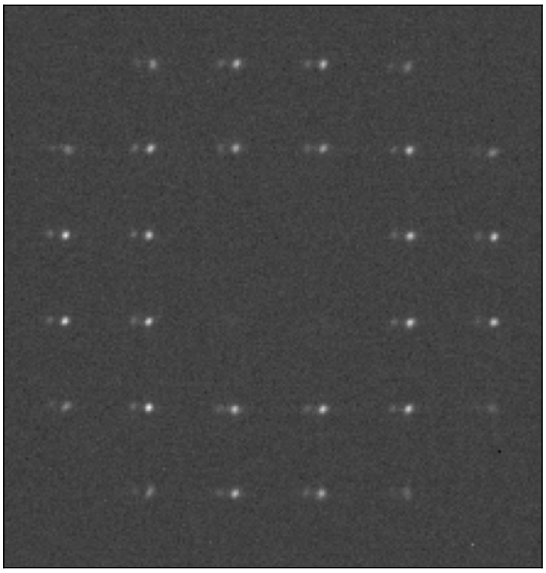

Figure 5.3: Long-exposure image of the Mizar binary system on the SHIMM.

5.2.3 Alignment

The alignment process for the optics involves firstly changing the distance between the microlens array and the camera sensor in order to bring a distant object into focus. Then, the microlens array - collimating lens distance must be set by measuring the distance between the optical mountings and making sure it agrees with that in the 3D optomechanical design in Fig 5.9. The tolerance on this alignment is relatively low as implied by equation 5.4. The alignment of the iris plane to the back-focal plane of the telescope is also set from the opto-mechanical design, and the focus of the telescope is made by adjustment until the correct sub-aperture separation is observed on the detector. Finally, misalignment in these processes can be calibrated by imaging a double star with a known separation, such as the Mizar binary system imaged on the SHIMM in figure 5.3 which has an angular separation of 14.4 $''$, or equivalently 6.6 pixels for a perfect alignment.

5.2.4 Central wavelength

Although the polychromatic simulations in the previous chapter suggest that it is not necessary to take into account the transmission profile when calculating the weighting functions, it is however necessary to characterise the central wavelength of the optical system. In computing the central wavelength, it is convenient to assume that the stellar spectrum is flat across the wavelength range of the instrument. As every star will have a different spectrum this assumption will likely lead to some systematic errors across different targets. The effects of the atmospheric absorption are easier to estimate, in this work the transmission profile is estimated using the LOWTRAN atmospheric modelling software (Kneizys et al., 1988).

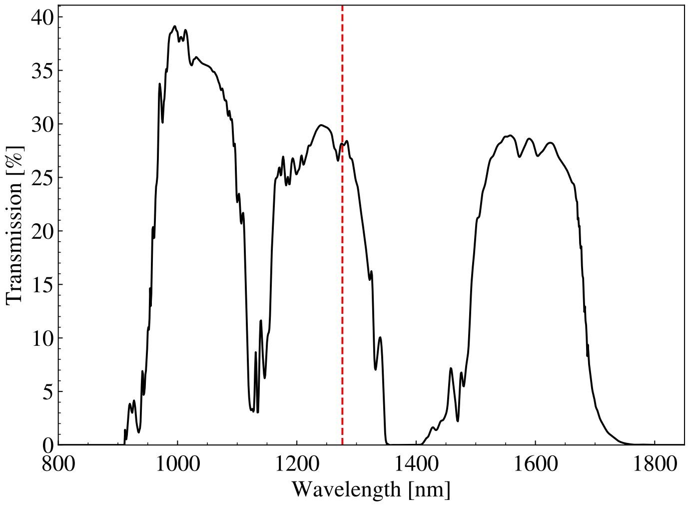

Figure 5.4: The estimated combined transmission spectrum of the SHIMM optical components and the atmosphere. The vertical, red dashed line indicates the value of the central wavelength $\lambda_c = 1280\,\mathrm{nm}$.

The transmission spectra of the optical components were obtained from manufacturer data in all cases except for the telescope. As the telescope manufacturer only specified wavelengths up to 700 nm, an estimate of the transmission spectrum of the telescope was instead made from a study on the transmission of the corrector plate (Baril et al., 2010). Cubing this value to obtain the transmission from the three surfaces in the telescope. Figure 5.4 shows the estimated transmission spectrum of the instrument and atmosphere with the central wavelength, computed as the average wavelength weighted by the transmission spectrum, marked as a vertical dashed line.

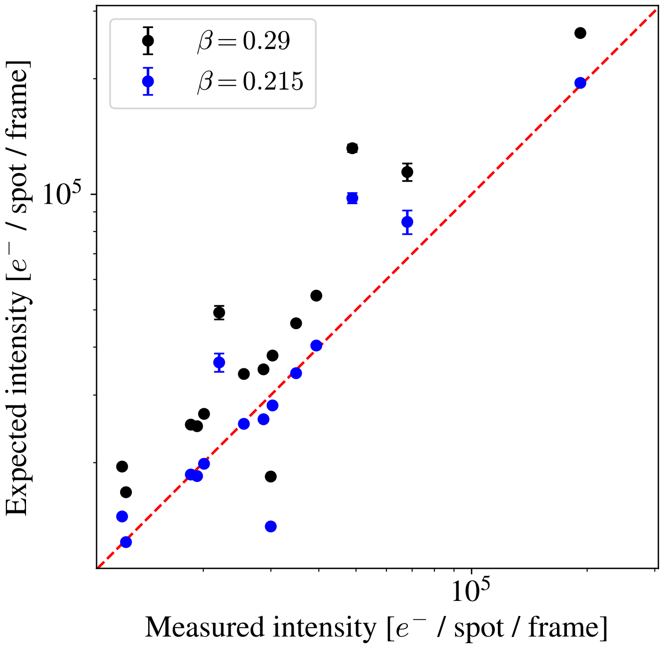

Figure 5.5: Measurements of star intensity in units of photo-electrons per exposure in a single spot plotted against the expected star intensity from the transmission spectrum of figure 5.4. For an average transmission of 0.29, calculated directly from figure 5.4 in black, and for a corrected transmission of 0.215. Each data point refers to the average intensity across all observations of a given star.

The accuracy of this transmission spectrum is investigated in figure 5.5. In this figure, the measured average intensity in each spot in units of photoelectrons per frame is plotted for a number of stars against the expected intensity given the average transmission, β, calculated from figure 5.4. The estimated transmission of $\beta = 0.29$ appears to overestimate compared to the measured signal from the star. The causes of this and some of the outliers could be any of: dust on the corrector plate, aerosols, thin clouds, imperfections and dirt on the optics and the accuracy of the telescope transmission estimate. Furthermore, this analysis makes no corrections for the stellar spectrum which likely adds to the spread of the data significantly. From figure 5.5, it can be seen that a lower average transmission of

$\beta = 0.215$ greatly improves the accuracy of the estimate and so this correction is adopted going forward.

5.2.5 SNR and target availability

To assess target availability, first an estimate of the minimum viable signal-to-noise ratio was necessary. This was determined as approximately 70 in the previous section to obtain accurate results. This SNR was then used to calculate the number of signal photons in the J band using the standard equation, assuming a diffraction limited spot, the same values for readout noise, and background noise as given in section 4.3 and the estimate of the telescope transmission as above. To visualise the effect of changing aperture size on SNR and the maximum permissible target magnitude, figure 5.6 shows J band star magnitude plotted against resulting SNR for a number of different aperture sizes corresponding to SHIMM optics on a 20, 28, 36 and 50 cm, f/10 commercial telescope.

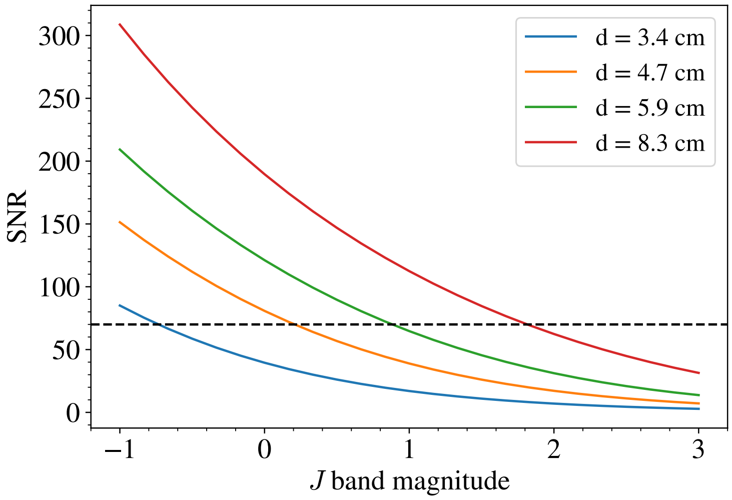

Figure 5.6: Estimated signal to noise ratio within one sub-aperture on the SHIMM for a number of different aperture sizes plotted against the target star J band magnitude.

J band magnitudes were used to best match the central wavelength of the instrument at 1280 nm. The minimum SNR suggested by figure 4.6 of 70 is marked by a black dashed line. It was found that for the C-11 SHIMM the maximum magnitude was 0.07. When varying the sub-aperture size, other factors such as angular spot size and changes in the performance of the reconstruction due to subaperture size are not controlled for. This graph alone therefore cannot be used to define the cutoff magnitudes for sub-aperture sizes other than 4.7 cm, however it can be used as a rough guide.

Parameter	Limit
J magnitude	≤ 0.07
Zenith angle	$\leq 45°$
Sun separation	$\geq 30°$
Moon separation	$\geq 15°$

Table 5.2: Conditions for valid target stars for the SHIMM.

The star catalogue used to find valid targets was the Vizier Bright star catalogue (Ducati, 2002) as figure 5.6 indicates only bright stars are useful and the catalogue includes J band colour information. To investigate target availability a number of additional critical thresholds were defined to filter out targets. These have been summarised in table 5.2.

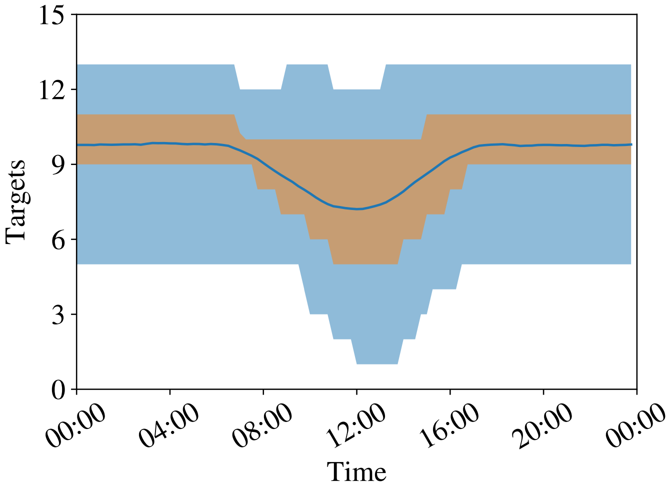

Figure 5.7: Number of valid targets plotted against the time of day for a SHIMM in Barcelona based on the limiting criteria in table 5.2 and data for the year 2024. The blue line is the average number of targets, the orange shaded area indicates the first and third quartiles and the blue shaded are the minimum and maximum.

The magnitude limit is set by combining the results of the figure 5.6 with the results of figure 4.6 in order to find the limiting magnitude to achieve a SNR of at least 70. The number of possible targets over the course of a year for Barcelona is given in figure 5.7 showing that for a limiting J band magnitude of 0.07, there are always targets available. This investigation does not account for extinction due to airmass or the stellar emission spectra.

5.3 Opto-mechanical design

The optomechanical design for the prototype SHIMM was based around a Thorlabs cage rod system. A three-dimensional CAD model of the optics was produced using the Zemax optical design software for integration with an Inventor assembly containing models of Thorlabs components and the camera. Since the beam diameter was small, 12.5 mm diameter lenses and 1/2-inch lens tubes were used. Figure 5.8 shows an annotated diagram of the mechanical design, highlighting key components. These include: an x-y translation stage and a rotation mount to enable alignment of the microlens array subapertures with the detector pixels and telescope pupil, a cage mounted motorised iris diaphragm (Optosigma C30-SSH-17IR) to function as the field stop, and a custom mounting for the microlens array that could screw into a 1/2-inch lens tube. The interface to the telescope is made using a Thorlabs adaptor with SM1 external threads and T-mount internal threads. The cage rods are 4 inches long. It was found that completely enclosing the optics was critical to eliminate ambient light during the daytime. This was accomplished by placing cage system covers into the free spaces between components and covering any remaining gaps with black tape. A further wrapping of aluminium foil was necessary to prevent optics becoming warm in direct sunlight, which could introduce additional tube seeing if left unmitigated.

This almost fully off-the-shelf prototype was subsequently used as a basis by mechanical engineer, Joss Guy, at Durham for producing a custom optomechanical

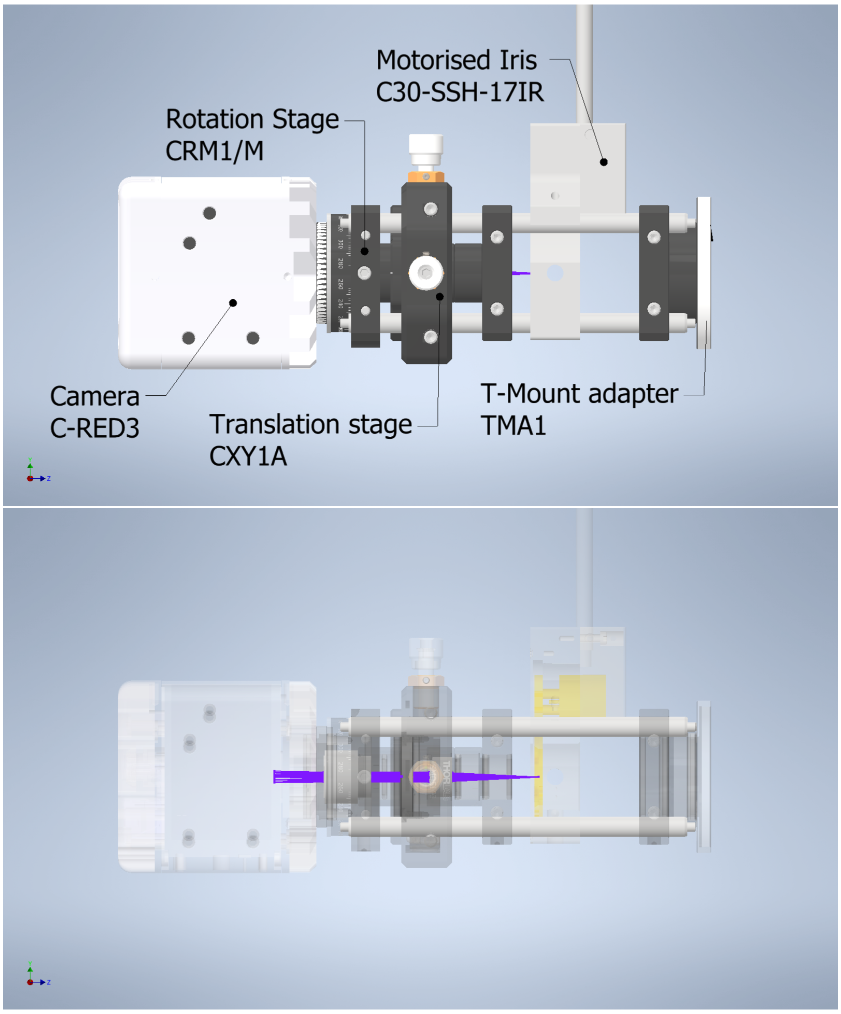

Figure 5.8: Top: Annotated SHIMM Thorlabs-based mechanical design. Bottom: transparent view with optical rays shown from the telescope focal plane onwards.

design for the instrument. This new design included a machined aluminium body, a reduced number of Thorlabs components and a more precise motorised iris. The optics in this design are fully shielded from ambient light and from humidity by o-rings on screws and other components. The aluminium casing greatly reduced instrument flexture which simplified target acquisition. A CAD model of the most current design is shown in figure 5.9. Additional improvements included an aluminium sun shield for the camera, and a solution for direct mounting of the casing onto the rear thread of the Celestron C11 telescope.

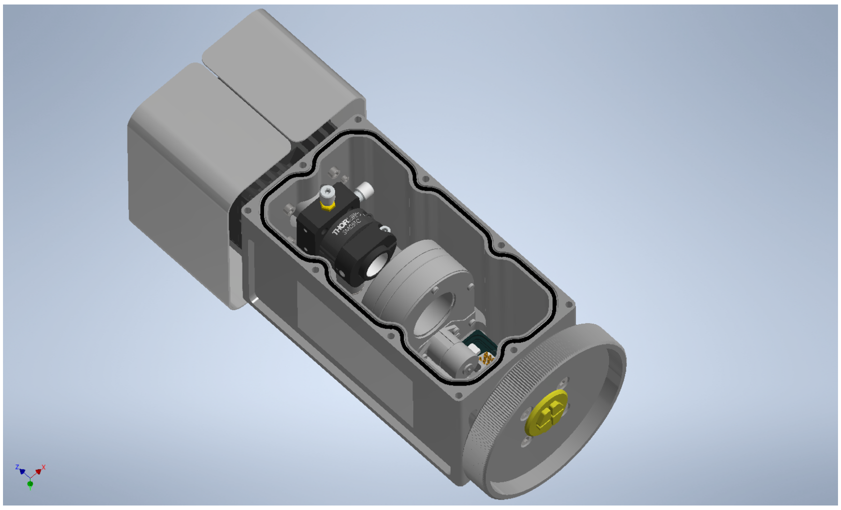

Figure 5.9: Custom optomechanical design with the lid removed.

5.4 Additional hardware

The SHIMM system also included a wide-field finder for acquisition of targets. A wider field of view was necessary as the telescope pointing alone was not sufficient to place a star in the field of view of the wavefront sensor. The solution was a barrel-mounted Skywatcher EVOGUIDE 50ED refractor, with a focal length of 242 mm and $f/4.8$. In order to minimise sky background noise, a ZWO ASI 662MC and 850 nm longpass filter were used. The Bayer filter in the colour camera is opaque above this wavelength and so the camera can function as a mono-camera in the near-infrared. The array of 1920×1080 2.9 µm pixels yielded a field of view of $1.32° \times 0.74°$. The CMOS sensor with the filter is reasonably sensitive to wavelengths in the range from 850 nm to 1100 nm , with a QE of 50% at 850 nm.

The SHIMM also used a computerised equatorial Celestron CGX-L mount which had a programmable interface to allow for automation of guiding and target acquisition from software. The experiment was controlled from a single Ubuntu PC - a HP Z2 G9 mini - chosen for its small form factor and powerful processor. An annotated image of the SHIMM hardware is shown in figure 5.10.

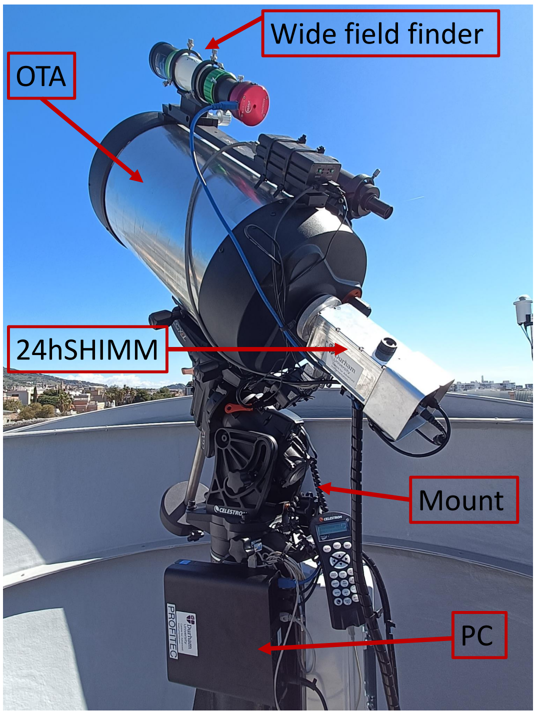

Figure 5.10: Annotated diagram of the SHIMM hardware.

5.5 Software design

Instrument software was written in python 3 for Ubuntu 20.04LTS. The software package for the instrument control was split into three separate repositories each with a separate function: a graphical user interface for control, interaction and data readout from the instrument, the back-end software to interact with instrument hardware for data acquisition, and the data analysis software containing the algorithms discussed in chapters 3 and 4.

5.5.1 Real time control implementation

The hardware diagram for the real time control (RTC) software is shown in figure 5.11. The system design relied on a distributed network of servers implemented through the python package Pyro 5. This included a supervisor server that communicated with a number of sub-servers each controlling a piece of hardware, and the autoguiding and data acquisition.

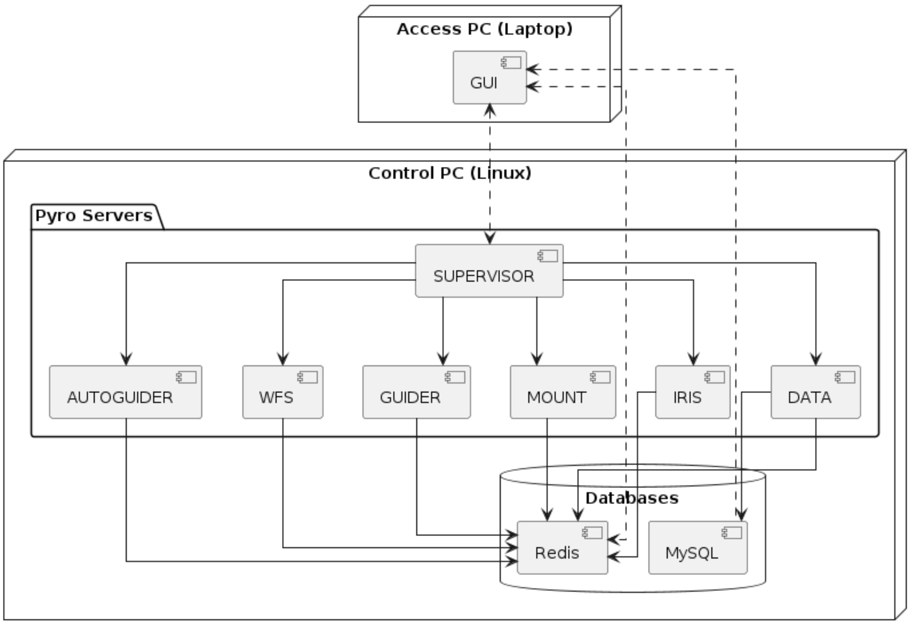

Figure 5.11: Component diagram for SHIMM RTC software showing interaction between the GUI on the access PC and the Pyro servers and databases on the SHIMM control PC.

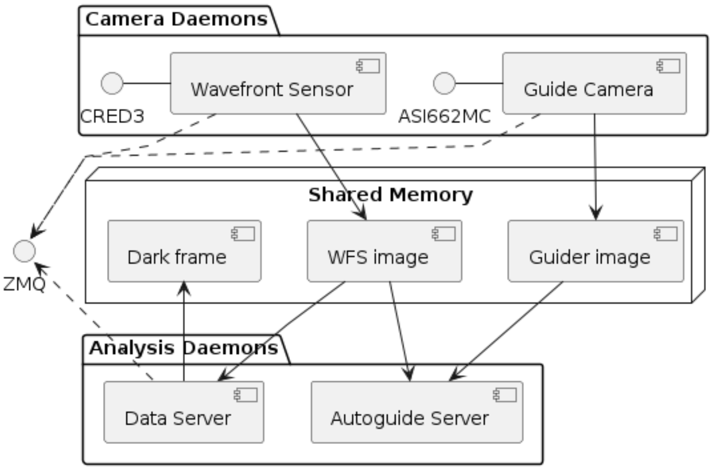

Figure 5.12: Shared memory implementation on the SHIMM for rapid transfer of frames between daemons and publishing of images to ZeroMQ for distribution to GUI client.

Additional critical packages included the databases Redis and MySQL which stored the instrument state and measurement results respectively. Images were passed between servers at high speeds using the Durham Adaptive Optics (DAO) (Townson et al., 2022) shared memory architecture. DAO is a high-performance RTC software designed for the ELT-HARMONI instrument AO system. The software also utilised ZeroMQ sockets for streaming video to clients connecting to the instrument. The handling of image data is illustrated in figure 5.12. The advantages of this implementation were relative simplicity due to little interaction aside for one-way communication of each server with the supervisor. The instrument latest state stored in Redis enabled all processes to access that information simultaneously.

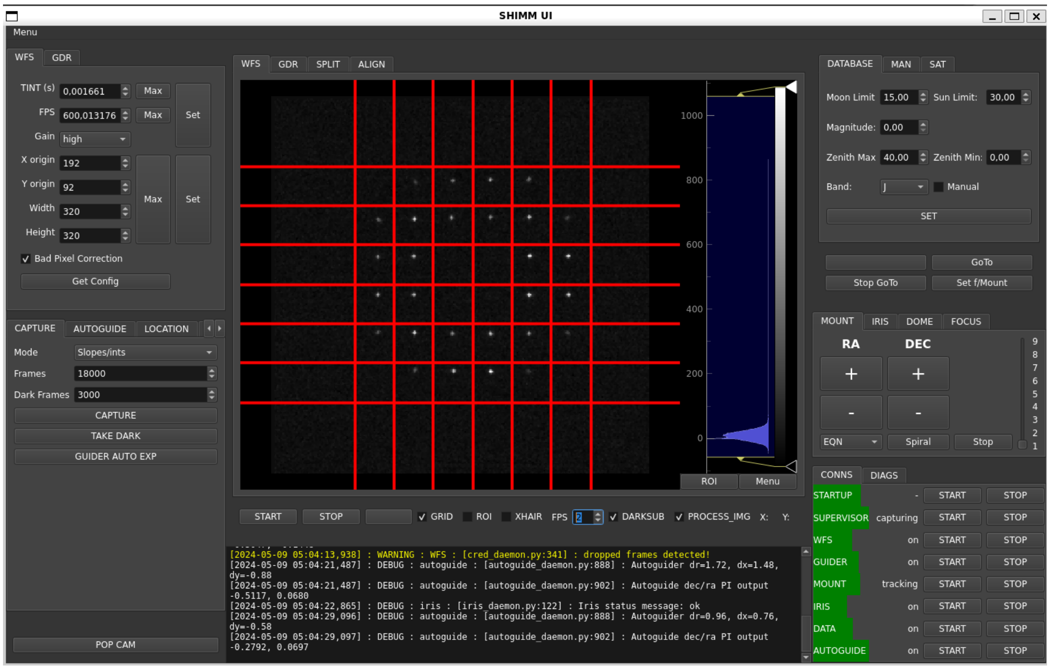

TINT (s) 0,001661
FPS 600,013176
Gain high
X origin 192
Y origin 92
Width 320
Height 320
☑ Bad Pixel Correction

Mode Slopes/ints
Frames 18000
Dark Frames 3000

☑ GRID ☐ ROI ☐ XHAIR FPS 2 ☑ DARKSUB ☑ PROCESS_IMG

Moon Limit 15,00 Sun Limit: 30,00
Magnitude: 0,00
Zenith Max 40,00 Zenith Min: 0,00
Band: J ☐ Manual

EQN

STARTUP -
SUPERVISOR capturing
WFS on
GUIDER on
MOUNT tracking
IRIS on
DATA on
AUTOGUIDE on

```
[2024-05-09 05:04:13,938] : WARNING : WFS : [cred_daemon.py:341] : dropped frames detected!
[2024-05-09 05:04:21,487] : DEBUG : autoguide : [autoguide_daemon.py:888] : Autoguider dr=1.72, dx=1.48,
dy=-0.88
[2024-05-09 05:04:21,487] : DEBUG : autoguide : [autoguide_daemon.py:902] : Autoguide dec/ra PI output
-0.5117, 0.0680
[2024-05-09 05:04:22,865] : DEBUG : iris : [iris_daemon.py:122] : Iris status message: ok
[2024-05-09 05:04:29,096] : DEBUG : autoguide : [autoguide_daemon.py:888] : Autoguider dr=0.96, dx=0.76,
dy=-0.58
[2024-05-09 05:04:29,097] : DEBUG : autoguide : [autoguide_daemon.py:902] : Autoguide dec/ra PI output
-0.2792, 0.0697
```

Figure 5.13: A screenshot of the instrument control GUI during an experiment.

5.5.2 Instrument GUI

The GUI for the instrument was written using the python PySide6 package, the official python implementation of Qt6. The client GUI for controlling the instrument is shown in figure 5.13. In the centre is a real-time embedded video feed displaying both the wavefront sensor camera or the wide-field acquisition camera implemented in pyqtgraph. Around the edge of the video feed there are a number of widgets that control target selection, mount driving, configuration of acquisition and autoguiding parameters, a real-time readout of the current RA-DEC coordinates of the mount and other important telemetry. The GUI directly interfaced with the supervisor component of the RTC to configure and control the experiment.

5.6 Operation

In order to produce accurate and automated measurements, there are a number of alignment and calibration steps that must be followed. The instrument demands accurate telescope pointing to acquire targets in the wide-field finderscope during the daytime, a well-calibrated autoguider to retain targets in the field of view and fight tracking errors, and a precise optical alignment to avoid systematic error due to conjugation height and image scale errors. This section will describe both these calibration steps, and the flow-control logic used to implement automated observations.

5.6.1 Alignment and Calibrations

Assuming first that the lenses have been placed in the correct positions as described in section 5.2.3, a number of additional alignments and calibrations are still required. Before any other steps, it is essential to build a dark frame to subtract the significant dark current, fixed pattern noise and hot pixels on the InGaAs detector. This was done by closing the iris to ensure that no light could enter the optics, then taking 5 seconds of frames (3000 at 600 Hz) which were averaged to build the dark frame. Furthermore due to the 24-hour nature of the experiment, significant temperature fluctuations regularly occurred throughout an observation. Regular updates of the dark frame were therefore key to maintaining accurate photometry.

The physical steps to prepare the experiment were then as follows:

- Firstly a star was acquired in the wavefront sensor and brought roughly into focus. The spot pattern was typically rotated at some angle to the detector pixels due to an offset angle between the detector and the microlens array. The rotation stage, or a rotation of the full optical assembly in the new design, was used to align the spot pattern with the $x - y$ axes of the detector.

- The spot pattern would then require focusing by adjusting the telescope primary mirror offset until spots are in the centre of the indicated sub-aperture grid.
- Lenslets were unlikely to be well aligned with the beam from the telescope. It was critical therefore to adjust the $x - y$ alignment of the MLA such that an integer number of lenslets were across the beam. The degree of vignetting in each sub-aperture could be used as a guide and the reference values are shown in figure 5.2.
- Finally, the wide-field finderscope was co-aligned with the wavefront sensor as closely as possible, and an image-scale calibration as in 5.2.3 was carried out.

The next stage of instrument alignment concerned the mount itself and the autoguiding software. To align the mount, the user must follow a full pointing model calibration as described in detail in Celestron (2021). To summarise, this involved asking the mount to point at several stars across the entire visible sky, then manually bringing the star into the centre of the field-of-view of the wavefront sensor so that the mount could build a pointing model. It was necessary for the pointing model to be accurate to within half of the field of view of the finderscope to ensure that a star was always visible on the finder and could then be guided onto the SHWFS. A computer-aided polar alignment was also possible through the CGX-L mount software which was usually carried out to improve the tracking and ensure less strain on the autoguider.

Finally, there were two major calibrations necessary for the autoguider to function: a measurement of the rotation of the RA-DEC coordinate axes compared to the camera $x - y$ axes, and setting the reference point for the autoguider to bring the object back into the instrument FOV. These were made both on the wavefront sensor, where the reference positions were set in each sub-aperture, and on the wide-field finder. The first calibration allowed $x - y$ offsets in pixels to be converted to an offset in RA/DEC through a simple rotation matrix, which was then fed into the autoguider which moved the mount to return the spots to their reference positions. Critically on the equatorial mount, the RA axis was mirrored for the eastern pierside position, equivalent to tracking falling targets.

5.6.2 Target Acquisition

Targets were acquired by querying current stars from the bright star catalogue that conformed to the specifications of table 5.2. The star with the lowest magnitude was almost always chosen unless its observation time was less than 30 min. Target observation time could be cut short by the meridian flip - the telescope could only track 20° after the meridian before locking. After a suitable target was selected, a slew command was issued to the mount and the system waited until the mount had stopped moving. The pointing model accuracy on this mount was not sufficient to acquire the target on the wavefront sensor immediately, however stars were always within the wide-field finder FOV. A reference position corresponding to the SHWFS field of view on the wide-field scope was used to then guide the star onto the wavefront sensor. In practice the system is limited, potentially by mirror flop in the telescope primary mirror or by flexing in the optics, such that the alignment between the finderscope and SHWFS would change depending on pointing angle. A spiral search was therefore implemented to automatically guide the star into the wavefront sensor which had a small FOV. Upon detection of a star in the SHWFS, the star was guided into the centre of the sub-apertures and acquisition could begin. This process is shown in figure 5.14 which details the flow control diagram of the automated data acquisition routine of the instrument.

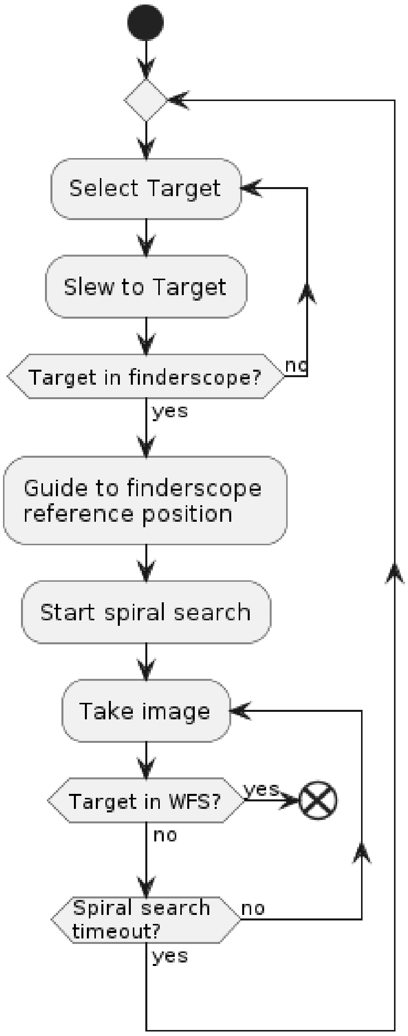

Figure 5.14: Flow control diagram describing the automated target acquisition process of the SHIMM.

5.6.3 Auto-guiding

Due to the flexing between the wide-field finder and SHWFS as pointing angle evolved, autoguiding was implemented directly on the SHWFS spot pattern. The autoguiding server took images from the SHWFS shared memory at 60 Hz, using 5 s (300 frames) of averaging for a single autoguide event to average out wind-shake effects. The image processing algorithm could then be applied to this small number of frames to generate a time-sequence of centroid positions which were averaged to determine the current spot pattern displacement. A PID algorithm was applied to

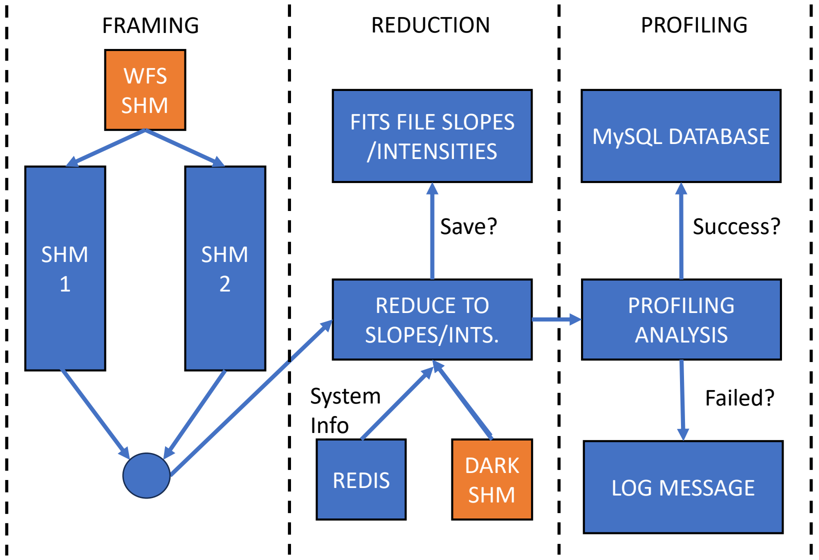

Figure 5.15: A simplified control diagram for the data server. The figure shows the three sub-processes and the overall data pipeline. The orange boxes signify the DAO shared memory objects.

give the RA/DEC motor movements required to maintain the spots close to their reference positions.

5.6.4 Data acquisition

The data acquisition ran alongside the autoguider and consisted of three separate threads: framing, reducing images to slopes and intensities and analysing processed images. Due to python's global interpreter lock, these process had to be implemented with sub-processes using the multiprocessing library in order to protect the acquisition thread resources from being drained by the other two threads. To investigate temporal parameters such as coherence time and perform exposure time corrections, it was critical that the acquisition rate remained fixed so that each frame can be accurately time stamped. To ensure that there was no downtime between measurements, a method of interleaved acquisition was implemented such that a new measurement could start while the previous measurement was being processed. This required two large numpy arrays to be held in multiprocessing shared memory and protected through thread locks. In order to not exceed the 32GB of memory on the system, the maximum array size was set to 18,000 images (or 30 s of data at 600 Hz) in the signed 16-bit format used by the camera. Arrays were not saved to disk due to their large size which would lower the speed of the acquisition software and increase downtime between measurements considerably. A diagram of the components and analysis steps in the data server is shown in figure 5.15.

5.6.5 Outputs

Results could be stored either as FITS files of raw SHWFS images, of measured Shack-Hartmann slopes and intensities, or simply turbulence parameters and the vertical profile saved to a MySQL database. Saving of raw Shack-Hartmann images was only used for debugging due to prohibitive size of the arrays for high-speed data. FITS objects were created in memory as a convenient package for transferring the arrays of slopes and intensities between the data reduction sub-process and the profiling sub-process. These could optionally be saved to allow for re-analysis of the data with new algorithms. If results were processed successfully they were entered into the MySQL database which ran locally on the SHIMM control PC. This provided a convenient central database for the client PC to read data in and display outputs in real time.

5.7 Data quality control

Given that the reconstruction process was very sensitive to noise in measurements, it was critical to assess the quality of data at all stages of the analysis pipeline to ensure outputs were accurate. Some basic controls were made in setting up experiments and at early stages in the pipeline:

- Ensure that the C-RED3 bad pixel corrections were on and that the camera was in high gain mode which gave the lowest readout noise (Gach et al., 2020).

- Dark frames were taken automatically every 10 min throughout measurements and the target acquisition process as the sensor temperature experienced large fluctuations over 24-hour periods.
- The iris aperture must be set correctly such that there were minimal overlaps of images of the sky background from adjacent sub-apertures. These could cause bright spots where multiple backgrounds were overlaid and affect the image analysis.
- The telescope was checked for condensation on the corrector plate, fitting a dew shield at night where necessary.

5.7.1 Image processing

Quality control checks were implemented at the image processing stage. They primarily dealt with early detection of failed centroids and checking that subsequent measurements were not affected.

- Values where centroiding failed, or the centroid was detected too close to the edge of a sub-aperture, were masked with zeros. This mitigated cases where the centroid drifted too close to the edge of a sub-aperture and the spot was vignetted, or where the spot was not visible above the background, or when the intensity after thresholding was negative which could happen in the case of a dark-subtracted image. This process would however also mask deep intensity fades due to scintillation in extreme conditions which would bias the measurements towards a lower scintillation index.
- If this occurred in more than 20% of frames, an error was raised and the measurement was dumped.

- Measurements of intensity were also set to zero for these cases. These frames were also excluded from any sub-aperture photometry calculations.

5.7.2 Profiling algorithm

The vast majority of data filtering took place in the processing algorithm after the measurements had been reduced.

- The SNR of the measurements in each sub-aperture was checked using the photometry measurements obtained in the image processing stage, and the average intensities of the spots used to give the shot signal. If this was found to be below 15 in any sub-apertures then the data was rejected.
- A measurement of intensity in a single frame that was less than 1% of the average value was judged to be more likely due to effects such as wind shaking the spot out of the aperture than due to a deep fade from turbulence and so it would be masked.
- After this stage, if 20% of the frames had a masked value then the data was rejected. If not then masked arrays were used so that subsequent calculations did not use the poor data. These data points where therefore omitted from calculations of the defocus coefficient and the covariances.

5.8 Conclusion

This chapter presented the optical, mechanical and software design of the SHIMM instrument. The combination of off-the-shelf optical components given in table 5.1 was shown to produce a 6×6 sub-aperture SHWFS with 20 active focal spots that were Nyquist sampled by the detector pixels. Using this optical design the transmission spectrum and central wavelength were estimated. Using analysis from the previous section on the minimum desired SNR and the restrictions on target attributes such as zenith angle, a target availability analysis was conducted for a northern-hemisphere site and indicated that there would always be targets available. Finally an overall description of the SHIMM system was made starting with necessary alignments and calibrations and ending with a detailed discussion of the software implementation; showing how fast sampling times are achieved using the DAO shared memory architecture, the automatic target acquisition logic, and the quality control and observation procedures.

Chapter 6

On-sky measurements and comparison of next-generation instrumentation

6.1 Introduction

The SHIMM is one of the latest generation of turbulence monitoring instrumentation including instruments such as RINGSS, FASS and Profiler of the Moon Limb (PML) (Aristidi et al., 2019), that are being developed to compliment, improve upon and eventually replace the existing dedicated small-telescope turbulence monitoring instruments, the MASS and DIMM. These two instruments are limited by the use of outdated detectors, custom-manufactured equipment and, in the case of the MASS, a noted discrepancy in measurements of OT profiles compared to the high-resolution SCIDAR technique (Masciadri et al., 2014; Lombardi and Sarazin, 2016). There is therefore significant motivation to develop new instrumentation based on modern technologies for deployment alongside the upcoming class of 20-40 m ELTs. There is also increasing demand from optical communications research for portable instruments to characterise turbulence conditions at potential OGS sites (Griffiths et al., 2023a; Birch et al., 2023b; Biasi et al., 2023), especially 24-

hour conditions for which there is little available data due to a lack of instruments adapted for both day and night measurements. It is critical that novel turbulence monitoring techniques undergo extensive testing and validation alongside existing instrumentation in order to understand their strengths and weaknesses and where techniques can be improved upon. This process was vital for the DIMM between its emergence in the 80s and the present day and led to many improvements made to the analysis in works such as Tokovinin (2002b). The aim of this chapter is to firstly show experimental results of a major turbulence monitoring campaign at Paranal observatory involving a number of established and novel turbulence profilers, of which the SHIMM was one. The instruments will be cross-validated and results analysed to identify how state-of-the-art turbulence monitors compare to the established instruments at the Paranal site. Secondly, extensive results from the SHIMM operating in an urban location of interest to FSOC will be shown, with a focus on how conditions differ between the night and day. In the interest of facilitating easy comparisons, unless stated otherwise all integrated turbulence parameter measurements are reported at zenith and for a wavelength of 500 nm. Furthermore, all turbulence profiles are given as a function of vertical height.

6.2 A turbulence profiling comparison at Paranal

Multi-instrument campaigns have been hosted a number of times at the European Southern Observatory (ESO) Paranal site, including for example Dali Ali et al. (2010) and Osborn et al. (2018). This section details the results from the most recent campaign at Paranal, in which three turbulence profiling instruments based on portable telescopes: the SHIMM (Griffiths et al., 2023b) (also called the 24hSHIMM), FASS (Guesalaga et al., 2021) and RINGSS (Tokovinin, 2021) were compared with permanently installed OT profiling instruments at the site. The primary motivation being to facilitate the development and characterisation of these next-generation instruments against existing techniques. The three instruments were co-located on the northernmost part of the observatory for 6 nights starting on the 27th of February, with the final night of observation on the 5th of March 2023. The ESO MASS-DIMM (Chiozzi et al., 2016) was operating throughout all nights of observation whereas the stereo-SCIDAR (Osborn et al., 2018) was operated from the 28th to the 5th only. As a part of the VLT atmospheric site monitoring package, measurements of local meteorological parameters were available for additional analysis. The descriptions and operational principles of all instruments other than the SHIMM are discussed in section 2.5. It should also be noted that the SHIMM at Paranal used the same techniques described in this work in chapter 3, implemented instead using a CMOS sensor due to being unable to source an InGaAs detector in Chile for the campaign. The implications of this were a lower central wavelength of 695 mm, increased noise in daytime optical turbulence measurements due to speckling in the PSF in strong turbulence conditions, but a gain in sensitivity during very weak turbulence due to greater centroid motion. Data were also collected at a slower sampling rate of 100 Hz, limiting the sensitivity of coherence time measurements when the effective wind velocity was greater than approximately $15\,\mathrm{m\,s^{-1}}$.

6.2.1 Campaign details

The location of each instrument on the Paranal observatory platform is shown in figure 6.1. The SHIMM and RINGSS were mounted on concrete pillars adjacent to the 1998 DIMM tower within 2 m of one-another. The FASS was mounted on a tripod slightly further away, between the old-DIMM tower and SLODAR cabin. The SHIMM was mounted approximately 2 m off of the ground, the RINGSS and FASS were at about 1.5 m. Wind breaks were set up along the northern fence next to the instruments.

The local environments for the S-SCIDAR and MASS-DIMM were therefore significantly different; they were both much further away from any large buildings and more elevated from the ground. The MASS-DIMM was on a 7 m tower and the S-SCIDAR was mounted on VLTI auxiliary telescope two; the alt-az altitude

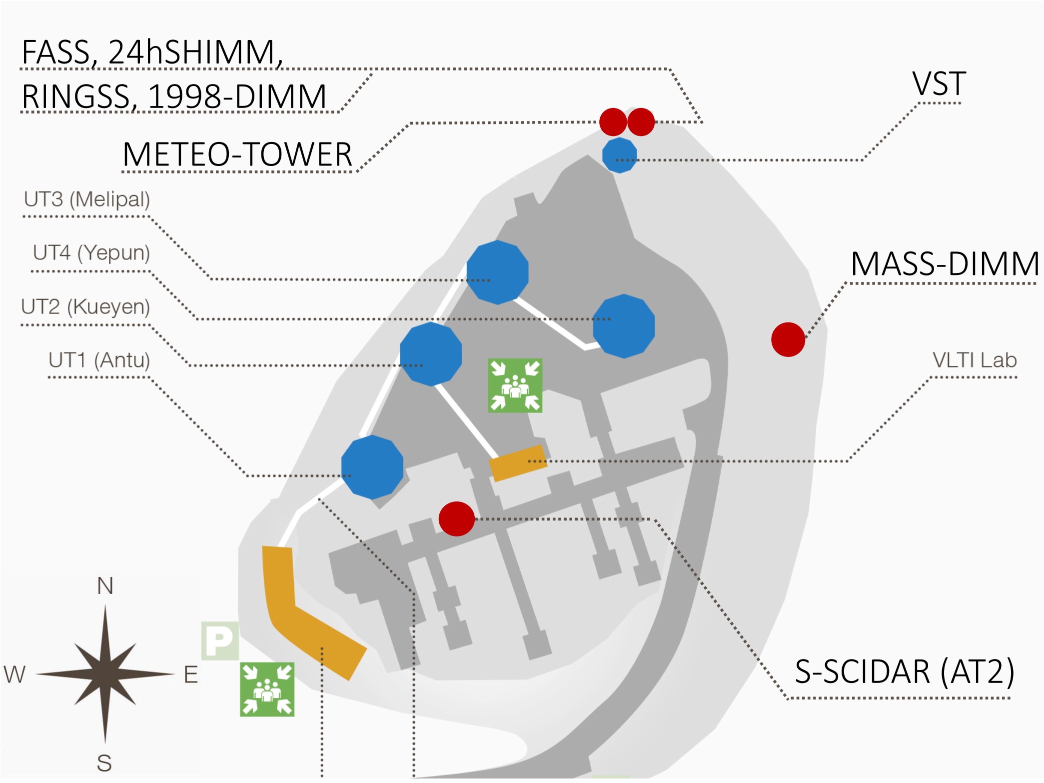

Figure 6.1: Location of turbulence monitoring instrumentation for the campaign. Instruments relevant to this study are indicated by red circles. Original image credit: ESO.

axis of which is 5 m above surface (Koehler and Flebus, 2000). We therefore expect poorer agreement in the seeing between these instruments and the monitors located near the VLT Survey Telescope (VST), as local turbulence conditions were likely to differ significantly.

The list of targets for the RINGSS was shared at the beginning of the experiment and efforts were made to synchronise target stars where possible between the visiting turbulence monitors. The MASS-DIMM and S-SCIDAR however were using separate target lists.

The overall results for this campaign are laid out below. This includes both direct comparison of integrated parameter measurements between the different instruments, and a comparison of optical turbulence profiles with the high-resolution

S-SCIDAR. A focus is primarily made on comparison of the developmental instruments SHIMM, RINGSS with the well-characterised and permanently installed S-SCIDAR and MASS-DIMM. However all instruments have been compared where appropriate. The comparison between SHIMM and RINGSS is of interest as the two instruments were co-located, observing similar targets and so are much more likely to agree. The agreement of the S-SCIDAR and MASS-DIMM is also of interest to compare to long-term monitoring results and previous studies.

To generate comparison plots, for the instrument on the x-axis, each measurement has been directly plotted against the nearest measurement from the instrument on the y-axis within a maximum time difference of two minutes. If a corresponding measurement could not be found within two minutes, the data point has been excluded from the plot to minimise the effects of temporal evolution of the turbulence on the comparison. This two minute interval was chosen to match the integration time used by the S-SCIDAR as it was the longest of all the instruments. As the algorithm finds the nearest measurement within the search window and the other instruments all have a cadence of a minute or less, reducing the interval to one minute, for example, was observed to produce almost identical statistical comparison parameters.

In each comparison plot, a white dashed line represents the line of perfect agreement between the instruments, and the Pearson correlation coefficient, r, bias, B, unbiased root mean square error, RMSE, and mean ratio, MR, of each data set is reported in the top-left of the graph. Mathematical definitions of the latter three parameters may be found in appendix A. These comparison parameters are additionally summarised for each figure in table 6.2. The colour gradient indicates the density of measurements at each point in the graph with black the lowest and pale yellow the highest. The median values from these findings will also be compared where useful to results from long-term studies on seeing conditions at Paranal with Butterley (2021) reporting the latest S-SCIDAR results and Otarola (2021) the results from the MASS and DIMM. These results can be found in table 6.1.

Table 6.1: Median values of parameters obtained during this campaign, marked in the columns as “2023”, from all instruments are compared with long-term site monitoring results of Otarola (2021); Butterley (2021) with the column labels “long-term”. There are some blank entries which correspond to unavailable data - either because the instrument cannot measure the parameter or there is no source for long-term data. The median values for the SHIMM are calculated excluding data taken during the daytime.

	N Profiles	$\varepsilon_0('')$		$\varepsilon_{0,f}('')$		$\theta_0('')$		τ_0 (ms)	
Instrument	2023	Long-term	2023	Long-term	2023	Long-term	2023	Long-term	2023
DIMM	2696	0.71	0.75	-	-	-	-	-	-
MASS-DIMM	2477	-	0.79	0.41	0.40	1.98	2.53	6.14	6.3
S-SCIDAR	611	0.72	0.76	0.46	0.51	2.03	2.62	3.61	5.8
RINGSS	5387	-	1.10	-	0.58		2.46	-	5.8
SHIMM	1942	-	0.89	-	-	-	2.35	-	6.4

Table 6.2: Summary of statistical comparison parameters all graphs.

X - axis	Y - axis	r	RMSE	B	MR
Seeing, ε_0			($''$)	($''$)	
S-SCIDAR	RINGSS	0.70	0.27	0.40	1.59
DIMM	RINGSS	0.76	0.28	0.34	1.46
S-SCIDAR	SHIMM	0.76	0.17	0.16	1.25
DIMM	SHIMM	0.80	0.18	0.11	1.19
S-SCIDAR	DIMM	0.83	0.15	0.02	1.04
SHIMM	RINGSS	0.83	0.28	0.24	1.25
Free atmosphere seeing, $\varepsilon_{0,f}$			($''$)	($''$)	
S-SCIDAR	RINGSS	0.86	0.21	0.14	1.23
MASS-DIMM	RINGSS	0.85	0.22	0.14	1.36
S-SCIDAR	MASS-DIMM	0.80	0.17	-0.03	0.93
Isoplanatic angle, θ_0			($''$)	($''$)	
S-SCIDAR	RINGSS	0.35	0.67	-0.17	0.97
MASS-DIMM	RINGSS	0.40	0.59	-0.08	1.00
S-SCIDAR	SHIMM	0.40	0.67	-0.32	0.91
MASS-DIMM	SHIMM	0.33	0.65	-0.18	0.96
S-SCIDAR	MASS-DIMM	0.30	0.72	-0.19	0.97
SHIMM	RINGSS	0.54	0.53	0.11	1.08
Coherence time, τ_0			(ms)	(ms)	
S-SCIDAR	RINGSS	0.75	1.94	-0.05	1.00
MASS-DIMM	RINGSS	0.69	3.69	-0.82	0.96
S-SCIDAR	SHIMM	0.68	2.15	0.21	1.05
MASS-DIMM	SHIMM	0.77	2.46	0.14	1.05
S-SCIDAR	MASS-DIMM	0.70	2.10	0.25	1.05
SHIMM	RINGSS	0.80	2.21	-0.53	0.97

Finally, the distribution and temporal sequences of $C_n^2(h)\,\mathrm{d}h$ profiles measured by the instruments will be directly compared with the S-SCIDAR through a binning process to investigate accuracy of OT profile characterisation, and the first results from the SHIMM of 24-hour continuous monitoring of OT at Paranal are presented in full.

6.2.2 Seeing

Accurate measurement of the astronomical seeing is the most fundamental requirement of an optical turbulence monitor as it quantifies the integrated turbulence strength of the atmosphere and directly relates this to the degree of image distortion. Seeing is dynamic, can change rapidly and is highly dependant on location and pointing direction (Tokovinin, 2023) which leads to discrepancies between instruments, even for well-synchronised measurements. Median seeing measurements in table 6.1 indicate that the two instruments located in the northern end of the site, near to the VST and installed at a lower height above ground, are measuring substantially stronger seeing that the MASS-DIMM and S-SCIDAR. This is most likely due to local turbulence effects. There is however a very strong agreement between the DIMM and S-SCIDAR measurements, and a mean ratio close to 1, despite their separation on the site — but noting their similar height above the ground and isolated locations this is not surprising.

It is known that the local seeing at the 1998-DIMM tower is slightly stronger than the current 2016-MASS-DIMM. The median seeing calculated from several years of measurements with the 1998-DIMM between 2010-01-01 and 2015-05-22 was found to be $0.98''$ compared to the 2016-DIMM long term seeing of $0.71''$. This supports a location-based argument for some of the discrepancy between the visiting and the ESO instruments. Previous campaigns using the Generalised Seeing Monitor at the same location have found seeing values of $0.88''$ (Martin et al., 2000) and $1.07''$ (Dali Ali et al., 2010). Additionally, high-resolution profiling of the surface layer carried out by Butterley et al. (2020b) using the surface-layer SLODAR identifies an exponentially decaying turbulence strength with altitude — hence we also expect the higher elevation of the MASS-DIMM and S-SCIDAR to result in lower seeing.

Individual comparisons of seeing measured by each instrument are displayed in figure 6.2. It is extremely encouraging that all seeing measurements display strong correlation with the minimum of $r = 0.70$ for the RINGSS compared with the S-SCIDAR. As expected, due to co-location and overlapping targets, the SHIMM and RINGSS display a very strong correlation of 0.83, however there is a significant bias between the two despite their proximity. A number of factors may contribute to this, including the RINGSS corrections for finite exposure time and partial saturation of scintillation - conditions which would lead to underestimates of fast-moving and high altitude turbulent layers on the SHIMM - there is a also a small

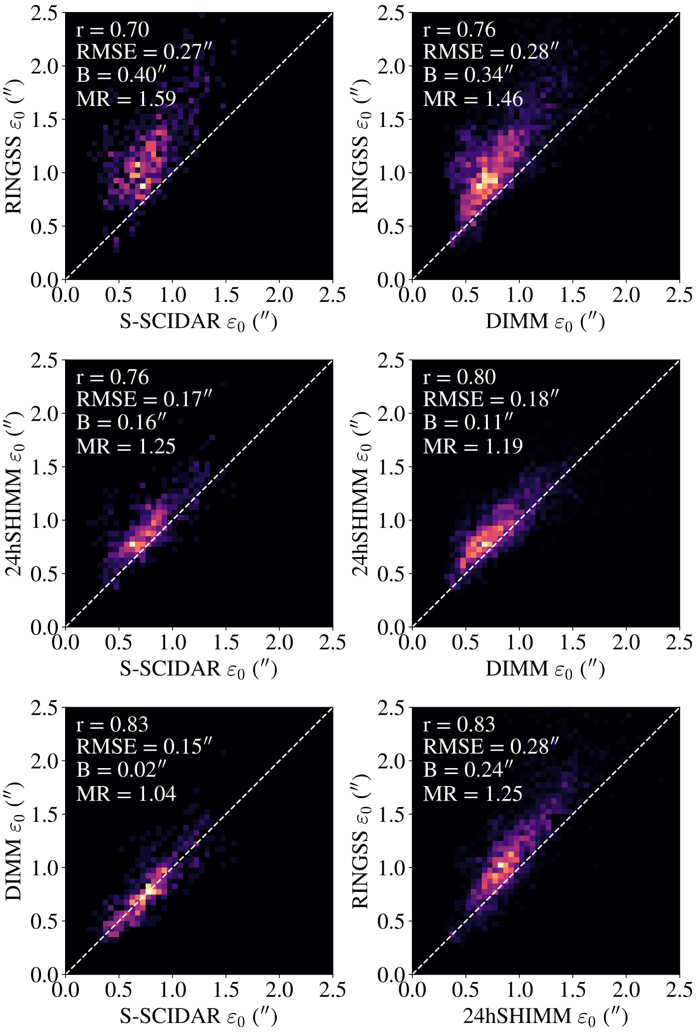

Figure 6.2: Comparison of contemporaneous seeing measurements during the campaign from the DIMM, S-SCIDAR, SHIMM and RINGSS.

height offset between the two with the RINGSS being closer to the ground which could lead to slightly stronger turbulence above the telescope pupil. The correlation between the DIMM and S-SCIDAR is equally strong but with far less bias - the results are also consistent with the long term monitoring as seen in table 6.1.

6.2.3 Free atmosphere seeing

The free atmosphere seeing, $\varepsilon_{0,f}$ is calculated as the integrated seeing of all turbulent layers with an altitude of 500 m or greater for the MASS, RINGSS and

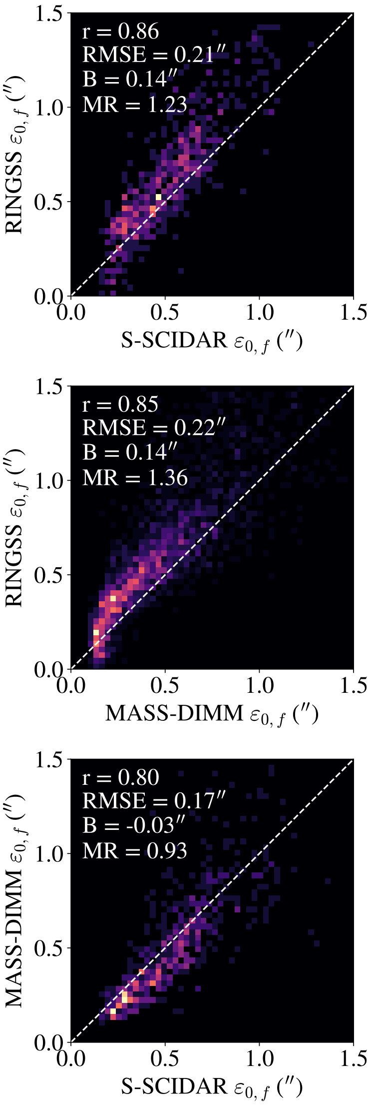

Figure 6.3: Comparison of contemporaneous free atmosphere seeing measurements during the campaign from the MASS-DIMM, S-SCIDAR, and RINGSS.

S-SCIDAR. The SHIMM is limited by a large sub-aperture size of 4.7 cm and cannot sample the highest frequency scintillation fluctuations produced by low-altitude turbulence. This is due to height scaling of the characteristic size of scintillation speckles - given by the radius of the first Fresnel zone, $r \approx \sqrt{\lambda z}$. It therefore lacks the sensitivity required to reconstruct a layer at 500 m, so a direct comparison with the other instruments is not possible and it has been excluded. Figure 6.3 details the measurements obtained with the three other instruments.

6.2.4 Isoplanatic angle

Figure 6.4 displays the comparisons of isoplanatic angle measured by all instruments. Unlike measurements of the seeing, it is observed that there is less correlation between all instruments. However, the variation of isoplanatic angle during the campaign was small. The strongest correlation, 0.54, is found between SHIMM and RINGSS which observed same targets, while other profilers sampled different turbulent volumes. The $h^{5/3}$ scaling in equation 2.53 implies that this parameter is highly sensitive to turbulence in the upper atmosphere. Therefore an accurate characterisation will require sensitivity to high-altitude turbulence. The SHIMM, RINGSS and MASS are limited in this regard by their response functions for the highest altitude layer which are several kilometres wide. The turbulence distributed over this layer will be averaged and reported at that height, leading to a reduction in accuracy. When taking optical propagation into account for observing at lower zenith angles, saturation of scintillation produced by the highest-altitude layers is an additional source of error for monitors based on weak-scintillation theory. The exception in this experiment being the RINGSS and MASS which implement a correction process. This combination of factors is likely to explain the smaller correlation observed in measurements from the four instruments, while the median values agree fairly closely within a range of 2.35 to 2.62 arcseconds.

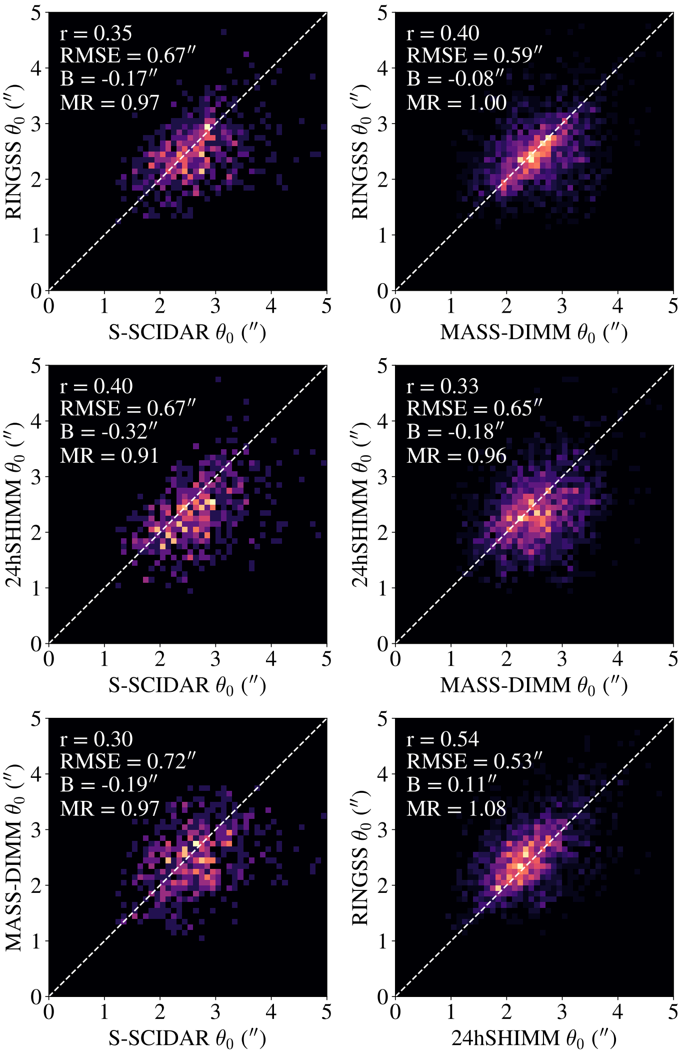

Figure 6.4: Comparison of contemporaneous isoplanatic angle measurements during the campaign by the MASS-DIMM, S-SCIDAR, SHIMM and RINGSS.

6.2.5 Coherence time

Knowledge of the coherence time is essential for AO as it defines the minimum bandwidth of the system. The instruments in this study employ a variety of strategies to measure the coherence time. The S-SCIDAR analyses the spatio-temporal cross-correlations of the scintillation measured in the pupil. Peaks that match atmospheric layers translate across the auto-covariance map with each successive time offset due to translation of the turbulent layers with wind. The direction and speed of each of the layers is recorded and the mean wind speed calculated from equation 2.55. The S-SCIDAR is only able to directly estimate the wind speed of the strongest layers. Weak layers with no detected wind speed are assigned a value through interpolation of the measured wind speed profile. The SHIMM takes a different approach, utilising the FADE method (Tokovinin et al., 2008), which involves fitting response functions, determined by layer wind speeds and $C_n^2(h)\,\mathrm{d}h$, to the measured temporal structure function of the Zernike defocus coefficient of the atmospheric wavefront distortions. The SHIMM analysis differs slightly from the FADE instrument as wavefronts are reconstructed by the Shack-Hartmann yielding direct measurements of the Zernike defocus term, and only layer wind speeds need to be fitted. As the SHIMM sampling rate was limited by the detector and software architecture to 100Hz for this experiment, it was necessary to exclude 362 measurements that had a $\overline{V}_{5/3} > 15\,\mathrm{m\,s^{-1}}$ as the defocus structure function curve could not be sampled with a sufficient temporal resolution to fit a wind speed profile. The MASS-DIMM and RINGSS utilise the method described in Kornilov (2011a) of including a wind shear component in the weighting functions, continuous exposures without gaps, and a fitting process to estimate the second moment of the wind $\overline{V}_2$ with the approximation of $\overline{V}_2 \approx 1.1\overline{V}_{5/3}$ found by Kellerer and Tokovinin (2007) enabling an estimate of the coherence time.

Figure 6.5 displays comparisons of coherence time measurements for the four instruments. The RINGSS and MASS use the same method of calculating coherence time and agree strongly with little bias. The two instruments also agree well with the S-SCIDAR, again with little bias. The SHIMM shows good correlation with all instruments too. The bias however is small but positive with respect to the S-SCIDAR and MASS-DIMM. Lower elevation and imaging through more of the surface layer should lead to a negative bias, suggesting that the instrument may be overestimating coherence time which could be a result of the low frame rate. Finally, the lower correlation of some instruments with the S-SCIDAR may result from the fact that S-SCIDAR measures wind direction and corrects line-of-sight

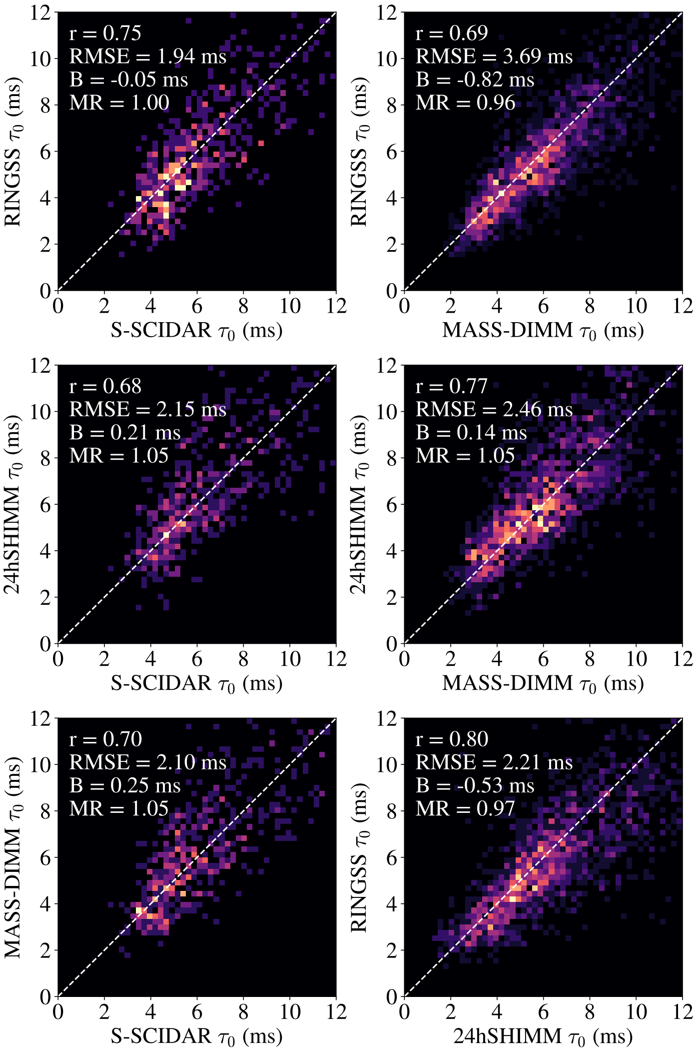

Figure 6.5: Comparison of contemporaneous measurements of the atmospheric turbulence coherence time by the MASS-DIMM, S-SCIDAR, SHIMM and RINGSS.

wind speed measurements to the wind speed parallel to the ground, which other instruments cannot do.

6.2.6 Influence of wind direction

Previous studies have observed that wake produced downwind of large telescope structures can have a significant effect on seeing conditions (Sarazin et al., 1990). Additionally, seeing at the 1998-DIMM tower has historically been stronger than that observed by the UTs for north-easterly and south-easterly winds (Sarazin et al., 2008). A later study by Lombardi et al. (2010) related this phenomenon to an increase in the strength of the surface layer. We therefore expect wind direction to influence the agreement between instruments in this campaign. The wind rose, figure 6.6, shows the distribution of wind speeds and directions measured 30 m above the ground by the meteo-tower between sunset and sunrise for all six nights of the campaign. The 30 m measurement is used over the 10 m measurement to minimise bias introduced by the Unit Telescopes (UTs) to the South and the VST to the SSW. The radial extent of the bars represents the fraction of the data with a given wind direction and it suggests, similar to previous studies such as Lombardi et al. (2009), that it is mainly from the NNE.

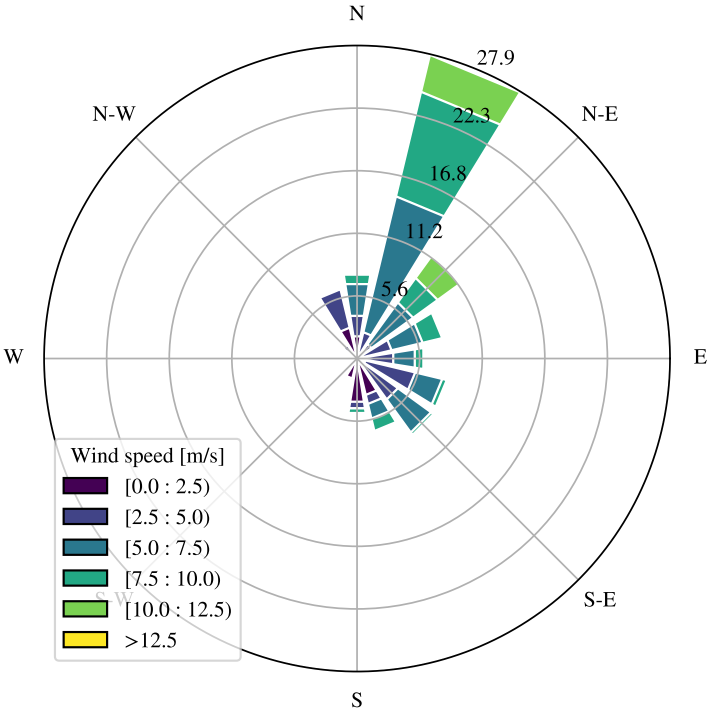

Figure 6.6: A wind rose displaying the distribution of wind speeds and directions measured 30 m above the ground by the Paranal meteo-tower for the six nights of the campaign.

Figure 6.7 shows how the bias between pairs of instruments changes as a function of wind direction for eight directional bins. In addition, the error bars indicate the bias-corrected RMSE of the comparisons for each wind direction. Due to insufficient data for some wind directions, the correlation is not plotted. Additionally, there were no S-SCIDAR data points between South and West and insufficient data for all instruments for the West bin. These points have therefore been omitted. Seeing measurements during the campaign appear to be strongly influenced by wind direction. For instrument pairs other than the S-SCIDAR and MASS-DIMM, the RMSE of instrument comparisons is larger for northerly winds. The RINGSS bias appears sensitive to the wind direction with the largest bias corresponding to north-westerly winds, but the SHIMM does not follow the same pattern - only seeing a larger bias compared to the MASS-DIMM towards the North-West. However there are few data points for this bin. This figure does not take into account instrument pointing direction, which can also lead to discrepancy in measurements. As this sample of six nights is relatively small, the influence of pointing direction was investigated instead through analysing the median and standard deviation of seeing measured by the 2016-DIMM for all data in the ESO archive. This analysis showed a clear increase in median seeing for north-easterly and south-easterly winds for all pointing angles. Features strongly dependent on pointing angle included: larger variability at low elevation angles when the DIMM points SE and wind blows from the W and SW, and for the DIMM pointing SW while the wind blows from the North. The larger spread of data and bias for northerly winds experienced by the SHIMM and RINGSS may be related to their proximity to the edge of the platform, as shown in figure 6.1, as air from the ground level will be driven up the mountain and mix with cooler air at the platform. By contrast, wind from the South will traverse the platform before reaching the SHIMM and RINGSS. The S-SCIDAR vs MASS-DIMM seeing comparison has no identifiable dependence on wind direction which is expected as both instruments are raised above the ground and located away from the platform edges and buildings.

For the free atmosphere seeing and isoplanatic angle, dependence on wind direction at 30 m seems unlikely as both parameters are insensitive to ground layer turbulence. In reality, non-Kolmogorov turbulence in the surface layer which may

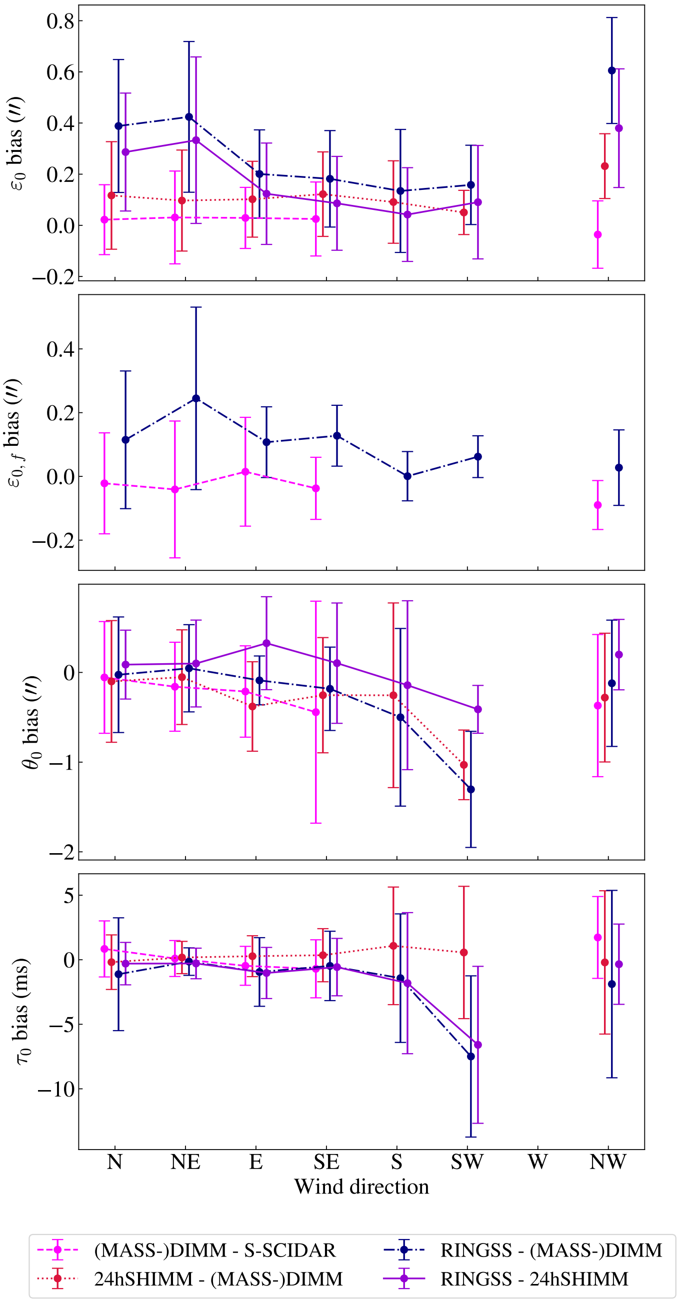

Figure 6.7: A plot showing the bias of measurements for all four integrated turbulence parameters, and the RMSE indicated by the error bars, as a function of wind direction for key pairs of instruments compared in this study. For the seeing, only DIMM data is used, but for other parameters the MASS-DIMM results use the same line style. The legend indicates the Y - X instrument pair for which the bias and RMSE have been plotted.

arise from interaction of wind with buildings or heat sources can “confuse” turbulence monitoring instruments that expect a specific power spectrum (typically Von Kármán or Kolmogorov), thus leading to inaccuracies in the characterisation of the turbulence profile that may depend on wind direction. Such effects are also encountered at low wind speeds and have been identified at the site by the SLODAR (Butterley et al., 2020b). Figure 6.6 shows that for southerly winds, a wind speed of less than $3\,\mathrm{m\,s^{-1}}$ is proportionally more frequent. For the coherence time, which is also dependent on the vertical wind speed profile, the biases are small relative to the spread of the data, except for the SW which may result from a small number of samples. The wind direction does not seem to have a significant influence on the bias or RMSE of these comparisons, however there is a trend towards a larger negative bias for most instrument comparisons in the NE to SW section of the graph. A full treatment of wind directional discrepancies at Paranal would require a significantly larger data set and is beyond the scope of this study.

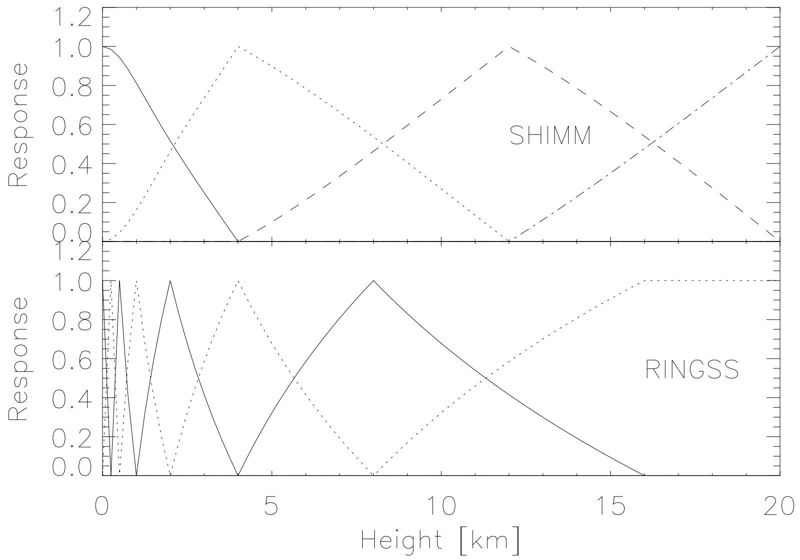

Figure 6.8: A plot of the response functions for the SHIMM and RINGSS. The alternating line styles differentiate the response functions of each reconstructed layer. The sum of responses from all layers is approximately one.

6.2.7 Optical turbulence profiles

Optical turbulence profiles are characterised by the refractive index structure constant C_n^2 as a function of vertical height above the ground. The instruments in this study record the sum of $C_n^2(h)$ over a given volume $\mathrm{d}h$ for each layer using an inversion process. To facilitate a comparison between all instruments which use different models and layers, the RINGSS, MASS-DIMM and SHIMM are directly compared with the high-resolution S-SCIDAR profiles through binning using instrument response functions.

The response functions dictate the measured $C_n^2(h)\,\mathrm{d}h$ response to a single, thin turbulent layer placed at any height throughout the atmosphere. These functions are typically evaluated in simulation by passing a single, thin layer from the ground to the upper atmosphere and plotting the $C_n^2(h)\,\mathrm{d}h$ measured by the instrument in each altitude bin. For scintillation-based instruments such as RINGSS, S-SCIDAR and MASS the response functions usually manifest as triangles on a log scale of height, centred on the altitude of the turbulent layer reconstructed and crossing adjacent bins at half of the input turbulence strength (Tokovinin et al., 2003; Tokovinin, 2021).

For the SHIMM, this approximation also holds well, except for between the ground layer and the first layer. The response functions $f_i(h)$ for the SHIMM and RINGSS are displayed in figure 6.8 on a linear scale of height. These instruments, as well as MASS, estimate turbulence strength in discrete layers as $C_n^2(h_i)\mathrm{d}h = \int f_i(h)C_n^2(h)\mathrm{d}h$. The response functions for the MASS can be found in Kornilov et al. (2003).

Figure 6.9 displays a box and whisker plot of optical turbulence profile measurements from the SHIMM, RINGSS and MASS-DIMM compared with contemporaneous S-SCIDAR profiles. The S-SCIDAR profiles have been binned down to the instrument layers using the response functions and only data within ±2 min of a S-SCIDAR measurement have been used. The whiskers represent the 5th and 95th

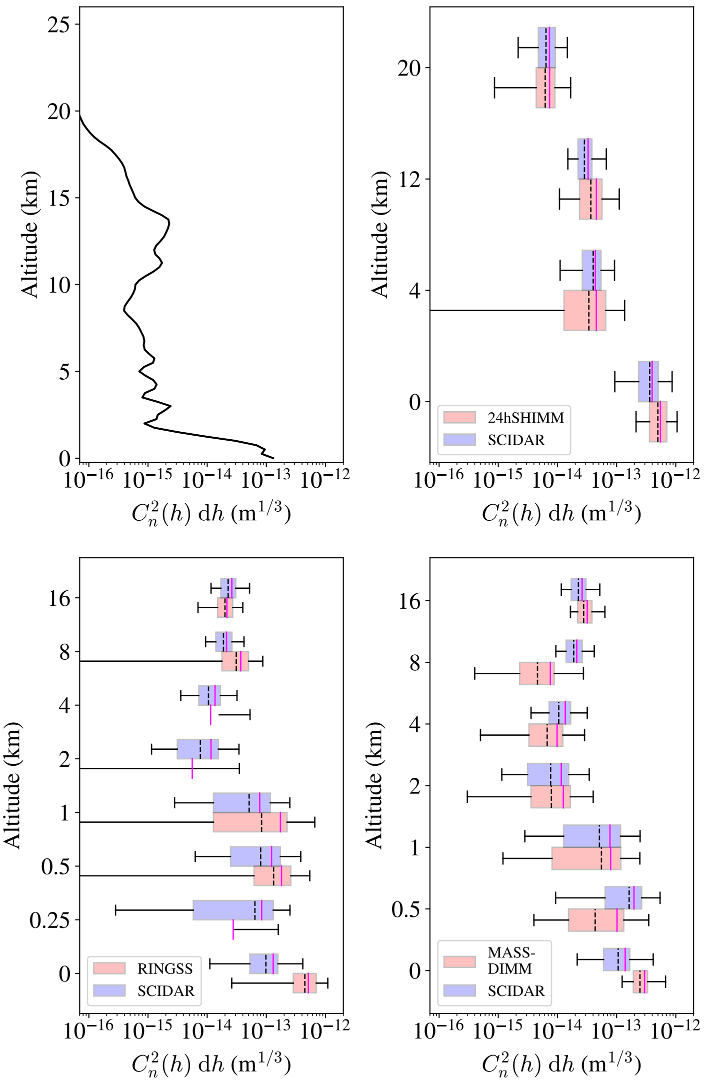

Figure 6.9: A comparison of $C_n^2(h)$ dh profile measurements for all instruments with contemporaneous measurements from the S-SCIDAR. The red boxes show the instrument data from each fitted layer, and the adjacent blue boxes the contemporaneous measurements (within ± 2 min+/- two minutes) from the S-SCIDAR which have been binned to match the instrument layers using the response functions. The extent of coloured boxes represents the first and third quartiles, the dashed line the median measurement, the magenta line the mean, and the whiskers the fifth and 95th percentiles of the distribution. From top left to bottom right, the plot shows the mean S-SCIDAR profile, and box and whisker plots for the SHIMM, RINGSS and MASS-DIMM compared with S-SCIDAR. Significantly smaller values in the top-left panel, compared to other panels, are explained by the thinner d$h = 0.25$ km layers of the S-SCIDAR profiles.

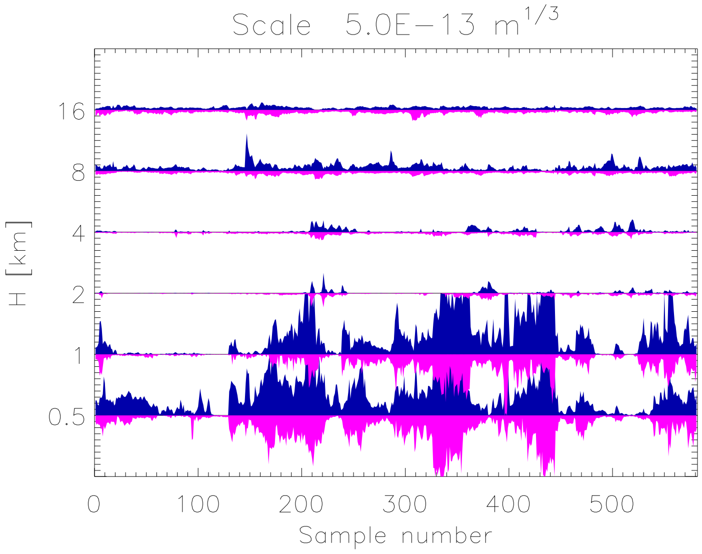

Figure 6.10: Turbulence profiles measured simultaneously by RINGSS (up-facing blue bars) and S-SCIDAR (down-facing magenta bars). S-SCIDAR is matched in resolution and time to RINGSS with the sample number indicating the nth S-SCIDAR measurement taken during the campaign. The width of each band is $5 \times 10^{-13}\,\mathrm{m}^{1/3}$.

percentiles of the distribution, the median is shown as a dashed black line and the mean as a solid magenta line. It is therefore possible to simultaneously compare mean profiles and distributions of measurements in individual layers. Figure 6.9 indicates that all instruments measure a significantly stronger ground layer than the equivalent S-SCIDAR measurement.

A notable feature of the MASS-DIMM profile is a significant underestimation in the 8 km layer, which appears to be the driving cause of the smaller value of median free-atmosphere seeing. For RINGSS and the SHIMM, some layers register zero $C_n^2(h)\,\mathrm{d}h$, hence anomalous boxes and whiskers such as the 4 km layer for the SHIMM and 2 km layer in RINGSS on a a log-scale of $C_n^2(h)\,\mathrm{d}h$. Mean values however agree well for the free-atmosphere layers.

Figure 6.10 shows a detailed comparison between vertical turbulence profiles measured by RINGSS with all 611 available S-SCIDAR profiles matched in time and resolution. Despite different locations and different target sources, we note a strong agreement of timing and localisation of strong turbulence packets, especially in the 0.5 and 1-km layers. The ground layer is not included in this comparison. Fig-

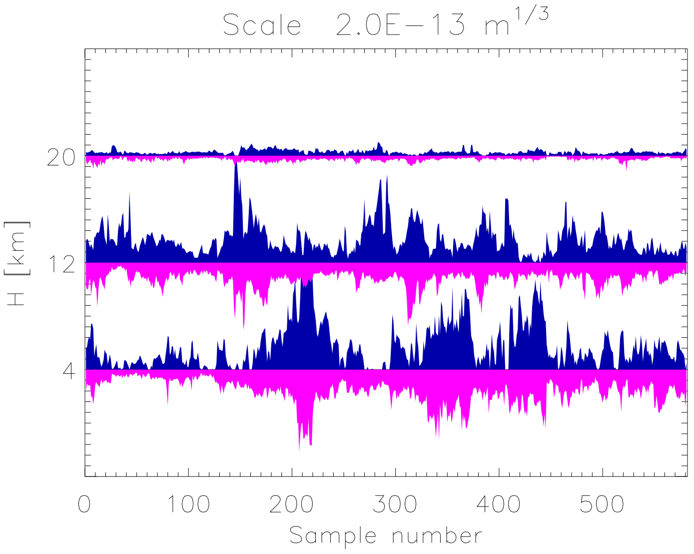

Figure 6.11: Turbulence profiles measured simultaneously by SHIMM (up-facing blue bars) and S-SCIDAR (down-facing magenta bars). S-SCIDAR is matched in resolution and time to SHIMM with the sample number indicating the nth S-SCIDAR measurement taken during the campaign. The width of each band is $2 \times 10^{-13}\,\mathrm{m}^{1/3}$.

ure 6.11 shows a similar plot for the SHIMM. It suggests that the correlation between lower-altitude layers is higher than for high-altitude layers, evidencing the low correlation in isoplanatic angle.

6.2.8 Day and night measurements

The SHIMM measures OT profiles continuously for 24-hours a day by operating at short-wave infrared wavelengths. Compared to the visible light, this extends the validity of the weak-scintillation assumption and reduces the sky background. Additional techniques for rapid background subtraction (Griffiths et al., 2023b) are also employed to ensure accurate photometry.

Figure 6.12 shows a continuous plot of the three main integrated turbulence parameters estimated by the SHIMM: seeing, isoplanatic angle and coherence time. Because the instrument produced a measurement every 1-2 minutes, for presentation purposes the data have been binned such that each data point represents the average of any measurements that fall into ten-minute bins. The sharp diurnal

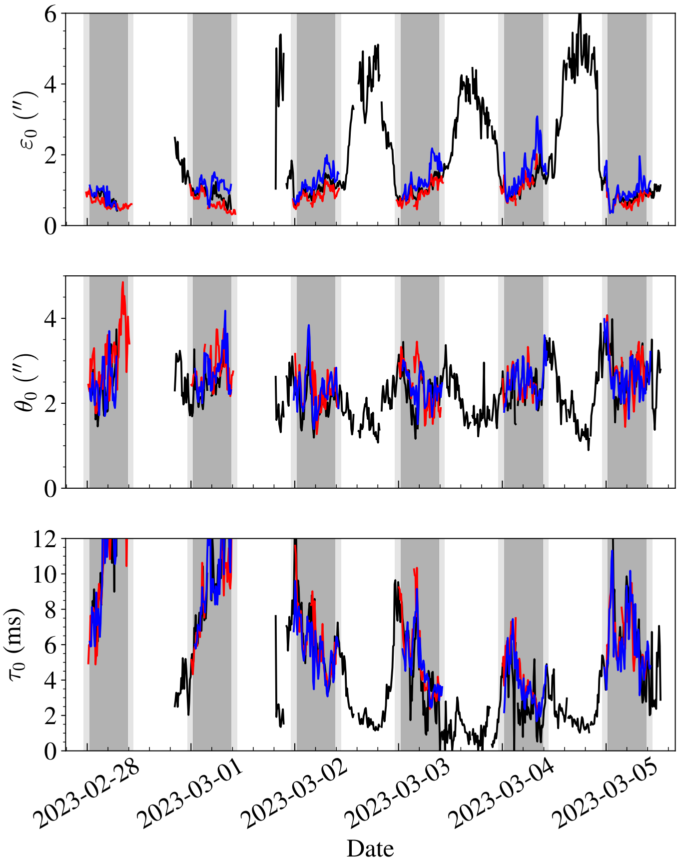

Figure 6.12: Integrated parameters measured by the SHIMM during the campaign. The black line represents SHIMM measurements, the red line DIMM measurements for seeing and MASS-DIMM for the coherence time and isoplanatic angle, and the blue line the RINGSS. All data sets have been binned to 10 min intervals for presentation and dates are in UTC. The white, grey and light grey shades of the background represent daytime, night and twilight respectively

variation in seeing is immediately evident from the graph, with a repetitive, sharp drop in the seeing after sunset leading to the best conditions in earliest part of the night. The general trend thereafter appears to be a gradual increase in the seeing until just after sunrise where it rises very strongly. More work is needed to understand the underlying processes behind this behaviour and the influence of meteorological parameters.

The median value of the daytime seeing, calculated between sunrise and sunset, was found to be 2.65″, isoplanatic angle 2.05″ and coherence time 2.4 ms. It is notable that measurements of the isoplanatic angle, which is insensitive to low-altitude turbulence, do not experience the same distinct variation. This suggests that the increased turbulence strength during daytime is a result of solar heating at the ground affecting the boundary layer, and the upper atmosphere is relatively unaffected. The coherence time follows a similar trend to the Fried parameter likely due to dominance of the strong ground layer turbulence.

6.3 TURBO

The TURBO experiment is an example application of the SHIMM for site monitoring for optical communications. TURBO is a facility consisting of two SHIMM instruments. One is permanently mounted in a ScopeDome 3m clamshell dome and one on a tripod, both on top of the CommsensLab building at the Universitat Politecnica de Catalunya (UPC) in Bacelona, Spain. The permanently mounted SHIMM (called TURBO 1) uses the same hardware detailed in table 5.1 and works automatically to measure urban atmospheric optical turbulence conditions for 24-hours a day continuously in clear weather conditions. Including the dome, weather station system and an all-sky camera, the facility has all it needs to enable robotic operation. However it is still under development and is limited to automatic operation with operator intervention to avoid poor weather and cloudy conditions. The tripod-mounted SHIMM (TURBO 2) uses the same optomechanical design, but on a 20 cm telescope with the more lightweight CGX mount. This makes it a portable instrument suitable for short-term site monitoring at other locations. A picture of the two instruments on the roof of the CommSensLab building at UPC is shown in figure 6.13. The aims of the project are to firstly characterise seasonal turbulence conditions in a typical southern European urban environment. Such sites are of great interest as optimal locations for nodes in a future European OGS network (Fuchs and Moll, 2015). A database of 24-hour urban turbulence measurements would be a significant asset for researchers modelling ground to satellite free-space optical links, and especially for those designing adaptive optics systems for OGSs.

Figure 6.13: TURBO 1 and 2 locations on the roof of the UPC CommSensLab building. On the left, the OTA of TURBO 1 can be seen extruding from the clamshell dome, on the right TURBO 2 is operating on a tripod mount.

The second aim of the experiment is to use this database of urban turbulence statistics for comparison with turbulence forecasting models such as Quatresooz et al. (2023), and to explore data assimilation techniques such as auto-regression (Masciadri et al., 2023) for enhancing the accuracy of forecast predictions. These forecasts will be critical to optimal management of OGS networks of the future in predicting outages due to strong turbulence, and for early identification of suitable OGS sites without having to travel to each location with a site monitor.

6.3.1 TURBO 1 results

During the commissioning process there have been three short measurement campaigns with the TURBO 1 instrument. Although there is not yet sufficient seasonal coverage in the results, there is enough to take an early look at the typical site conditions. Results of all available data (a total of 7164 profiles and at least 70 hours of measurements) collected so far by TURBO 1 are displayed below in figure 6.14. Measurements have been categorised as made during the daytime or night-time using sunset and sunrise as the cutoff points between the two regimes.

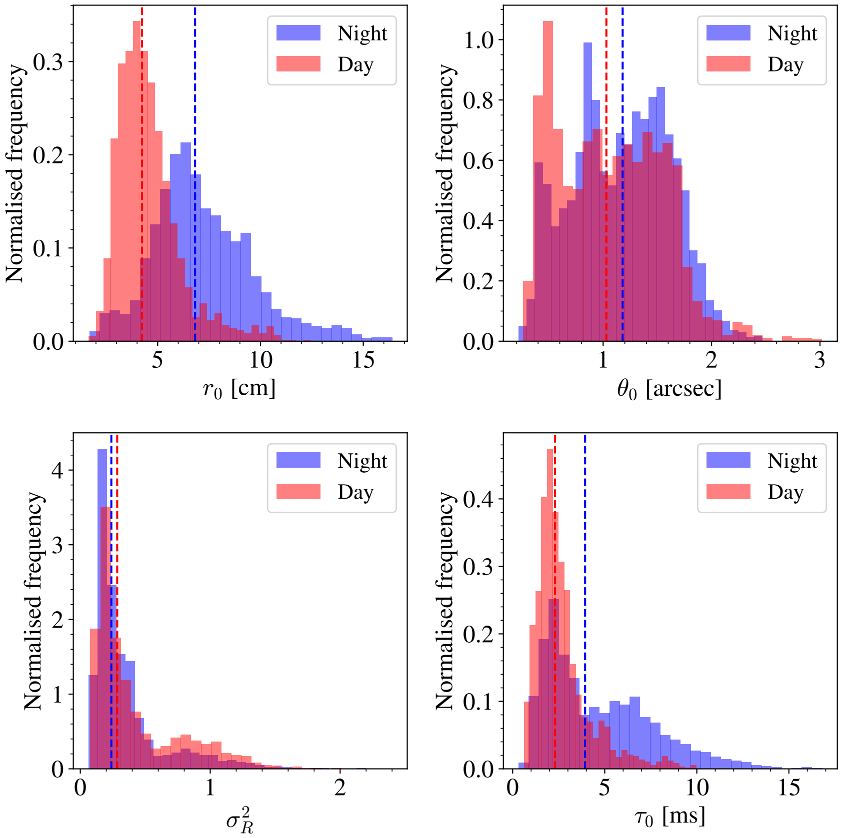

Figure 6.14: Histograms of key turbulence parameters measured during the cumulative operating time of TURBO 1. The blue bars represent the data collected at night (between sunset and sunrise) and the red bars the daytime (between sunrise and sunset). The median values of each distribution are represented by the vertical dashed lines on the plot. The values of each median are shown in table 6.3. Histogram frequencies are normalised such that the area under the histogram is equal to 1.

Distributions of turbulence parameters tend therefore to be fairly wide as conditions do not change between day and night suddenly, but rather over the course of a few hours as can be seen in figure 6.12. Separation of the two regimes is necessary nonetheless as some turbulence parameters exhibit strong diurnal variation which would otherwise be obscured in a combined analysis. Figure 6.14 indicates in all measures that the turbulence is stronger during the daytime. The most significant changes are in r_0, the median of which decreases from 6.82 cm to 4.24 cm, and coherence time which experiences a similarly large drop of more than 1.6 ms from 3.93 ms to 2.30 ms. Changes in isoplanatic angle and Rytov variance, parameters

	Day			Night		
Parameter	Q1	Median	Q3	Q1	Median	Q3
r_0 [cm]	3.50	4.24	5.19	5.60	6.82	8.63
θ_0 [$''$]	0.619	1.03	1.44	0.83	1.18	1.52
σ_R^2	0.18	0.28	0.59	0.17	0.24	0.39
τ_0 [ms]	1.73	2.30	3.09	2.28	3.93	6.63

Table 6.3: Median and quartiles of all day and night measurements from the TURBO 1 instrument.

that are more sensitive to high altitude turbulence, are smaller but nonetheless point towards stronger turbulence during the daytime.

These results have implications for free-space optical communications activities. Taking the median value of r_0 during the daytime, its value can be calculated along the line-of-sight, for example, for a typical case of an OGS receiving a 1550 nm laser downlink beam in an 80 cm telescope from a geostationary satellite. For the best-case scenario of the satellite at the same longitude as the Barcelona site, the elevation angle of observations would be roughly 48°. This would lead to $D/r_0 \approx 5.8$ for observations along the communications channel. From the first quartile it can be seen that $D/r_0 > 7$ for 25% of the time. Both of these cases will result in significant speckling of the PSF for optical communications. AO would therefore be beneficial for improving link performance by enabling more efficient coupling into a single-mode fibre. Furthermore strong scintillation can greatly affect the performance of AO systems. This data shows that the median Rytov variance during the daytime is comparable to the upper limit of the weak-scintillation regime (at 500 nm) of 0.3, and frequently above this threshold during both the day and the night. Scaling for the communications wavelength and satellite elevation angle, $\sigma_R^2 \approx 0.54$ at 500 nm and zenith would mean that the weak scintillation limit is exceeded along the communication channel at 1550 nm. Using table 6.3, during the day more than 25% of the profiles exceeded this value. The smaller secondary peak at $\sigma_R^2 \approx 0.8$, typically associated with a large $C_n^2(h)\,\mathrm{d}h$ in the 12 km layer, comfortably exceeds this limit for such a system.

This example illustrates the use of this data for modelling of ground-to-satellite optical links. There is no general database of site statistics for “typical” locations. In general, the atmospheric turbulence along the optical channel for free-space optical communications is modelled using the Hufnagel-Valley profile (Osborn et al., 2021; Conan et al., 2019), or by modification of profiles taken from existing astronomical databases (Lognoné et al., 2023). In fact the results from the TURBO experiment are broadly in agreement with both of these approaches except for characterisation of isoplanatic angle. The median θ_0 is smaller than the $1.37''$of the strong Hufnagel-Valley profile presented in Osborn et al. (2021), indicating strong high-altitude turbulence above the site. The key advantage of using SHIMM data over the Hufnagel-Valley profile for modelling is the introduction of distributions of optical turbulence parameters and the ability to point to a average, or a worst-case scenario.

6.3.2 Comparison of TURBO 1 and TURBO 2

A comparison of the two SHIMM instruments from the TURBO experiment was an important step for validating the experiment. To this end, in a similar fashion to the Paranal campaign, the two instruments were run at the same time to generate a set of contemporaneous measurements. The two instruments were co-located on the roof of the UPC CommSensLab building as in figure 6.13, approximately within 3 m of each another. TURBO 1 was was operating within the dome approximately 2 m above the ground while TURBO 2 was operating on a tripod mount just over a meter above the ground. Similar to above, all measurements from TURBO 2 are time-matched with data from TURBO 1 within a maximum limit of 2 minutes. Then, scatter plots could be made to compare measurements of the key optical turbulence parameters. This data is found in figure 6.15.

The plot shows overall a reasonable level of agreement between the two instruments with good correlation on measurements of the Fried parameter and coherence time. The correlations for isoplanatic angle and Rytov variance are however significantly lower at 0.46 and 0.52 respectively. When analysing the bias between each instru-

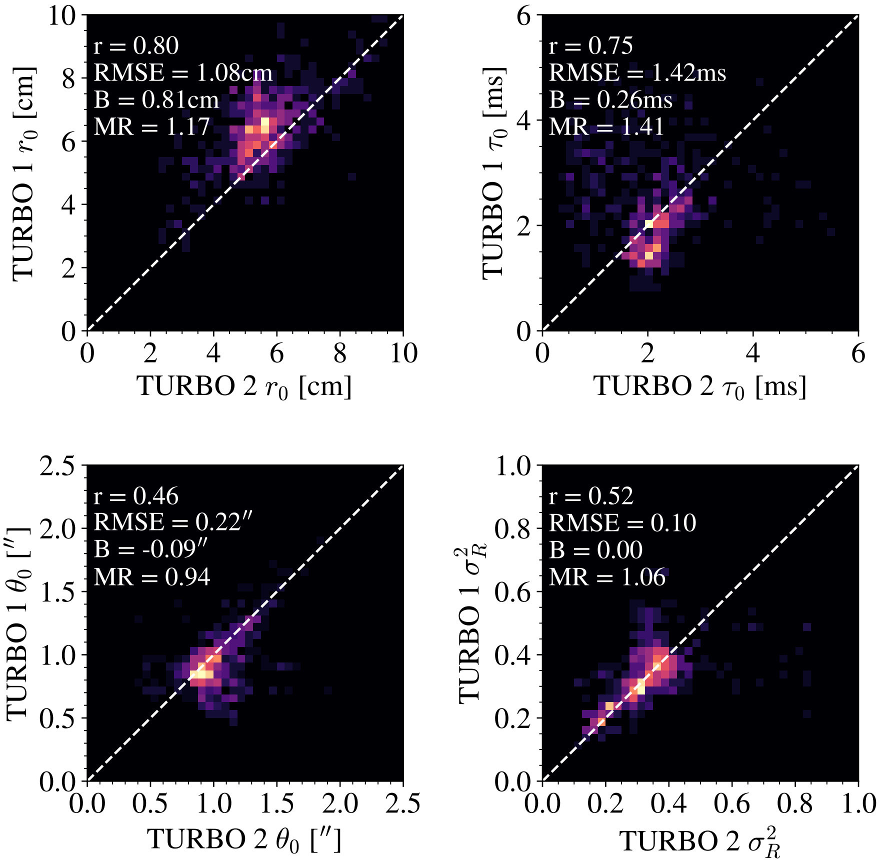

Figure 6.15: A comparison of contemporaneous measurements of the four key turbulence parameters with TURBO 1 on the y-axis and TURBO 2 on the x-axis.

ment the opposite case appears true. The seeing and coherence time exhibit a bias towards larger r_0 and τ_0 on TURBO 1, whereas for measurements of isoplanatic angle and Rytov variance the bias is extremely small. The most pronounced bias is in measurements of coherence time, where TURBO 2 for a number of points registers a much small coherence time than TURBO 1. Due to the lower signal-to-noise ratio of TURBO 2 and the smaller sub-aperture size and separations, the instrument responses are expected to differ.

To investigate this discrepancy, the measurements of both coherence time and Fried parameter have been plotted for a 27-hour sequence. This time sequence includes a number of contemporaneous measurements from the two instruments. Including also the average ground level wind speed measured by the TURBO weather station, the largest bias between the two instruments can be found on the night of the 9th of May where the wind speed drops to a very low level of under $1\,\mathrm{m\,s^{-1}}$. Low wind speeds have been associated with discrepancy between turbulence monitoring instruments (Butterley et al., 2020b); they are associated with poorer statistical convergence of measurements as there will be fewer independent realisations of turbulent phase. Furthermore, local heat sources are likely to have a greater impact if the air is moving slowly and the air vent for the building situated next to to the TURBO 2 instrument could have been increases local turbulence. A greater number of continuous measurements in more diverse conditions are needed to identify the discrepancy in this data.

6.4 Dome seeing

The rich TURBO 1 data set enables investigation of the additional concepts described in chapter 3. In this section, the dome seeing contribution to the SHIMM slope measurements is examined. To estimate the dome-seeing contribution, the subtraction algorithm as described in section 3.10 was applied to extract the slope auto-covariance peak from the dome seeing. Given the dome seeing auto-covariance response (similar to figure 3.12), there are a number of approaches to measuring its strength. To fit a value of $C_n^2(h)\,\mathrm{d}h$, as in Osborn and Alaluf (2023), a Kolmogorov or Von Kármán model must be assumed. This work avoids any such assumptions as the power spectrum of the dome turbulence does not follow either example and so a comparison is not particularly meaningful. Instead, this work will use the dome-seeing contribution to the centroid variance to as a quantitative measurement of the dome seeing. This will be referred to as the dome spot motion.

Figure 6.17 shows a 34-hour time sequence of the measured dome spot motion. The figure also shows the dome-seeing corrected measurement of r_0. The graph shows that broadly, the dome seeing contribution is larger during the daytime, and that r_0 is smaller during the daytime. However outside of the daytime, the two appear

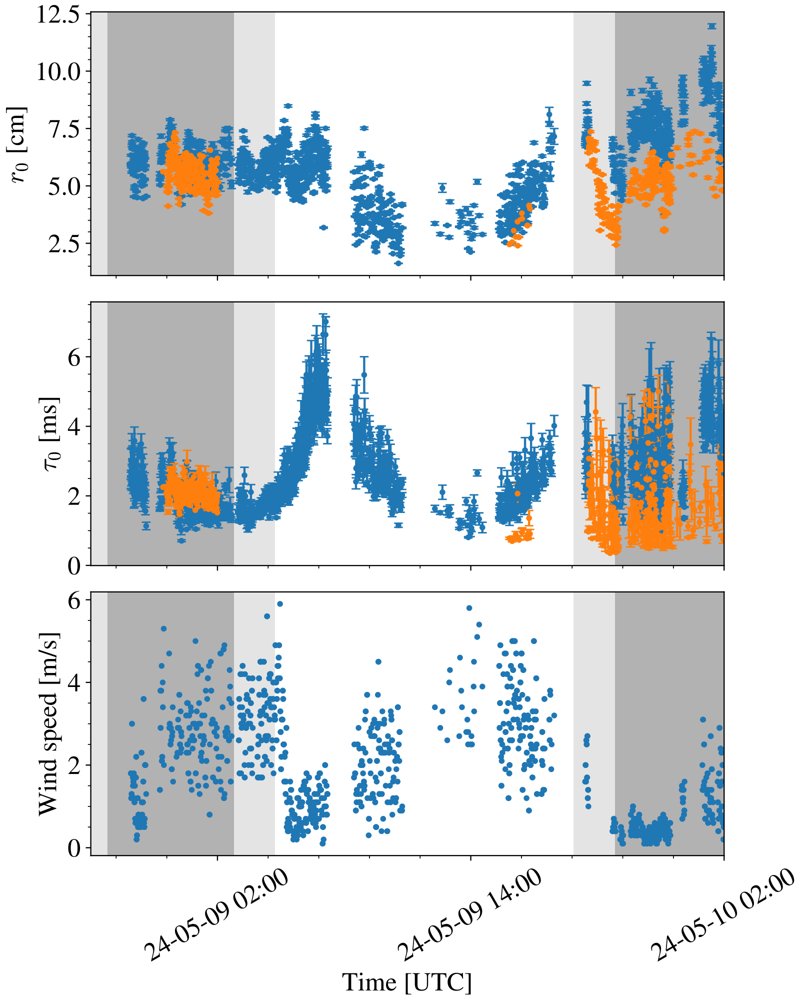

Figure 6.16: Time sequence of r_0 (top), τ_0 (middle) and the wind speed (bottom) measured by the TURBO system over 27-hours of almost-continuous operation during commissioning. For the turbulence parameter measurements, blue points represent measurements by TURBO 1, and orange points measurements by TURBO 2.

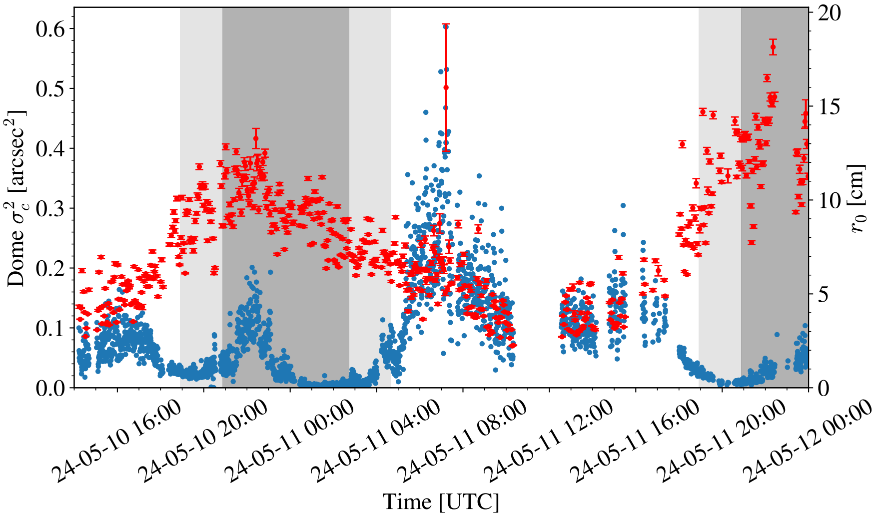

Figure 6.17: A 34-hour time sequence of the estimated magnitude of dome seeing quantified by its centroid variance contribution (blue points, left axis) and the measurements of r_0 after dome seeing correction (red points, right axis) from TURBO 1. Only every 5th measurement of r_0 has been plotted to aid visibility.

to be poorly correlated, this can be seen in the spike at 22:00 on the 10th of May in the dome seeing where no obvious change in r_0 is visible. These results were further plotted against key meteorological parameters from the weather station: wind speed and temperature. However there no was clear correlation with either of these that explained the short-timescale features of figure 6.17 such as the dips in the dome seeing throughout the transition periods between day and night, or any of the sharp spikes in the dome seeing strength. More work is needed including cross-validation with a separate instrument to examine the performance of the dome seeing strength estimation.

6.5 Conclusion

This chapter presented the results of two major turbulence monitoring campaigns involving the SHIMM. The first was at at Cerro Paranal observatory between the 2023 February 27 and March 5. The aim of this study was to characterise novel turbulence monitoring instruments, the SHIMM and RINGSS, against existing instruments at the site through comparison measurements of vertical OT profiles and integrated parameters. Data collected from these two instruments during the campaign were further compared against measurements from the S-SCIDAR and the MASS-DIMM by assessing the RMSE, bias, and correlation of contemporaneous data from pairs of instrument. Additionally median values from the whole campaign were calculated and compared to long-term averages. It was found, as in previous campaigns, that the seeing measured near the old 1998-DIMM tower was significantly larger than for the S-SCIDAR and 2016-MASS-DIMM. In general, however, strong correlation was found across all seeing and free-atmosphere seeing measurements. Isoplanatic angle measurements displayed a close agreement in median values, but were less correlated between all instruments, which is likely a result of limitations in sensitivity to high altitude turbulence and differences in the sampled turbulence volumes. Coherence time measurements were strongly correlated between all instruments, however the RMSE of distributions was relatively large. The influence of wind direction on statistical agreement between measurements was also investigated which showed increased spread and bias in RINGSS and SHIMM seeing comparisons with the MASS-DIMM for northerly winds. Additionally, changes in bias for parameters that should have no dependence on the wind direction could be attributed to non-Kolmogorov effects. The accuracy of OT profiling was also investigated by comparison of profiles with contemporaneous S-SCIDAR measurements binned using instrument response functions. The two visiting instruments were found to agree well with the S-SCIDAR, with expected bias towards stronger turbulence in the ground layer. It was also observed that the MASS-DIMM systematically underestimates the 8 km layer. Finally, the first measurements of continuous optical turbulence parameters at Paranal were presented which indicate a predictable and extreme diurnal variation in seeing with a median daytime value of 2.65 $''$ compared to equivalent night-time median of 0.88 $''$ arcsec, which is assumed to be driven by changes in the boundary layer due to solar heating in the early morning and rapid cooling in the evening as similar changes are not present in the isoplanatic angle which is sensitive to high altitude turbulence. This experiment suggests that the best seeing conditions are in the earliest part of the night.

The second campaign was the TURBO experiment in Barcelona, Spain, to characterise a typical urban southern European site for an OGS. It consisted of two SHIMM turbulence monitors, one permanently installed inside a dome on a 28 cm telescope, and one on a smaller, portable 20 cm telescope. These were referred to as TURBO 1 and 2 respectively. The cumulative results, spanning over 70 hours of measurements to date form TURBO 1, have been presented in this section. The median measurements of integrated turbulence parameters agree well with the Hufnagel-Valley, although a significant range of conditions were recorded for both daytime and night-time data. It was found, as for Paranal, that turbulence is significantly stronger during the day, rising from a median r_0 of 4.2 cm to 6.8 cm. This is far less significant than that seen at Paranal observatory where the median r_0 changes from 3.8 cm to 11.4 cm. In stark contrast to Paranal, almost half of the daytime measurements indicated strong scintillation conditions at optical wavelengths. It was reasoned that for optical links to geostationary satellites, the turbulence along the channel would also experience strong scintillation more than 25% of the time. Following this, a comparison was made between TURBO 1 and 2 results. Strong correlation and a slight bias was found in r_0 and τ_0. In Rytov variance and the isoplanatic angle, there was no bias but a reduced correlation. The discrepancy in the first two was attributed to some low-wind measurements, and potentially some local turbulence from an air vent on the roof. The lower correlation was attributed to more outliers and the width of high-altitude response functions leading to more spread in the data. Finally, a quantitative measure of the dome seeing is extracted from the data analysis and plotted for a time sequence. It is found to be larger during the day, and to have a low correlation with r_0 and ground level meteorological parameters. It is found to dip during transition periods between day and night, corresponding to some of the best seeing conditions.

This may be related to temperature of the the environment and air reaching equilibrium, however without more detailed data from the environment the causes of these trends can only be speculated upon.

Chapter 7

Conclusions

Optical turbulence monitoring activities have long held an important role in site characterisation for some of the most influential ground-based telescopes and instruments. While large-telescope based optical turbulence profilers such as the Stereo-SCIDAR offer the most detailed characterisation of the profile of atmospheric optical turbulence, small-telescope monitors are no less important due to being cheap, portable and easy to implement. In astronomy, current key applications of such instruments include site monitoring for astronomical observatories, specifically for the upcoming 20-40 m Extremely Large Telescopes (ELTs), the next generation of large solar telescopes and providing data for validation and assimilation into turbulence forecasting software which will be critical for effective operation of ELT instruments. Turbulence monitoring technologies are also becoming widely employed in free-space optical communications. Bidirectional ground-to-satellite optical links will be required to run for 24-hours a day and in strong turbulence conditions at urban sites. The conditions at such sites is poorly understood as historical site monitoring has focused primarily on pristine mountain-top sites for astronomy. The performance of the optical link is also strongly influenced by the optical turbulence conditions. Therefore 24-hour site characterisation, monitoring and forecasting will be essential building blocks for a successful communications network. Such networks will include a large number of OGSs in diverse sites, heavily favouring relatively cheap and easily produced small-telescope turbulence monitors that can characterise both daytime and nighttime turbulence conditions.

7.1 The SHIMM optical turbulence profiler

The subject of this thesis was the Shack Hartmann image motion monitor (SHIMM) instrument. The SHIMM is an optical turbulence monitor based around a Shack-Hartmann wavefront sensor observing single, bright stars in the SWIR. It has been shown that by leveraging InGaAs technology, continuous, 24-hour monitoring of atmospheric optical conditions can be achieved on a small telescope due to a reduction in turbulence strength, sky background and brighter target stars. This work aims to address demand from the fields of astronomy and free space optical communications for a 24-hour optical turbulence monitor. This capability allows for novel techniques to be investigated such as data assimilation into turbulence forecasting models to provide an early prediction of the turbulence conditions at the start of the night and 24-hour validation of OGS adaptive optics system performance.

In describing the SHIMM profiling method, a novel Z-tilt model for wavefront sensor slope covariances in Kolmogorov turbulence was presented along with an assessment of modifications to the model for non-zero exposure times, polychromatic light and the influence of dome turbulence. The FADE method of measuring optical turbulence coherence time was implemented successfully through modal Zernike wavefront reconstruction. Utilising high frame rates and the $C_n^2(h)\,\mathrm{d}h$ measured independently by the profiling method, the wind speed profile and therefore the coherence time could be estimated. These techniques were validated for noisy daytime data using Monte Carlo simulations for the instrument. These simulations indicated a critical signal-to-noise ratio of 70 to obtain accurate measurements at the system central wavelength of 1280 nm. These Monte Carlo simulations were further used to determine optimal methods for extracting slope and intensity measurements from the wavefront sensor images. It was shown that a padded correlation centroid algorithm offered the closest fit to the models, and the optimal window size for slicing out the spot and measuring its intensity was identified. Finally the impact of regularisation in solving the inverse problem of profile reconstruction was investigated to attempt to fit more layers to the SHIMM data. The regularisation parameter was chosen using the Gaussian maximum whiteness of the residuals as a optimisation metric. It was found that regularisation led to greater correlation and fewer missing values when fitting six layers with weighted least squares, however this came at the cost of over-smoothing in the first two atmospheric layers where some turbulent energy was transferred from the ground layer to the first atmospheric layer. There was no observed benefit to regularisation when fitting a small number of layers.

Following this, a full description of the prototype instrument design was made. A simple InGaAs optical design was selected which reduced background light from the sky, gave more bright star targets and mitigated potential strong turbulence conditions. The two key aspects of the design were the inclusion of a motorised shutter/iris to function as a field stop and full shutter, and a high speed InGaAs detector. The central wavelength of the instrument was estimated to be 1280 nm, and the transmission spectrum analysed to determine that the sensitivity limit of SNR of 70 corresponded to a magnitude 0.07 star in the J band. A target availability analysis showed that this corresponded to at least one target at all times of the year for an example site in Barcelona. Finally the software design and analysis pipeline was discussed at length highlighting the necessary procedures to handle high speed data acquisition while retaining data quality on a small telescope.

The final part of the thesis was dedicated to analysing on-sky data from the instrument. The first half of this focused on a cross-validation campaign between a number of other contemporary turbulence monitoring instruments, with a wider view to compare each instrument in the context of OT profiling for ELT-class telescopes. The second part detailed the latest results from the TURBO experiment in Barcelona, a permanently mounted SHIMM inside a clamshell dome combined with a weather monitoring system. The site was chosen to be representative of that of a typical European optical ground station. The data will be used to model expected link performances in similar urban environments. It was found that the site experienced less dramatic variance in turbulence strength between day and night compared to Paranal. However the turbulence was still strong, particularly during the day where it had a median of 4.24 cm. There was also evidence of much stronger scintillation conditions than at astronomical sites such as Paranal.

7.2 Future work and applications

This work represents the development and initial testing phase of the SHIMM instrument. Included in chapter 6 are some of the longest-term SHIMM measurements collected to date. Limitations on the software implementation and suitable sites have so far restricted the amount of data that could be collected. Going forward, recent work on the TURBO installation in Barcelona has provided a solid basis on which to collect much more data, and so a key aim for the near future will be to obtain significant quantities of seasonal data and 24-hour measurements using this system. The TURBO system further provides a blueprint for a turbulence monitoring station that can be replicated at other locations. This project will also apply the SHIMM data in meso-scale turbulence forecasts. This will involve extending the validation work in Quatresooz et al. (2023) in which $C_n^2(h)\,\mathrm{d}h$ models are evaluated against on-sky the instrument measurements. The next steps for this work will be evaluating accuracy of predictions of integrated turbulence parameters beyond only r_0, using larger data sets and input from the local weather station. Furthermore, large continuous data sets offer the possibility of using data assimilation techniques such as auto-regression (Masciadri et al., 2023) to improve the accuracy of predictions from the forecast. The SHIMM is also currently employed as a dedicated site monitor for the ALASCA experiment at the OGS at Mount Teide Observatory (Biasi et al., 2023). The instrument will be performing turbulence profiling using the downlink beam from the Alphasat geostationary satellite during the AO system commissioning. The turbulence measurements will be used with the FAST Fourier adaptive optics simulation software (Farley et al., 2022) to model the AO system performance. This will then be compared to results from the experiment to provide a 24-hour source of external validation.

There are also several investigations into the SHIMM analysis that could follow from this work. The next stage of development requires testing of the dome turbulence estimation technique. This could be accomplished by taking simultaneous measurements with a dedicated dome turbulence monitor such as that described in Osborn and Alaluf (2023) and evaluating the correlation of the dome seeing measures from both instruments. The impact of regularisation on the profiling inversion has not been studied exhaustively in this work. This is due to the large number of methods for choosing the regularisation parameter, and the possibility of using alternative methods which could include neural networks and machine learning. Other techniques include representing turbulence profiles using sparse, continuous basis functions and solving for their coefficients, or applying principle component analysis. Finally, the effects of altering the SHWFS geometry are yet to be studied in detail. A natural extension to this work could be to simulate a SHIMM on a 0.5 m telescope with 10 subapertures across the pupil, and to investigate whether more layers could be fit as a result of the increased number of sub-aperture baselines.

Appendix A

Statistical comparison parameters

In this section, the equations for statistical comparison parameters used in figures 2-5 and tables 1-2 are defined. In all equations $i = 1, 2, 3 \ldots N$ indicates a sample of N independent turbulence parameter measurements, X_i the measurement of the parameter by instrument X and Y_i the contemporaneous measurement of the parameter by instrument Y. The bias, B is defined as

$$\mathrm{B} = \sum_{i=1}^{N} \frac{Y_i - X_i}{N}, \tag{A.1}$$

the root mean square error (with bias subtracted), or RMSE, as

$$\mathrm{RMSE} = \sqrt{\sum_{i=1}^{N} \frac{([Y_i - \overline{Y_i}] - [X_i - \overline{X_i}])^2}{N}}, \tag{A.2}$$

where $\overline{Y_i}, \overline{X_i}$ are the means of the contemporaneous measurements, and the mean ratio by

$$\mathrm{MR} = \frac{1}{N} \sum_{i=1}^{N} \frac{Y_i}{X_i}. \tag{A.3}$$

Bibliography

A. Abahamid, J. Vernin, Z. Benkhaldoun, A. Jabiri, M. Azouit, and A. Agabi. Seeing, outer scale of optical turbulence, and coherence outer scale at different astronomical sites using instruments on meteorological balloons. *Astronomy and Astrophysics*, 422(3), 2004. ISSN 00046361. doi: 10.1051/0004-6361:20040215.

M. S. C. Almeida and M. A. T. Figueiredo. Parameter Estimation for Blind and Non-Blind Deblurring Using Residual Whiteness Measures. *IEEE Transactions on Image Processing*, 22(7):2751–2763, 7 2013. ISSN 1057-7149. doi: 10.1109/TIP.2013.2257810. URL `http://ieeexplore.ieee.org/document/6497608/`.

P. P. Andrade, P. J. V. Garcia, C. M. Correia, J. Kolb, and M. I. Carvalho. Estimation of atmospheric turbulence parameters from Shack–Hartmann wavefront sensor measurements. *Monthly Notices of the Royal Astronomical Society*, 483 (1):1192–1201, 2 2019. ISSN 0035-8711. doi: 10.1093/mnras/sty3181.

L. C. Andrews and R. L. Phillips. *Laser Beam Propagation through Random Media.* SPIE, 1000 20th Street, Bellingham, WA 98227-0010 USA, 9 2005. ISBN 9780819459480. doi: 10.1117/3.626196. URL `http://ebooks.spiedigitallibrary.org/book.aspx?doi=10.1117/3.626196`.

E. Aristidi, A. Ziad, Y. Fantéï-Caujolle, J. Chabé, C. Giordano, C. Renaud, and H. Lantéri. Monitoring daytime and nighttime optical turbulence profiles with the PML instrument. *AO4ELT 2019 - Proceedings 6th Adaptive Optics for Extremely Large Telescopes*, 2 2019. URL `http://arxiv.org/abs/2002.04947`.

F. Assémat, R. Wilson, and E. Gendron. Method for simulating infinitely long and non stationary phase screens with optimized memory storage. *Optics Express*, 14 (3):988, 2006. ISSN 10944087. doi: 10.1364/oe.14.000988. URL `https://opg.optica.org/oe/abstract.cfm?uri=oe-14-3-988`.

R. C. Aster, B. Borchers, and C. H. Thurber. *Parameter Estimation and Inverse Problems*. Elsevier, 2013. ISBN 9780123850485. doi: 10.1016/C2009-0-61134-X. URL `https://linkinghub.elsevier.com/retrieve/pii/C2009061134X`.

M. Azouit and J. Vernin. Remote Investigation of Tropospheric Turbulence by Two-Dimensional Analysis of Stellar Scintillation. *Journal of the Atmospheric Sciences*, 37(7), 1980. ISSN 0022-4928. doi: 10.1175/1520-0469(1980)037<1550:riottb>2.0.co;2.

M. Baril, O. Lai, G. Zahariade, F. Bouchacourt, G. Perrin, P. Fedou, and J. Woillez. 'OHANA-Iki: a test-bed for the 'OHANA beam combiner and delay line at CFHT. In *Optical and Infrared Interferometry II*, volume 7734, page 77342C. SPIE, 7 2010. doi: 10.1117/12.856219. URL `http://proceedings.spiedigitallibrary.org/proceeding.aspx?doi=10.1117/12.856219`.

R. Barletti, G. Ceppatelli, E. Moroder, L. Paternò, and A. Righini. A vertical profile of turbulence in the Atlantic air mass measured by balloon-borne radiosondes. *Journal of Geophysical Research*, 79(30), 1974. doi: 10.1029/jc079i030p04545.

A. G. Basden, R. M. Myers, and E. Gendron. Wavefront sensing with a brightest pixel selection algorithm. *Monthly Notices of the Royal Astronomical Society*, 419(2):1628–1636, 1 2012. ISSN 00358711. doi: 10.1111/j.1365-2966.2011.19825.x. URL `https://academic.oup.com/mnras/article-lookup/doi/10.1111/j.1365-2966.2011.19825.x`.

L. Beesley, J. Osborn, R. Wilson, O. Farley, R. Griffiths, and G. Love. Exploring atmospheric optical turbulence: Observations across zenith angles. *Applied Optics*, 4 2024. ISSN 1559-128X. doi: 10.1364/AO.519063.

F. Bennet, R. Conan, C. D'Orgeville, M. Dawson, N. Paulin, I. Price, F. Rigaut, I. Ritchie, C. Smith, and K. Uhlendorf. Adaptive optics for laser space debris removal. In B. L. Ellerbroek, E. Marchetti, and J.-P. Véran, editors, *Proc. SPIE 8447, Adaptive Optics Systems III*, volume 8447, pages 844744–844744. International Society for Optics and Photonics, 9 2012. doi: 10.1117/12.925773. URL `http://proceedings.spiedigitallibrary.org/proceeding.aspx?articleid=1358996`.

R. Biasi, D. Bonaccini Calia, M. Centrone, M. Enderlein, M. Faccini, O. Farley, D. Gallieni, D. Gooding, P. Haguenauer, P. Janout, D. Jenkins, F. Lison, J. Luis, N. Martinez Rey, J. Osborn, C. Patauner, D. Pescoller, M. Reyes, L. Sabatini, L. Salvi, Z. Sodnik, D. Alaluf, M. Tintori, M. Tordi, M. Townson, H. Virdee, D. P. Wei, and W. L. Clements. ALASCA: the ESA Laser Guide Star Adaptive Optics Optical Feeder Link demonstrator facility. In K. Minoglou, N. Karafolas, and B. Cugny, editors, *International Conference on Space Optics — ICSO 2022*, page 186. SPIE, 7 2023. ISBN 9781510668034. doi: 10.1117/12.2690989.

M. Birch, J. R. Beattie, F. Bennet, N. Rattenbury, M. Copeland, T. Travouillon, K. Ferguson, J. Cater, and M. Sayat. Availability, outage, and capacity of spatially correlated, Australasian free-space optical networks. *Journal of Optical Communications and Networking*, 15(7), 2023a. ISSN 19430639. doi: 10.1364/JOCN.480805.

M. Birch, F. Bennet, M. Copeland, D. Grosse, J. Munro, and T. Travouillon. A small, low-cost, turbulence profiling instrument for free-space optical communication. In H. Hemmati and B. S. Robinson, editors, *Free-Space Laser Communications XXXV*, page 52. SPIE, 3 2023b. ISBN 9781510659315. doi: 10.1117/12.2646569. URL `https://www.spiedigitallibrary.`

org/conference-proceedings-of-spie/12413/2646569/A-small-low-cost-turbulence-profiling-instrument-for-free-space/10.1117/12.2646569.full.

J. Borgnino. Estimation of the spatial coherence outer scale relevant to long baseline interferometry and imaging in optical astronomy. *Applied Optics*, 29(13), 1990. ISSN 0003-6935. doi: 10.1364/ao.29.001863.

E. Bustos and A. Tokovinin. Dome seeing monitor and its results for the 4-m Blanco telescope. In R. Gilmozzi, H. K. Marshall, and J. Spyromilio, editors, *Ground-based and Airborne Telescopes VII*, page 21. SPIE, 7 2018. ISBN 9781510619531. doi: 10.1117/12.2309652. URL https://www.spiedigitallibrary.org/conference-proceedings-of-spie/10700/2309652/Dome-seeing-monitor-and-its-results-for-the-4-m/10.1117/12.2309652.full.

T. Butterley. SCIDAR reprocessing: part of the MASS reprocessing investigation part 2b. Technical report, ESO, Durham University, 4 2021.

T. Butterley, R. W. Wilson, and M. Sarazin. Determination of the profile of atmospheric optical turbulence strength from SLODAR data. *Monthly Notices of the Royal Astronomical Society*, 369(2):835–845, 6 2006. ISSN 00358711. doi: 10.1111/j.1365-2966.2006.10337.x. URL http://mnras.oxfordjournals.org/cgi/doi/10.1111/j.1365-2966.2006.10337.x.

T. Butterley, M. Sarazin, M. Le Louarn, J. Osborn, and O. J. D. Farley. Correction of finite spatial and temporal sampling effects in stereo-SCIDAR. In D. Schmidt, L. Schreiber, and E. Vernet, editors, *Adaptive Optics Systems VII*, page 75. SPIE, 12 2020a. ISBN 9781510636835. doi: 10.1117/12.2562559.

T. Butterley, R. W. Wilson, M. Sarazin, C. M. Dubbeldam, J. Osborn, and P. Clark. Characterization of the ground layer of turbulence at Paranal using a robotic SLODAR system. *Monthly Notices of the Royal Astronomical Society*, 492(1):934–949, 2 2020b. ISSN 0035-8711. doi: 10.1093/mnras/stz3498.

Celestron. CGX-L Equatorial Mount and Tripod Instruction Manual, 2021.

J. Chabé, E. Aristidi, A. Ziad, H. Lantéri, Y. Fanteï-Caujolle, C. Giordano, J. Borgnino, M. Marjani, and C. Renaud. PML: a generalized monitor of atmospheric turbulence profile with high vertical resolution. *Applied Optics*, 59(25):7574, 9 2020. ISSN 1559-128X. doi: 10.1364/AO.384504. URL `https://www.osapublishing.org/abstract.cfm?URI=ao-59-25-7574https://opg.optica.org/abstract.cfm?URI=ao-59-25-7574`.

V. W. S. Chan. Free-Space Optical Communications. *Journal of Lightwave Technology*, 24(12):4750–4762, 12 2006. ISSN 0733-8724. doi: 10.1109/JLT.2006.885252. URL `http://ieeexplore.ieee.org/document/4063386/`.

G. Chiozzi, H. Sommer, M. Sarazin, T. Bierwirth, D. Dorigo, I. Vera Sequeiros, J. Navarrete, and D. Del Valle. The ESO astronomical site monitor upgrade. In G. Chiozzi and J. C. Guzman, editors, *Software and Cyberinfrastructure for Astronomy IV*, page 991314. SPIE, 8 2016. doi: 10.1117/12.2232302. URL `http://proceedings.spiedigitallibrary.org/proceeding.aspx?doi=10.1117/12.2232302`.

J.-M. Conan, A. Montmerle-Bonnefois, N. Védrenne, C. B. Lim, C. Petit, V. Michau, M.-T. Velluet, J.-F. Sauvage, S. Meimon, and C. Robert. Adaptive Optics for GEO-Feeder Links, from Performance Analysis via Reciprocity Based Models to Experimental Demonstration. In *COAT-2019 - workshop (Communications and Observations through Atmospheric Turbulence: characterization and mitigation)*, Châtillon, 12 2019. ONERA.

A. Costille and T. Fusco. Impact of the Cn2 description on WFAO performance. In *AO for ELT 2011 - 2nd International Conference on Adaptive Optics for Extremely Large Telescopes*, 2011.

C. E. Coulman. Fundamental and Applied Aspects of Astronomical “Seeing”. *Annual Review of Astronomy and Astrophysics*, 23(1):19–57, 9 1985. ISSN 0066-4146. doi: 10.1146/annurev.aa.23.090185.000315. URL `https://www.annualreviews.org/doi/10.1146/annurev.aa.23.090185.000315`.

J. C. Dainty, R. J. Scaddan, and J. Ring. Measurements of the Atmospheric Transfer Function at Mauna Kea, Hawaii. *Monthly Notices of the Royal Astronomical Society*, 170(3):519–532, 3 1975. ISSN 0035-8711. doi: 10.1093/mnras/170.3.519.

W. Dali Ali, A. Ziad, A. Berdja, J. Maire, J. Borgnino, M. Sarazin, G. Lombardi, J. Navarrete, H. Vazquez Ramio, M. Reyes, J. M. Delgado, J. J. Fuensalida, A. Tokovinin, and E. Bustos. Multi-instrument measurement campaign at Paranal in 2007. *Astronomy & Astrophysics*, 524(3):A73, 12 2010. ISSN 0004-6361. doi: 10.1051/0004-6361/201015178. URL `http://www.aanda.org/10.1051/0004-6361/201015178`.

J. R. Ducati. Catalogue of Stellar Photometry in Johnson’s 11-color system. *VizieR Online Data Catalog*, 2237:0, 2002.

C. Erven, C. Couteau, R. Laflamme, and G. Weihs. Entangled quantum key distribution over two free-space optical links. *Optics Express*, 16(21):16840–16853, 10 2008. ISSN 1094-4087. doi: 10.1364/OE.16.016840. URL `https://opg.optica.org/oe/abstract.cfm?uri=oe-16-21-16840`.

O. J. D. Farley, M. J. Townson, and J. Osborn. FAST: Fourier domain adaptive optics simulation tool for bidirectional ground-space optical links through atmospheric turbulence. *Optics Express*, 30(13), 2022. ISSN 10944087. doi: 10.1364/oe.458659.

D. L. Fried. Statistics of a Geometric Representation of Wavefront Distortion. *Journal of the Optical Society of America*, 55(11):1427, 1965. ISSN 0030-3941. doi: 10.1364/josa.55.001427. URL `https://www.osapublishing.org/abstract.cfm?URI=josa-55-11-1427`.

S. Fromovitz. Methods for Solving Incorrectly Posed Problems (V. A. Morozov). *SIAM Review*, 28(1), 1986. ISSN 0036-1445. doi: 10.1137/1028021.

A. Fuchs, M. Tallon, and J. Vernin. Focusing on a Turbulent Layer: Principle of the "Generalized SCIDAR". *Publications of the Astronomical Society of the Pacific*, 110(743):86–91, 1 1998. ISSN 0004-6280. doi: 10.1086/316109. URL `http://iopscience.iop.org/article/10.1086/316109`.

C. Fuchs and F. Moll. Ground station network optimization for space-to-ground optical communication links. *Journal of Optical Communications and Networking*, 7(12), 2015. ISSN 19430620. doi: 10.1364/JOCN.7.001148.

T. Fusco, J.-M. Conan, V. Michau, L. M. Mugnier, and G. Rousset. Efficient phase estimation for large-field-of-view adaptive optics. *Optics Letters*, 24(21): 1472, 11 1999. ISSN 0146-9592. doi: 10.1364/OL.24.001472. URL `https://opg.optica.org/abstract.cfm?URI=ol-24-21-1472`.

J.-L. Gach, D. Boutolleau, C. Brun, T. Carmignani, F. Clop, P. Feautrier, S. Lemarchand, E. Stadler, and Y. Wanwanscappel. C-RED 3: A SWIR camera for FSO applications. In H. Hemmati and D. M. Boroson, editors, *Free-Space Laser Communications XXXII*, page 14. SPIE, 3 2020. ISBN 9781510633070. doi: 10.1117/12.2545823. URL `https://www.spiedigitallibrary.org/conference-proceedings-of-spie/11272/2545823/C-RED-3-A-SWIR-camera-for-FSO-applications/10.1117/12.2545823.full`.

E. Gendron and P. Lena. Astronomical adaptive optics. II. Experimental results of an optimized modal control. *Astronomy and Astrophysics Supplement Series*, 111:153–167, 1995.

M. Goodwin, C. Jenkins, and A. Lambert. Improved detection of atmospheric turbulence with SLODAR. *Optics Express*, 15(22):14844, 10 2007. ISSN 1094-4087. doi: 10.1364/OE.15.014844.

R. Griffiths, J. Osborn, O. Farley, T. Butterley, M. Townson, and R. Wilson. The 24hSHIMM: a continuous day and night turbulence monitor for optical communications. In H. Hemmati and B. S. Robinson, editors, *Free-Space Laser Communications XXXV*, page 54. SPIE, 3 2023a. ISBN 9781510659315. doi: 10.1117/12.2648789.

R. Griffiths, J. Osborn, O. Farley, T. Butterley, M. J. Townson, and R. Wilson. Demonstrating 24-hour continuous vertical monitoring of atmospheric optical turbulence. *Optics Express*, 31(4):6730, 2 2023b. ISSN 1094-4087. doi: 10.1364/OE.479544. URL `https://opg.optica.org/abstract.cfm?URI=oe-31-4-6730`.

R. Griffiths, L. Bardou, T. Butterley, J. Osborn, R. Wilson, E. Bustos, A. Tokovinin, M. Le Louarn, and A. Otarola. A comparison of next-generation turbulence profiling instruments at Paranal. *Monthly Notices of the Royal Astronomical Society*, 529(1):320–330, 2 2024. ISSN 0035-8711. doi: 10.1093/mnras/stae434.

A. Guesalaga, B. Neichel, A. Cortés, C. Béchet, and D. Guzmán. Using the `${C_{n}^{2}}$` and wind profiler method with wide-field laser-guide-stars adaptive optics to quantify the frozen-flow decay. *Monthly Notices of the Royal Astronomical Society*, 440(3):1925–1933, 5 2014. ISSN 0035-8711. doi: 10.1093/mnras/stu366.

A. Guesalaga, S. Perera, J. Osborn, M. Sarazin, B. Neichel, and R. Wilson. FASS: the full aperture seeing sensor. In E. Marchetti, L. M. Close, and J.-P. Véran, editors, *Adaptive Optics Systems V*, page 99090H. SPIE, 7 2016. doi: 10.1117/12.2232012. URL `http://proceedings.spiedigitallibrary.org/proceeding.aspx?doi=10.1117/12.2232012`.

A. Guesalaga, B. Neichel, C. M. Correia, T. Butterley, J. Osborn, E. Masciadri, T. Fusco, and J. F. Sauvage. Online estimation of the wavefront outer scale profile from adaptive optics telemetry. *Monthly Notices of the Royal Astronomical Society*, 465(2), 2017. ISSN 13652966. doi: 10.1093/mnras/stw2548.

A. Guesalaga, B. Ayancán, M. Sarazin, R. W. Wilson, S. Perera, and M. Le Louarn. FASS: a turbulence profiler based on a fast, low-noise camera. *Monthly Notices of the Royal Astronomical Society*, 501(2):3030–3045, 2 2021. ISSN 0035-8711. doi: 10.1093/mnras/staa3823.

P. C. Hansen. Analysis of Discrete Ill-Posed Problems by Means of the L-Curve. *SIAM Review*, 34(4):561–580, 12 1992. ISSN 0036-1445. doi: 10.1137/1034115. URL `http://epubs.siam.org/doi/10.1137/1034115`.

P. C. Hansen and D. P. O'Leary. The Use of the L-Curve in the Regularization of Discrete Ill-Posed Problems. *SIAM Journal on Scientific Computing*, 14(6): 1487–1503, 11 1993. ISSN 1064-8275. doi: 10.1137/0914086. URL `http://epubs.siam.org/doi/10.1137/0914086`.

R. E. Hufnagel and N. R. Stanley. Modulation Transfer Function Associated with Image Transmission through Turbulent Media. *Journal of the Optical Society of America*, 54(1):52, 1 1964. ISSN 0030-3941. doi: 10.1364/JOSA.54.000052.

C. R. Jenkins. Fast guiding and small telescopes in the 8-m era. *Monthly Notices of the Royal Astronomical Society*, 294(1):69–92, 2 1998. ISSN 0035-8711. doi: 10.1046/j.1365-8711.1998.01196.x. URL `https://academic.oup.com/mnras/article-lookup/doi/10.1046/j.1365-8711.1998.01196.x`.

F. Kasten and A. T. Young. Revised optical air mass tables and approximation formula. *Applied Optics*, 28(22):4735, 11 1989. ISSN 0003-6935. doi: 10.1364/AO.28.004735.

A. Kellerer and A. Tokovinin. Atmospheric coherence times in interferometry: definition and measurement. *Astronomy & Astrophysics*, 461(2):775–781, 1 2007. ISSN 0004-6361. doi: 10.1051/0004-6361:20065788.

F. X. Kneizys, E. Shettle, L. W. Abreu, J. H. Chetwynd, and G. P. Anderson. User guide to LOWTRAN 7, 1988.

B. Koehler and C. Flebus. VLTI auxiliary telescopes. In P. J. Lena and A. Quirrenbach, editors, *Interferometry in Optical Astronomy*, page 13. SPIE, 7 2000. doi: 10.1117/12.390206. URL `http://proceedings.spiedigitallibrary.org/proceeding.aspx?doi=10.1117/12.390206`.

A. N. Kolmogorov. The Local Structure of Turbulence in Incompressible Viscous Fluid for Very Large Reynolds, 1941. URL `https://cir.nii.ac.jp/crid/1371131421197965440`.

V. Kornilov. Stellar scintillation in the short exposure regime and atmospheric coherence time evaluation. *Astronomy & Astrophysics*, 530:A56, 6 2011a. ISSN 0004-6361. doi: 10.1051/0004-6361/201116553.

V. Kornilov and B. Safonov. Differential image motion in the short-exposure regime. *Monthly Notices of the Royal Astronomical Society*, 418(3), 2011. ISSN 00358711. doi: 10.1111/j.1365-2966.2011.19604.x.

V. Kornilov, A. A. Tokovinin, O. Vozyakova, A. Zaitsev, N. Shatsky, S. F. Potanin, and M. S. Sarazin. MASS: a monitor of the vertical turbulence distribution. In P. L. Wizinowich and D. Bonaccini, editors, *Adaptive Optical System Technologies II*, page 837, 2 2003. doi: 10.1117/12.457982. URL `http://proceedings.spiedigitallibrary.org/proceeding.aspx?doi=10.1117/12.457982`.

V. G. Kornilov. The statistics of the photometric accuracy based on MASS data and the evaluation of high-altitude wind. *Astronomy Letters*, 37(1):40–48, 1 2011b. ISSN 1063-7737. doi: 10.1134/S1063773710111027.

O. Lai, J. K. Withington, R. Laugier, and M. Chun. Direct measure of dome seeing with a localized optical turbulence sensor. *Mon. Not. R. Astron. Soc.*, 484(4):5568–5577, 2 2019. ISSN 0035-8711. doi: 10.1093/mnras/

stz396. URL `https://academic.oup.com/mnras/advance-article/doi/10.1093/mnras/stz396/5309992`.

R. G. Lane and M. Tallon. Wave-front reconstruction using a Shack–Hartmann sensor. *Applied Optics*, 31(32):6902, 11 1992. ISSN 0003-6935. doi: 10.1364/AO.31.006902.

C. L. Lawson and R. J. Hanson. *Solving Least Squares Problems.* Society for Industrial and Applied Mathematics, 1 1995. ISBN 978-0-89871-356-5. doi: 10.1137/1.9781611971217. URL `http://epubs.siam.org/doi/book/10.1137/1.9781611971217`.

M. G. Löfdahl. Evaluation of image-shift measurement algorithms for solar Shack-Hartmann wavefront sensors. *Astronomy & Astrophysics*, 524, 2010. ISSN 0004-6361. doi: 10.1051/0004-6361/201015331.

P. Lognoné, J.-M. Conan, G. Rekaya, and N. Védrenne. Phase estimation at the point-ahead angle for AO pre-compensated ground to GEO satellite telecoms. *Optics Express*, 31(3), 2023. ISSN 10944087. doi: 10.1364/oe.476328.

G. Lombardi and M. Sarazin. Using MASS for AO simulations: A note on the comparison between MASS and Generalized SCIDAR techniques. *Monthly Notices of the Royal Astronomical Society*, 455(3), 2016. ISSN 13652966. doi: 10.1093/mnras/stv2441.

G. Lombardi, V. Zitelli, and S. Ortolani. The astroclimatological comparison of the Paranal Observatory and El Roque de Los Muchachos Observatory. *Monthly Notices of the Royal Astronomical Society*, 399(2):783–793, 10 2009. ISSN 00358711. doi: 10.1111/j.1365-2966.2009.15309.x. URL `https://academic.oup.com/mnras/article-lookup/doi/10.1111/j.1365-2966.2009.15309.x`.

G. Lombardi, J. Melnick, R. H. Hinojosa Goñi, J. Navarrete, M. Sarazin, A. Berdja, A. Tokovinin, R. Wilson, J. Osborn, T. Butterley, and H. Shepherd. Surface layer characterization at Paranal Observatory. In L. M. Stepp, R. Gilmozzi, and H. J. Hall, editors, *Ground-based and Airborne Telescopes III*, page 77334D. SPIE, 7 2010. doi: 10.1117/12.856772. URL `http://proceedings.spiedigitallibrary.org/proceeding.aspx?doi=10.1117/12.856772`.

J. Maire, A. Ziad, J. Borgnino, and F. Martin. Measurements of profiles of the wavefront outer scale using observations of the limb of the Moon. *Monthly Notices of the Royal Astronomical Society*, 377(3), 2007. ISSN 13652966. doi: 10.1111/j.1365-2966.2007.11681.x.

F. Martin, R. Conan, A. Tokovinin, A. Ziad, H. Trinquet, J. Borgnino, A. Agabi, and M. Sarazin. Optical parameters relevant for High Angular Resolution at Paranal from GSM instrument and surface layer contribution. *Astronomy and Astrophysics Supplement Series*, 144(1), 2000. ISSN 03650138. doi: 10.1051/aas:2000197.

E. Masciadri, G. Lombardi, and F. Lascaux. On the comparison between MASS and generalized-SCIDAR techniques. *Monthly Notices of the Royal Astronomical Society*, 438(2):983–1004, 2 2014. ISSN 0035-8711. doi: 10.1093/mnras/stt2194. URL `http://academic.oup.com/mnras/article/438/2/983/1002909/On-the-comparison-between-MASS-and`.

E. Masciadri, G. Martelloni, and A. Turchi. Filtering techniques to enhance optical turbulence forecast performances at short time-scales. *Monthly Notices of the Royal Astronomical Society*, 492(1):140–152, 2 2020. ISSN 0035-8711. doi: 10.1093/mnras/stz3342. URL `https://academic.oup.com/mnras/article/492/1/140/5647365`.

E. Masciadri, A. Turchi, and L. Fini. Optical turbulence forecasts at short time-scales using an autoregressive method at the Very Large Telescope. *Monthly Notices of the Royal Astronomical Society*, 523(3):3487–3502, 6 2023. ISSN 0035-8711. doi: 10.1093/mnras/stad1552. URL `https://academic.oup.com/mnras/article/523/3/3487/7193819`.

R. Mata Calvo, J. Poliak, J. Surof, A. Reeves, M. Richerzhagen, H. F. Kelemu, R. Barrios, C. Carrizo, R. Wolf, F. Rein, A. Dochhan, K. Saucke, and W. Luetke. Optical technologies for very high throughput satellite communications. In H. Hemmati and D. M. Boroson, editors, *Free. Laser Commun. XXXI*, volume 10910, page 31. SPIE, 3 2019. ISBN 9781510624627. doi: 10.1117/12.2513819. URL `https://www.spiedigitallibrary.org/conference-proceedings-of-spie/10910/2513819/Optical-technologies-for-very-high-throughput-satellite-communications/10.1117/12.2513819.full`.

J. Milli, R. Gonzalez, P. R. Fluxa, A. Chacon, J. Navarette, M. Sarazin, E. Peña, R. Carrasco-Davis, A. Solarz, J. Smoker, C. Martayan, C. Melo, E. Sedaghati, S. Mieske, O. Hainaut, and L. Tacconi-Garman. Nowcasting the turbulence at the Paranal Observatory. In *AO4ELT 2019 - Proceedings 6th Adaptive Optics for Extremely Large Telescopes*, 2019.

R. J. Noll. Zernike Polynomials and Atmospheric Turbulence. *J Opt Soc Am*, 66(3):207–211, 3 1976. ISSN 0030-3941. doi: 10.1364/JOSA.66.000207. URL `https://www.osapublishing.org/abstract.cfm?URI=josa-66-3-207https://opg.optica.org/abstract.cfm?URI=josa-66-3-207`.

A. M. Obukhov. Turbulence in an atmosphere with a non-uniform temperature. *Boundary-Layer Meteorology*, 2(1):7–29, 1971. ISSN 0006-8314. doi: 10.1007/BF00718085.

H. Ogane, M. Akiyama, S. Oya, and Y. Ono. Atmospheric turbulence profiling with multi-aperture scintillation of a Shack–Hartmann sensor. *Monthly Notices of the Royal Astronomical Society*, 503(4):5778–5788, 4 2021. ISSN 0035-8711. doi: 10.1093/mnras/stab105. URL `https://academic.oup.com/mnras/article/503/4/5778/6225821`.

J. Osborn and D. Alaluf. Line-of-sight optical Dome Turbulence Monitor. *Monthly*

Notices of the Royal Astronomical Society, 525(2), 2023. ISSN 13652966. doi: 10.1093/mnras/stad2428.

J. Osborn, R. Wilson, T. Butterley, H. Shepherd, and M. Sarazin. Profiling the surface layer of optical turbulence with SLODAR. *Monthly Notices of the Royal Astronomical Society*, pages no–no, 5 2010. ISSN 00358711. doi: 10.1111/j.1365-2966.2010.16795.x. URL `https://academic.oup.com/mnras/article-lookup/doi/10.1111/j.1365-2966.2010.16795.x`.

J. Osborn, D. Föhring, V. S. Dhillon, and R. W. Wilson. Atmospheric scintillation in astronomical photometry. *Monthly Notices of the Royal Astronomical Society*, 452(2):1707–1716, 9 2015. ISSN 0035-8711. doi: 10.1093/mnras/stv1400. URL `https://academic.oup.com/mnras/article-lookup/doi/10.1093/mnras/stv1400`.

J. Osborn, R. W. Wilson, M. Sarazin, T. Butterley, A. Chacón, F. Derie, O. J. D. Farley, X. Haubois, D. Laidlaw, M. LeLouarn, E. Masciadri, J. Milli, J. Navarrete, and M. J. Townson. Optical turbulence profiling with Stereo-SCIDAR for VLT and ELT. *Monthly Notices of the Royal Astronomical Society*, 478(1): 825–834, 6 2018. ISSN 13652966. doi: 10.1093/mnras/sty1070. URL `http://arxiv.org/abs/1806.02585http://dx.doi.org/10.1093/mnras/sty1070`.

J. Osborn, M. J. Townson, O. J. D. Farley, A. Reeves, and R. M. Calvo. Adaptive Optics pre-compensated laser uplink to LEO and GEO. *Optics Express*, 29 (4):6113, 2021. ISSN 10944087. doi: 10.1364/oe.413013. URL `https://www.osapublishing.org/abstract.cfm?URI=oe-29-4-6113`.

J. Osborn, J.-E. Communal, and F. Jabet. Global atmospheric turbulence forecasting for free-space optical communications. In H. Hemmati and B. S. Robinson, editors, *Free-Space Laser Communications XXXV*, page 51. SPIE, 3 2023. ISBN 9781510659315. doi: 10.1117/12.2649795.

A. Otarola. Paranal Observatory site: Long-term statistics of optical turbulence, PWV and meteorological conditions. Technical report, ESO, 8 2021.

S. Perera. *SHIMM: A Low-Cost Portable Seeing Monitor for Astronomical Observing Sites*. PhD thesis, Durham University, 2017.

S. Perera, R. W. Wilson, T. Butterley, J. Osborn, O. J. Farley, and D. J. Laidlaw. SHIMM: a versatile seeing monitor for astronomy. *Monthly Notices of the Royal Astronomical Society*, 520(4), 2023. ISSN 13652966. doi: 10.1093/mnras/stad339.

B. C. Platt and R. Shack. History and Principles of Shack-Hartmann Wavefront Sensing. *Journal of Refractive Surgery*, 17(5), 9 2001. ISSN 1081-597X. doi: 10.3928/1081-597X-20010901-13.

M. Polnik, L. Mazzarella, M. Di Carlo, D. K. Oi, A. Riccardi, and A. Arulselvan. Scheduling of space to ground quantum key distribution. *EPJ Quantum Technology*, 7(1):3, 12 2020. ISSN 2662-4400. doi: 10.1140/epjqt/s40507-020-0079-6. URL `https://epjquantumtechnology.springeropen.com/articles/10.1140/epjqt/s40507-020-0079-6`.

W. H. Press, S. A. Teukolsky, W. T. Vettering, and B. P. Flannery. *NUMERICAL RECIPES The Art of Scientific Computing Third Edition*. Cambridge University Press, 2007.

F. Quatresooz, R. Griffiths, L. Bardou, R. Wilson, J. Osborn, D. Vanhoenacker-Janvier, and C. Oestges. Continuous daytime and nighttime forecast of atmospheric optical turbulence from numerical weather prediction models. *Optics Express*, 31(21):33850, 10 2023. ISSN 1094-4087. doi: 10.1364/OE.500090. URL `https://opg.optica.org/abstract.cfm?URI=oe-31-21-33850`.

R. Ragazzoni. Pupil plane wavefront sensing with an oscillating prism. *Journal of Modern Optics*, 43(2):289–293, 2 1996. ISSN 0950-0340. doi: 10.1080/09500349608232742.

C. Robert, J.-M. Conan, V. Michau, T. Fusco, and N. Vedrenne. Scintillation and phase anisoplanatism in Shack-Hartmann wavefront sensing. *Journal of the Optical Society of America A*, 23(3):613, 3 2006. ISSN 1084-7529. doi: 10.1364/JOSAA.23.000613. URL `https://opg.optica.org/abstract.cfm?URI=josaa-23-3-613`.

F. Roddier. The effects of atmospheric turbulence in optical astronomy. *Progress in Optics*, 19(C):281–376, 1981. ISSN 00796638. doi: 10.1016/S0079-6638(08)70204-X.

F. Roddier. *Adaptive Optics in Astronomy.* Cambridge University Press, 6 1999. ISBN 9780521553759. doi: 10.1017/CBO9780511525179. URL `https://www.cambridge.org/core/product/identifier/9780511525179/type/book`.

F. Roddier, C. Roddier, and N. Roddier. Curvature Sensing: A New Wavefront Sensing Method. In G. M. Morris, editor, *Statistical Optics*, page 203. SPIE, 12 1988. doi: 10.1117/12.948547. URL `http://proceedings.spiedigitallibrary.org/proceeding.aspx?doi=10.1117/12.948547`.

R. Sagar, C. S. Stalin, A. K. Pandey, W. Uddin, V. Mohan, B. B. Sanwal, S. K. Gupta, R. K. Yadav, A. K. Durgapal, S. Joshi, B. Kumar, A. C. Gupta, Y. C. Joshi, J. B. Srivastava, U. S. Chaubey, M. Singh, P. Pant, and K. G. Gupta. Evaluation of Devasthal site for optical astronomical observations. *Astronomy and Astrophysics Supplement Series*, 144(2):349–362, 6 2000. ISSN 0365-0138. doi: 10.1051/aas:2000213.

M. Sarazin. ESO VLT site evaluation. II. In *Workshop on ESO's Very Large Telescope*, pages 229–238, Venice, 9 1986. European Southern Observatory.

M. Sarazin and F. Roddier. The ESO differential image motion monitor. *Astronomy and Astrophysics*, 227(1):294–300, 1990.

M. Sarazin, J. P. Swings, I. Appenzeller, A. Ardeberg, P. Charvin, G. Lelièvre, C. Perrier, H. E. Schuster, and P. Shaver. VLT Report 62. Technical report, ESO, 11 1990.

M. Sarazin, J. Melnick, J. Navarrete, and G. Lombardi. Seeing is Believing: New Facts about the Evolution of Seeing on Paranal. *The Messenger*, 12 2008.

R. J. Sasiela. Wave-front correction by one or more synthetic beacons. *Journal of the Optical Society of America A*, 11(1):379, 1 1994. ISSN 1084-7529. doi: 10.1364/JOSAA.11.000379. URL `https://opg.optica.org/abstract.cfm?URI=josaa-11-1-379`.

C. M. Schieler, K. M. Riesing, B. C. Bilyeu, J. S. Chang, A. S. Garg, N. C. Gilbert, A. J. Horvath, R. S. Reeve, B. S. Robinson, J. P. Wang, S. Piazzolla, W. T. Roberts, J. M. Kovalik, and B. Keer. On-orbit demonstration of 200-Gbps laser communication downlink from the TBIRD CubeSat. In H. Hemmati and B. S. Robinson, editors, *Free-Space Laser Communications XXXV*, page 1. SPIE, 3 2023. ISBN 9781510659315. doi: 10.1117/12.2651297.

H. W. Shepherd, J. Osborn, R. W. Wilson, T. Butterley, R. Avila, V. S. Dhillon, and T. J. Morris. Stereo-SCIDAR: Optical turbulence profiling with high sensitivity using a modified SCIDAR instrument. *Monthly Notices of the Royal Astronomical Society*, 437(4):3568–3577, 2 2014. ISSN 13652966. doi: 10.1093/mnras/stt2150. URL `http://academic.oup.com/mnras/article/437/4/3568/1007168/StereoSCIDAR-optical-turbulence-profiling-with`.

P. Stark and R. Parker. Bounded-Variable Least-Squares: an Algorithm and Applications. *Computational Statistics*, 10, 6 1995.

N. Takato, M. Iye, and I. Yamaguchi. Wavefront reconstruction error of Shack-Hartmann wavefront sensors. *Publications of the Astronomical Society of the Pacific*, 106, 1994. ISSN 0004-6280. doi: 10.1086/133367.

V. Tatarski. *Wave Propagation in a Turbulent Medium.* Jerusalem: Israel Program for Scientific Translations, 1971.

V. I. Tatarski, R. A. Silverman, and N. Chako. <i>Wave Propagation in a Turbulent Medium</i>. *Physics Today*, 14(12):46–51, 12 1961. ISSN 0031-9228. doi: 10.1063/1.3057286.

G. I. Taylor. The Spectrum of Turbulence. *Proceedings of the Royal Society of London. Series A - Mathematical and Physical Sciences*, 164(919):476–490, 2 1938. ISSN 0080-4630. doi: 10.1098/rspa.1938.0032.

S. Thomas, T. Fusco, A. Tokovinin, M. Nicolle, V. Michau, and G. Rousset. Comparison of centroid computation algorithms in a Shack-Hartmann sensor. *Monthly Notices of the Royal Astronomical Society*, 371(1):323–336, 8 2006. ISSN 00358711. doi: 10.1111/j.1365-2966.2006.10661.x. URL `https://academic.oup.com/mnras/article-lookup/doi/10.1111/j.1365-2966.2006.10661.x`.

A. N. Tikhonov, A. V. Goncharsky, V. V. Stepanov, and A. G. Yagola. *Numerical Methods for the Solution of Ill-Posed Problems.* Springer Netherlands, Dordrecht, 1995. ISBN 978-90-481-4583-6. doi: 10.1007/978-94-015-8480-7. URL `http://link.springer.com/10.1007/978-94-015-8480-7`.

A. Tokovinin. Measurement of seeing and the atmospheric time constant by differential scintillations. *Applied Optics*, 41(6):957, 2002a. ISSN 0003-6935. doi: 10.1364/ao.41.000957. URL `https://opg.optica.org/abstract.cfm?URI=ao-41-6-957`.

A. Tokovinin. From Differential Image Motion to Seeing. *Publications of the Astronomical Society of the Pacific*, 114(800), 2002b. ISSN 0004-6280. doi: 10.1086/342683.

A. Tokovinin. Requirements for AO-ELT operation and ELT site monitor. In *1st AO4ELT conference - Adaptive Optics for Extremely Large Telescopes*, page 02005, Les Ulis, France, 2 2010. EDP Sciences. ISBN 978-2-7598-0496-2. doi:

10.1051/ao4elt/201002005. URL `http://ao4elt.edpsciences.org/10.1051/ao4elt/201002005`.

A. Tokovinin. Measurement of turbulence profile from defocused ring images. *Monthly Notices of the Royal Astronomical Society*, 502(1):794–808, 1 2021. ISSN 0035-8711. doi: 10.1093/mnras/staa4049.

A. Tokovinin. The Elusive Nature of “Seeing”. *Atmosphere*, 14(11):1694, 11 2023. ISSN 2073-4433. doi: 10.3390/atmos14111694.

A. Tokovinin, V. Kornilov, N. Shatsky, and O. Voziakova. Restoration of turbulence profile from scintillation indices. *Monthly Notices of the Royal Astronomical Society*, 343(3):891–899, 8 2003. ISSN 0035-8711. doi: 10.1046/j.1365-8711.2003.06731.x. URL `https://academic.oup.com/mnras/article/343/3/891/1123465`.

A. Tokovinin, A. Kellerer, and V. Coudé Du Foresto. FADE, an instrument to measure the atmospheric coherence time. *Astronomy & Astrophysics*, 477(2):671–680, 1 2008. ISSN 0004-6361. doi: 10.1051/0004-6361:20077996.

A. A. Tokovinin. Polychromatic scintillation. *Journal of the Optical Society of America A*, 20(4):686, 4 2003. ISSN 1084-7529. doi: 10.1364/JOSAA.20.000686.

M. J. Townson, O. J. D. Farley, G. Orban de Xivry, J. Osborn, and A. P. Reeves. AOtools: a Python package for adaptive optics modelling and analysis. *Optics Express*, 27(22):31316, 2019. ISSN 10944087. doi: 10.1364/oe.27.031316. URL `https://www.osapublishing.org/abstract.cfm?URI=oe-27-22-31316`.

M. J. Townson, C. Bond, C. Correia, S. Dimoudi, T. Morris, E. Younger, D. T. Barr, and S. Cetre. RTC Design and Performance Modelling for ELT Scale AO. In L. Schreiber, D. Schmidt, and E. Vernet, editors, *Adaptive Optics Systems VIII*, volume 12185, page 121851E, Bellingham, 8 2022. SPIE. doi: 10.1117/12.2631360. URL `https://doi.org/10.1117/12.2631360`.

N. Védrenne, V. Michau, C. Robert, and J.-M. Conan. C_n^2 profile measurement from Shack-Hartmann data. *Optics Letters*, 32(18):2659, 9 2007. ISSN 0146-9592. doi: 10.1364/OL.32.002659. URL `https://opg.optica.org/abstract.cfm?URI=ol-32-18-2659`.

N. Védrenne, A. Bonnefois Montmerle, C. Robert, V. Michau, J. Montri, and B. Fleury. Cn2 profile measurement from Shack-Hartmann data: experimental validation and exploitation. In K. Stein and J. D. Gonglewski, editors, *Optics in Atmospheric Propagation and Adaptive Systems XIII*, volume 7828, page 78280B. SPIE, 10 2010. doi: 10.1117/12.866168. URL `http://proceedings.spiedigitallibrary.org/proceeding.aspx?doi=10.1117/12.866168`.

J. Voyez, C. Robert, J.-M. Conan, L. M. Mugnier, E. Samain, and A. Ziad. First on-sky results of the CO-SLIDAR C^2_n profiler. *Optics Express*, 22(9):10948, 2014. ISSN 10944087. doi: 10.1364/oe.22.010948.

R. W. Wilson. SLODAR: measuring optical turbulence altitude with a Shack-Hartmann wavefront sensor. *Monthly Notices of the Royal Astronomical Society*, 337(1):103–108, 11 2002. ISSN 00358711. doi: 10.1046/j.1365-8711.2002.05847.x. URL `https://academic.oup.com/mnras/article-lookup/doi/10.1046/j.1365-8711.2002.05847.x`.

R. W. Wilson and C. R. Jenkins. Adaptive optics for astronomy: theoretical performance and limitations. *Monthly Notices of the Royal Astronomical Society*, 278(1):39–61, 1 1996. ISSN 0035-8711. doi: 10.1093/mnras/278.1.39.

P. R. Wood, A. W. Rodgers, and K. S. Russell. Seeing Measurements at Freeling Heights and Siding Spring Observatory. *Publications of the Astronomical Society of Australia*, 12(1):97–105, 4 1995. ISSN 1323-3580. doi: 10.1017/S1323358000020129.

N. Woolf. Dome seeing. *Publications of the Astronomical Society of the Pacific*, 91:

523, 8 1979. ISSN 0004-6280. doi: 10.1086/130532. URL `http://iopscience.iop.org/article/10.1086/130532`.

Y. Xiang, D. Sun, W. Fan, and X. Gong. Generalized simulated annealing algorithm and its application to the Thomson model. *Physics Letters A*, 233(3):216–220, 8 1997. ISSN 03759601. doi: 10.1016/S0375-9601(97)00474-X.

A. T. Young. Aperture Filtering and Saturation of Scintillation. *Journal of the Optical Society of America*, 60(2):248, 2 1970. ISSN 0030-3941. doi: 10.1364/JOSA.60.000248. URL `https://opg.optica.org/abstract.cfm?URI=josa-60-2-248`.

A. Ziad. Review of the outer scale of the atmospheric turbulence. In E. Marchetti, L. M. Close, and J.-P. Véran, editors, *Adaptive Optics Systems V*, page 99091K. SPIE, 7 2016. doi: 10.1117/12.2231375. URL `http://proceedings.spiedigitallibrary.org/proceeding.aspx?doi=10.1117/12.2231375`.

A. Ziad, R. Gredel, J. Aceituno, J. Borgnino, F. Hoyo, A. Irbah, F. Martin, U. Thiele, and S. Pedraz. A site-testing campaign at the Calar Alto Observatory with GSM and DIMM instruments. *Monthly Notices of the Royal Astronomical Society*, 362(2):455–459, 9 2005. ISSN 00358711. doi: 10.1111/j.1365-2966.2005.09299.x.

Colophon

This thesis is based on a template developed by Matthew Townson and Andrew Reeves. It was typeset with LaTeX 2_ε. It was created using the *memoir* package, maintained by Lars Madsen, with the *madsen* chapter style. The font used is Latin Modern, derived from fonts designed by Donald E. Kunith.